

1 SEARCH FOR PRODUCTION OF A HIGGS BOSON AND A SINGLE TOP
2 QUARK IN MULTILEPTON FINAL STATES IN pp COLLISIONS AT $\sqrt{s} = 13$
3 TeV.

4 by

5 Jose Andres Monroy Montañez

A DISSERTATION

7 Presented to the Faculty of

8 The Graduate College at the University of Nebraska

9 In Partial Fulfilment of Requirements

10 For the Degree of Doctor of Philosophy

11 Major: Physics and Astronomy

12 Under the Supervision of Kenneth Bloom and Aaron Dominguez

13 Lincoln, Nebraska

14 July, 2018

15 SEARCH FOR PRODUCTION OF A HIGGS BOSON AND A SINGLE TOP
16 QUARK IN MULTILEPTON FINAL STATES IN pp COLLISIONS AT $\sqrt{s} = 13$
17 TeV.

18 Jose Andres Monroy Montañez, Ph.D.

19 University of Nebraska, 2018

20 Adviser: Kenneth Bloom and Aaron Dominguez

²¹ Table of Contents

²²	Table of Contents	iii
²³	List of Figures	vii
²⁴	List of Tables	ix
²⁵	1 INTRODUCTION	1
²⁶	2 Theoretical approach	2
²⁷	2.1 Introduction	2
²⁸	2.2 Standard model of particle physics	3
²⁹	2.2.1 Fermions	5
³⁰	2.2.1.1 Leptons	6
³¹	2.2.1.2 Quarks	9
³²	2.2.2 Fundamental interactions	13
³³	2.2.3 Gauge Bosons	18
³⁴	2.3 Electroweak unification and the Higgs mechanism	20
³⁵	2.3.1 Spontaneous symmetry breaking (SSB)	28
³⁶	2.3.2 Higgs mechanism	32
³⁷	2.3.3 Masses of the gauge bosons	34

38	2.3.4	Masses of the fermions	35
39	2.3.5	The Higgs field	36
40	2.3.6	Higgs boson production mechanisms at LHC.	37
41	2.3.7	Higgs decay channels	41
42	2.4	Associated Production of Higgs Boson and Single Top Quark.	42
43	2.5	The CP-mixing in tH processes	47
44	3	The CMS experiment at the LHC	52
45	3.1	Introduction	52
46	3.2	The LHC	53
47	3.3	The CMS experiment	61
48	3.3.1	coordinate system	63
49	3.3.2	tracker- pixels and strips	63
50	3.3.3	calorimeters	63
51	3.3.4	magnet	63
52	3.3.5	muon system	63
53	3.3.6	trigger system - HLT- L1	63
54	3.3.7	computing model	63
55	3.4	Event generation simulation and reconstruction	63
56	3.4.1	event generation	63
57	3.4.2	Hard scattering	63
58	3.4.3	parton shower	63
59	3.4.4	hadronization and decays	63
60	3.4.5	underlying events and pileup	63
61	3.4.6	MC - MadEvent, MadGraph and madgraphNLO, powheg, pythia, tauola	63

63	3.4.7	detector simulation	63
64	3.4.8	event reconstruction- particle flow algorithm, vertexing , muon	
65		reco, electron reco, photon and hadron reco, jets reco, anti-kt	
66		algoritm, jet energy corrections, btagging, MET	63
67	3.4.9	MVA methods, NN, BDT, boosting, overtraining, variable	
68		ranking	63
69	3.4.10	statistical inference, likelihood parametrization	63
70	3.4.11	nuisance paraeters	63
71	3.4.12	exclusion limits	63
72	3.4.13	asymptotic limits	63
73	4	Search for production of a Higgs boson and a single top quark in	
74	multilepton final states in pp collisions at $\sqrt{s} = 13$ TeV		64
75	4.1	Introduction	64
76	4.2	Data and MC Samples	66
77	4.2.1	Full 2016 dataset and MC samples	66
78	4.2.2	Triggers	69
79	4.2.2.1	Trigger efficiency scale factors	69
80	4.3	Object Identification and event selection	70
81	4.3.1	Jets and b tagging	70
82	4.3.2	Lepton selection	71
83	4.3.3	Lepton selection efficiency	72
84	4.4	Background predictions	73
85	4.5	Signal discrimination	74
86	4.5.1	Classifiers response	78
87	4.6	Additional discriminating variables	81

88	5 The CMS forward pixel detector	84
89	5.0.1 The phase 1 FPix upgrade	84
90	5.0.2 FPix module production line	84
91	5.0.3 The Gluing stage	84
92	5.0.4 The Encapsulation stage	84
93	5.0.5 The FPix module production yields	84
94	Bibliography	84
95	References	85

⁹⁶ List of Figures

97	1.1	^{14}N neutron capture in a PECVD polymerized pyridine film. The Q-value of this reaction is 626 keV. Taken from [22]	1
99	2.1	Standard model of particle physics.	4
100	2.2	WI transformations between quarks	12
101	2.3	Fundamental interactions in nature.	13
102	2.4	SM interactions diagrams	14
103	2.5	Neutral current processes	21
104	2.6	Spontaneous symmetry breaking mechanism	28
105	2.7	SSB Potential form	30
106	2.8	Potential for complex scalar field	30
107	2.9	SSB mechanism for complex scalar field	31
108	2.10	Proton-Proton collision	38
109	2.11	Higgs production mechanism Feynman diagrams	39
110	2.12	Higgs production cross section and decay branching ratios	40
111	2.13	Associated Higgs production mechanism Feynman diagrams	43
112	2.14	Cross section for tHq process as a function of κ_t	45
113	2.15	Cross section for tHW process as a function of κ_{Htt}	46
114	2.16	NLO cross section for tX_0 and $t\bar{t}X_0$	49

115	2.17 NLO cross section for tWX_0 , $t\bar{t}X_0$ and $tWX_0 + t\bar{t}X_0 + \text{interference}$	50
116	3.1 CERN accelerator complex	53
117	3.2 LHC protons source and first acceleration stage.	54
118	3.3 The LINAC2 accelerating system at CERN.	55
119	3.4 LHC layout and RF cavities module.	56
120	3.5 LHC dipole magnet.	58
121	3.6 2016 CMS Integrated luminosity	60
122	3.7 ref: CMS Collaboration, “Detector Drawings”, CMS-PHO-GEN-2012-002, http://cds.cern.ch/record/1433717 , 2012.	62
124	4.1 The two leading-order diagrams of tHq production.	65
125	4.2 Input variables to the BDT for signal discrimination normalized.	75
126	4.3 Input variables to the BDT for signal discrimination not normalized.	77
127	4.4 BDT inputs as seen by TMVA against $t\bar{t}$	78
128	4.5 BDT inputs as seen by TMVA against $t\bar{t}V$	79
129	4.6 Correlation matrices for the input variables in the TMVA.	80
130	4.7 MVA classifiers performance.	80
131	4.8 Additional discriminating variables distributions.	82

¹³² List of Tables

133	2.1	Fermions of the SM.	5
134	2.2	Fermion masses.	6
135	2.3	Leptons properties.	9
136	2.4	Quarks properties.	9
137	2.5	Fermion weak isospin and weak hypercharge multiplets.	11
138	2.6	Fundamental interactions features.	15
139	2.7	SM gauge bosons.	20
140	2.8	Higgs boson properties.	37
141	2.9	Predicted branching ratios for a SM Higgs boson with $m_H = 125 \text{ GeV}/c^2$	42
142	2.10	Predicted SM cross sections for tH production at $\sqrt{s} = 13 \text{ TeV}$	44
143	2.11	Predicted enhancement of the tHq and tHW cross sections at LHC	47
144	4.1	Signal samples and their cross section and branching fraction.	66
145	4.2	κ_V and κ_t combinations.	67
146	4.3	List of background samples used in this analysis (CMSSW 80X).	68
147	4.4	Leading-order $t\bar{t}W$ and $t\bar{t}Z$ samples used in the signal BDT training. . . .	68
148	4.5	Table of high-level triggers that we consider in the analysis.	69
149	4.6	Trigger efficiency scale factors and associated uncertainties.	70
150	4.7	Requirements on each of the three muon selections.	71

151	4.8	Criteria for each of the three electron selections.	72
152	4.9	MVA input discriminating variables	76
153	4.10	TMVA input variables ranking for BDTA_GRAD method	81
154	4.11	TMVA configuration used in the BDT training.	81
155	4.12	ROC-integral for all the testing cases.	83

¹⁵⁶ Chapter 1

¹⁵⁷ INTRODUCTION

Figure 1.1: ^{14}N neutron capture in a PECVD polymerized pyridine film. The Q-value of this reaction is 626 keV. Taken from [22]

¹⁵⁸ **Chapter 2**

¹⁵⁹ **Theoretical approach**

¹⁶⁰ **2.1 Introduction**

¹⁶¹ The physical description of the universe is a challenge that physicists have faced by
¹⁶² making theories that refine existing principles and proposing new ones in an attempt
¹⁶³ to embrace emerging facts and phenomena.

¹⁶⁴

¹⁶⁵ At the end of 1940s Julian Schwinger [11] and Richard P. Feynman [12], based in
¹⁶⁶ the work of Sin-Itiro Tomonaga [13], developed an electromagnetic theory consistent
¹⁶⁷ with special relativity and quantum mechanics that describes how matter and light
¹⁶⁸ interact; the so-called “quantum eletrodynamics” (QED) had born.

¹⁶⁹

¹⁷⁰ QED has become the guide in the development of theories that describe the universe.
¹⁷¹ It was the first example of a quantum field theory (QFT), which is the theoretical
¹⁷² framework for building quantum mechanical models that describes particles and their
¹⁷³ interactions. QFT is composed of a set of mathematical tools that combines classical
¹⁷⁴ fields, special relativity and quantum mechanics, while keeping the quantum point

175 particles and locality ideas.

176 This chapter gives an overview of the standard model of particle physics, starting
 177 with a description of the particles and interactions that compose it, followed by a
 178 description of the electroweak interaction, the Higgs boson and the associated pro-
 179 duction of Higgs boson and a single top quark (tH). The description contained in
 180 this chapter is based on references [1–3].

181 2.2 Standard model of particle physics

182 Particle physics at the fundamental level is modeled in terms of a collection of in-
 183 teracting particles and fields in a theory known as the “standard model of particle
 184 physics (SM)”¹.

185

186 The full picture of the SM is composed of three fields², whose excitations are inter-
 187 preted as particles called mediators or force-carriers; a set of fields, whose excitations
 188 are interpreted as elementary particles, interacting through the exchange of those
 189 mediators and a field that give the mass to elementary particles. Figure 2.1 shows an
 190 scheme of the SM particles organization. In addition to the particles in the scheme
 191 (but not listed in it), their corresponding anti-particles, with opposite quantum num-
 192 bers, are also part of the picture; some particles are their own anti-particles, like
 193 photon or Higgs, or anti-particle is already listed like in the W^+ and W^- case.

194

195 The mathematical formulation of the SM is based on group theory and the use of

¹ The formal and complete treatment of the SM is out of the scope of this document, however a plenty of textbooks describing it at several levels are available in the literature. The treatment in “An Introduction To Quantum Field Theory (Frontiers in Physics)” by Michael E. Peskin and Dan V. Schroeder is quite comprehensive and detailed.

² Note that gravitational field is not included in the standard model formulation

Standard Model of Elementary Particles

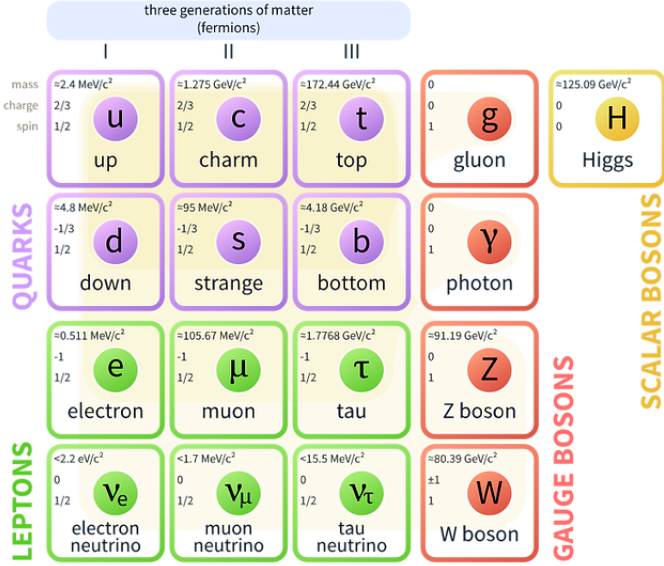


Figure 2.1: Schematic representation of the Standard model of particle physics. SM is a theoretical model intended to describe three of the four fundamental forces of the universe in terms of a set of particles and their interactions. [18].

196 Noether's theorem [17] which states that for a physical system modeled by a La-
 197 grangian that is invariant under a group of transformations a conservation law is
 198 expected. For instance, a system described by a time-independent Lagrangian is
 199 invariant (symmetric) under time changes (transformations) with the total energy
 200 conservation law as the expected conservation law. In QED, the charge operator
 201 (Q) is the generator of the $U(1)$ symmetry which according to the Noether's theorem
 202 means that there is a conserved quantity; this conserved quantity is the electric charge
 203 and thus the law conservation of electric charge is established.

204

205 In the SM, the symmetry group $SU(3)_C \otimes SU(2)_L \otimes U(1)_Y$ describes three of the
 206 four fundamental interactions in nature(see section 2.2.2): strong interaction(SI),
 207 weak interaction(WI) and electromagnetic interactions (EI) in terms of symmetries

208 associated to physical quantities:

209 • Strong: $SU(3)_C$ associated to color charge

210 • Weak: $SU(2)_L$ associated to weak isospin and chirality

211 • Electromagnetic: $U(1)_Y$ associated to weak hypercharge and electric charge

212 It will be shown that the electromagnetic and weak interactions are combined in
 213 the so-called electroweak interaction where chirality, hypercharge, weak isospin and
 214 electric charge are the central concepts.

215 2.2.1 Fermions

216 The basic constituents of the ordinary matter at the lowest level, which form the set
 217 of elementary particles in the SM formulation, are quarks and leptons. All of them
 218 have spin 1/2, therefore they are classified as fermions since they obey Fermi-Dirac
 219 statistics. There are six “flavors” of quarks and three of leptons organized in three
 220 generations, or families, as shown in table 2.1.

221

Generation				
	Type	1st	2nd	3rd
Leptons	Charged	Electron (e)	Moun(μ)	Tau (τ)
	Neutral	Electron neutrino (ν_e)	Muon neutrino (ν_μ)	Tau neutrino (ν_τ)
Quarks	Up-type	Up (u)	Charm (c)	Top (t)
	Down-type	Down (d)	Strange (s)	Bottom (b)

Table 2.1: Fermions of the SM. There are six flavors of quarks and three of leptons, organized in three generations, or families, composed of two pairs of closely related particles. The close relationship is motivated by the fact that WI between leptons is limited to the members of the same generation; WI between quarks is not limited but greatly favoured, to same generation members.

222

223 There is a mass hierarchy between generations (see table 2.2), where the higher gener-
 224 ation particles decays to the lower one, which can explain why the ordinary matter is
 225 made of particles in the first generation. In the SM, neutrinos are modeled as massless
 226 particles so they are not subject to this mass hierarchy; however, today it is known
 227 that neutrinos are massive so the hierarchy could be restated. The reason behind this
 228 mass hierarchy is one of the most important open questions in particle physics, and
 229 it becomes more puzzling when noticing that the mass difference between first and
 230 second generation fermions is small compared to the mass difference with respect to
 231 the third generation.

Lepton	Mass (MeV/c ²)	Quark	Mass (MeV/c ²)
e	0.51	u	2.2
μ	105.65	c	1.28×10^3
τ	1776.86	t	173.1×10^3
ν_e	Unknown	d	4.7
ν_μ	Unknown	s	96
τ_μ	Unknown	b	4.18×10^3

Table 2.2: Fermion masses [21]. Generations differ by mass in a way that have been interpreted as a masss hierarchy. Approximate values with no uncertainties are used, for comparison purpose.

232
 233 Usually, the second and third generation fermions are produced in high energy pro-
 234 cesses, like the ones recreated in particle accelerators.

235 2.2.1.1 Leptons

236 A lepton is an elementary particle that is not subject to the SI. As seen in table 2.1,
 237 there are two types of leptons, the charged ones (electron, muon and tau) and the
 238 neutral ones (the three neutrinos). The electric charge (Q) is the property that gives
 239 leptons the ability to participate in the EI. From the classical point of view, Q plays

240 a central role determining, among others, the strength of the electric field through
241 which the electromagnetic force is exerted. It is clear that neutrinos are not affected
242 by EI because they don't carry electric charge.

243

244 Another feature of the leptons that is fundamental in the mathematical description
245 of the SM is the chirality, which is closely related to spin and helicity. Helicity de-
246 fines the handedness of a particle by relating its spin and momentum such that if
247 they are parallel then the particle is right-handed; if spin and momentum are an-
248 tiparallel the particle is said to be left-handed. The study of parity conservation (or
249 violation) in β -decay have shown that only left-handed electrons/neutrinos or right-
250 handed positrons/anti-neutrinos are created [19]; the inclusion of that feature in the
251 theory was achieved by using projection operators for helicity, however, helicity is
252 frame dependent for massive particles which makes it not Lorentz invariant and then
253 another related attribute has to be used: *chirality*.

254

255 Chirality is a purely quantum attribute which makes it not so easy to describe in
256 graphical terms but it defines how the wave function of a particle transforms under
257 certain rotations. As with helicity, there are two chiral states, left-handed chiral (L)
258 and right-handed chiral (R). In the highly relativistic limit where $E \approx p \gg m$ helicity
259 and chirality converge, becoming exactly the same for massless particles.

260

261 In the following, when referring to left-handed (right-handed) it will means left-
262 handed chiral (right-handed chiral). The fundamental fact about chirality is that
263 while EI and SI are not sensitive to chirality, in WI left-handed and right-handed
264 fermions are treated asymmetrically, such that only left handed fermions and right-
265 handed anti-fermions are allowed to couple to WI mediators, which is a violation of

266 parity. The way to translate this statement in a formal mathematical formulation is
 267 based on the isospin symmetry group $SU(2)_L$.

268

269 Each generation of leptons is seen as a weak isospin doublet.³ The left-handed charged
 270 lepton and its associated left-handed neutrino are arranged in doublets of weak isospin
 271 $T=1/2$ while their right-handed partners are singlets:

$$\begin{pmatrix} \nu_l \\ l \end{pmatrix}_L, l_R := \begin{pmatrix} \nu_e \\ e \end{pmatrix}_L, \begin{pmatrix} \nu_\mu \\ \mu \end{pmatrix}_L, \begin{pmatrix} \nu_\tau \\ \tau \end{pmatrix}_L, e_R, \mu_R, \tau_R, \nu_{eR}, \nu_{\mu R}, \nu_{\tau R} \quad (2.1)$$

272 The isospin third component refers to the eigenvalues of the weak isospin operator
 273 which for doublets is $T_3 = \pm 1/2$, while for singlets it is $T_3 = 0$. The physical meaning
 274 of this doublet-singlet arrangement falls in that the WI couples the two particles in
 275 the doublet by exchanging the interaction mediator while the singlet member is not
 276 involved in WI. The main properties of the leptons are summarized in table 2.3.

277

278 Altough all three flavor neutrinos have been observed, their masses remain unknown
 279 and only some estimations have been made [20]. The main reason is that the fla-
 280 vor eigenstates are not the same as the mass eigenstates which implies that when
 281 a neutrino is created its mass state is a linear combination of the three mass eigen-
 282 states and experiments can only probe the squared difference of the masses. The
 283 Pontecorvo-Maki-Nakagawa-Sakata (PMNS) mixing matrix encode the relationship
 284 between flavor and mass eigenstates.

285

³ The weak isospin is an analogy of the isospin symmetry in strong interaction where neutron and proton are affected equally by strong force but differ in their charge.

Lepton	Q(e)	T_3	L_e	L_μ	L_τ	Lifetime (s)
Electron (e)	-1	-1/2	1	0	0	Stable
Electron neutrino(ν_e)	0	1/2	1	0	0	Unknown
Muon (μ)	-1	-1/2	0	1	0	2.19×10^{-6}
Muon neutrino (ν_μ)	0	1/2	0	1	0	Unknown
Tau (τ)	-1	-1/2	0	0	1	290.3×10^{-15}
Tau neutrino (τ_μ)	0	1/2	0	0	1	Unknown

Table 2.3: Leptons properties [21]. Q: electric charge, T_3 : weak isospin. Only left-handed leptons and right-handed anti-leptons participate in the WI. Anti-particles with inverted T_3 , Q and lepton number complete the leptons set but are not listed. Right-handed leptons and left-handed anti-leptons, neither listed, form weak isospin singlets with $T_3 = 0$ and do not take part in the weak interaction.

286 2.2.1.2 Quarks

287 Quarks are the basic constituents of protons and neutrons. The way quarks join to
288 form bound states, called “hadrons”, is through the SI. Quarks are affected by all the
289 fundamental interactions which means that they carry all the four types of charges:
290 color, electric charge, weak isospin and mass.

Flavor	Q(e)	I_3	T_3	B	C	S	T	B'	Y	Color
Up (u)	2/3	1/2	1/2	1/3	0	0	0	0	1/3	r,b,g
Charm (c)	2/3	0	1/2	1/3	1	0	0	0	4/3	r,b,g
Top(t)	2/3	0	1/2	1/3	0	0	1	0	4/3	r,b,g
Down(d)	-1/3	-1/2	-1/2	1/3	0	0	0	0	1/3	r,b,g
Strange(s)	-1/3	0	-1/2	1/3	0	-1	0	0	-2/3	r,b,g
Bottom(b)	-1/3	0	-1/2	1/3	0	0	0	-1	-2/3	r,b,g

Table 2.4: Quarks properties [21]. Q: electric charge, I_3 : isospin, T_3 : weak isospin, B: baryon number, C: charmness, S: strangeness, T: topness, B' : bottomness, Y: hypercharge. Anti-quarks posses the same mass and spin as quarks but all charges (color, flavor numbers) have opposite sign.

291

292 Table 2.4 summarizes the features of quarks, among which the most particular is
293 their fractional electric charge. Note that fractional charge is not a problem, given
294 that quarks are not found isolated, but serves to explain how composed particles are

295 formed out of two or more valence quarks⁴.

296

297 Color charge is the responsible for the SI between quarks and is the symmetry
 298 ($SU(3)_C$) that defines the formalism to describe SI. There are three colors: red (r),
 299 blue(b) and green(g) and their corresponding three anti-colors; thus each quark carries
 300 one color unit while anti-quarks carries one anti-color unit. As said above, quarks are
 301 not allowed to be isolated due to the color confinement effect, therefore their features
 302 have been studied indirectly by observing their bound states created when:

- 303 • one quark with a color charge is attracted by an anti-quark with the correspond-
 304 ing anti-color charge forming a colorless particle called a “meson.”
- 305 • three quarks (anti-quarks) with different color (anti-color) charges are attracted
 306 among them forming a colorless particle called a “baryon(anti-baryon).”

307 In the first version of the quark model (1964), M. Gell-Mann [22] and G. Zweig
 308 [23,24] developed a consistent way to classify hadrons according to their properties.
 309 Only three quarks (u, d, s) were involved in a scheme in which all baryons have
 310 baryon number B=1 and therefore quarks have B=1/3; non-baryons have B=0. The
 311 scheme organizes baryons in a two-dimensional space (I_3 - Y); Y (hypercharge) and I_3
 312 (isospin) are quantum numbers related by the Gell-Mann-Nishijima formula [25, 26]:

$$Q = I_3 + \frac{Y}{2} \quad (2.2)$$

313 where $Y = B + S + C + T + B'$ are the quantum numbers listed in table 2.4. Baryon
 314 number is conserved in SI and EI which means that single quarks cannot be created

⁴ Hadrons can contain an indefinite number of virtual quarks and gluons, known as the quark and gluon sea, but only the valence quarks determine hadrons' quantum numbers.

315 but in pairs $q - \bar{q}$.

316

317 There are six quark flavors organized in three generations (see table 2.1) following a
 318 mass hierarchy which, again, implies that higher generations decay to first generation
 319 quarks.

	Quarks			T_3	Y_W	Leptons			T_3	Y_W
Doublets	$(\begin{smallmatrix} u \\ d' \end{smallmatrix})_L$	$(\begin{smallmatrix} c \\ s' \end{smallmatrix})_L$	$(\begin{smallmatrix} t \\ b' \end{smallmatrix})_L$	$(\begin{smallmatrix} 1/2 \\ -1/2 \end{smallmatrix})$	1/3	$(\begin{smallmatrix} \nu_e \\ e \end{smallmatrix})_L$	$(\begin{smallmatrix} \nu_\mu \\ \mu \end{smallmatrix})_L$	$(\begin{smallmatrix} \nu_\tau \\ \tau \end{smallmatrix})_L$	$(\begin{smallmatrix} 1/2 \\ -1/2 \end{smallmatrix})$	-1
Singlets	u_R	c_R	t_R	0	4/3	ν_{eR}	$\nu_{\mu R}$	$\nu_{\tau R}$	0	-2

Table 2.5: Fermion weak isospin and weak hypercharge multiplets. Weak hypercharge is calculated through the Gell-Mann-Nishijima formula 2.2 but using the weak isospin and charge for quarks.

320

321 Isospin doublets of quarks are also defined (see table 2.5) and as for neutrinos, the
 322 mass eigenstates are not the same as the WI eigenstates which means that members of
 323 different quark generations are connected by the WI mediator; thus, up-type quarks
 324 are coupled not to down-type quarks directly but to a superposition of down-type
 325 quarks (q'_d) via WI according to:

$$q'_d = V_{CKM} q_d$$

326

$$\begin{pmatrix} d' \\ s' \\ b' \end{pmatrix} = \begin{pmatrix} V_{ud} & V_{us} & V_{ub} \\ V_{cd} & V_{cs} & V_{cb} \\ V_{td} & V_{ts} & V_{tb} \end{pmatrix} \begin{pmatrix} d \\ s \\ b \end{pmatrix} \quad (2.3)$$

327 where V_{CKM} is known as Cabibbo-Kobayashi-Maskawa (CKM) mixing matrix [27,28].
 328 The weak decays of quarks are represented in the diagram of figure 2.2; again the
 329 CKM matrix plays a central role since it contains the probabilities for the different

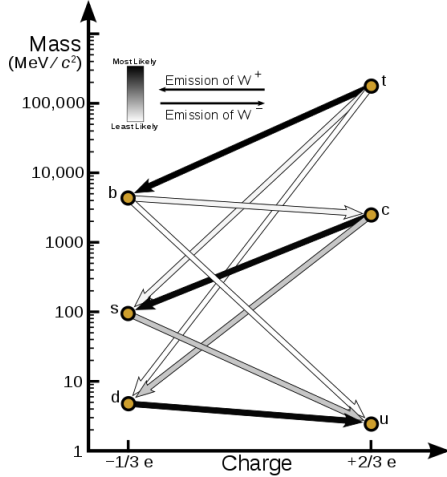


Figure 2.2: Transformations between quarks through WI. Higher generations quarks decay to first generation quarks by emitting a W boson. The arrow color indicates the likelihood of the transition according to the grey scale in the top left side which represent the CKM matrix parameters [29].

330 quark decay channels, in particular, note that quark decays are greatly favored be-
 331 tween generation members.

332

333 CKM matrix is a 3×3 unitary matrix parametrized by three mixing angles and
 334 the *CP-mixing phase*; the latter is the parameter responsible for the Charge-Parity
 335 symmetry violation (CP-violation) in the SM. The fact that the b quark decays almost
 336 all the times to a top quark is exploited in this thesis when making the selection of
 337 the signal events by requiring the presence of a jet tagged as a jet coming from a
 338 b quark in the final state. The effect of the *CP-mixing phase* on the cross section of
 339 associated production of Higgs boson and a single top process is also explored in this
 340 thesis.

Fundamental interactions.

Illustration: Typoform

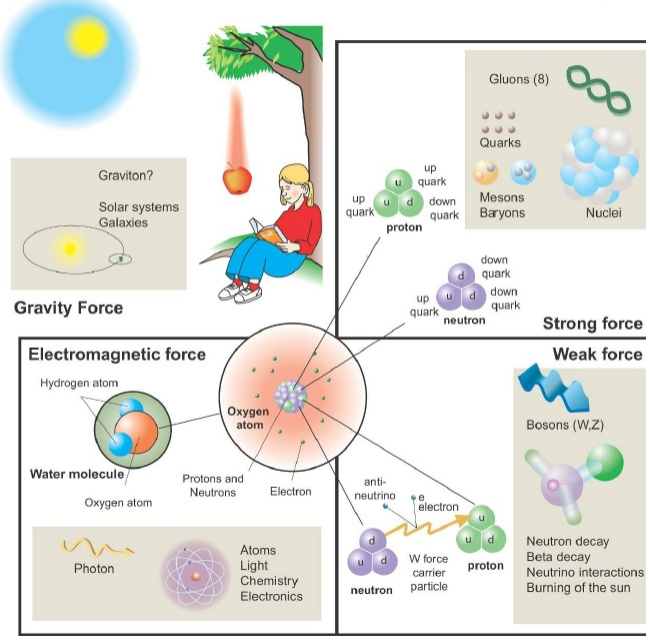


Figure 2.3: Fundamental interactions in nature. Despite the many manifestations of forces in nature, we can track all of them back to one of the fundamental interactions. The most common forces are gravity and electromagnetic given that all of us are subject and experience them in everyday life.

341 2.2.2 Fundamental interactions

342 Even though there are many manifestations of force in nature, like the ones represented in figure 2.3, we can classify all of them into one of four fundamental interactions:

- 345 • *Electromagnetic interaction (EI)* affects particles that are “electrically charged,” 346 like electrons and protons. It is described by QED combining quantum mechanics, 347 special relativity and electromagnetism in order to explain how particles 348 with electric charge interact through the exchange of photons, therefore, one 349 says that “Electromagnetic Force” is mediated by “photons”. Figure 2.4a. shows 350 a graphical representation, known as “feynman diagram”, of electron-electron

351 scattering.

- 352 • *Strong interaction (SI)* described by Quantum Chromodynamics (QCD). Hadrons
 353 like proton and neutron have internal structure given that they are composed
 354 of two or more valence quarks⁵. Quarks have fractional electric charge which
 355 means that they are subject to electromagnetic interaction and in the case of the
 356 proton they should break apart due to electrostatic repulsion; however, quarks
 357 are held together inside the hadrons against their electrostatic repulsion by the
 358 “Strong Force” through the exchange of “gluons.” The analog to the electric
 359 charge is the “color charge”. Electrons and photons are elementary particles
 360 as quarks but they don’t carry color charge, therefore they are not subject to
 361 SI. The feynman diagram for gluon exchange between quarks is shown in figure
 362 2.4b.

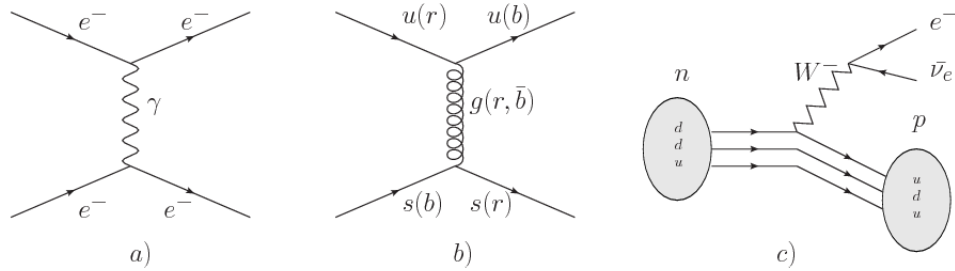


Figure 2.4: Feynman diagrams representing the interactions in SM; a) EI: e - e scattering; b) SI: gluon exchange between quarks ; c) WI: β -decay

- 363 • *Weak interaction (WI)* described by the weak theory (WT), is responsible, for
 364 instance, for the radioactive decay in atoms and proton-proton (pp) fusion
 365 within the sun. Quarks and leptons are the particles affected by the weak
 366 interaction; they possess a property called “flavor charge” (see 2.2.1) which can
 367 be changed by emitting or absorbing one weak force mediator. There are three
 368 mediators of the “weak force” known as “Z” boson in the case of electrically

⁵ particles made of four and five quarks are exotic states not so common.

369 neutral changes and “ W^\pm ” bosons in the case of electrically charged changes.
 370 The “weak isospin” is the WI analog to electric charge in EI, and color charge
 371 in SI, and defines how quarks and leptons are affected by the weak force. Figure
 372 2.4c. shows the feynman diagram of β -decay where a newtron (n) is transformed
 373 in a proton (p) by emmiting a W^- particle. Since this thesis is in the frame
 374 of the electroweak interaction, a more detailed description of it will be given in
 375 section 2.3

376 • *Gravitational interaction (GI)* described by General Theory of Relativity (GR).
 377 It is responsible for the structure of galaxies and black holes as well as the
 378 expansion of the universe. As a classical theory, in the sense that it can be for-
 379 mulated without even appeal to the concept of quantization, it implies that the
 380 spacetime is a continuum and predictions can be made without limitation to the
 381 precision of the measurement tools. The latter represent a direct contradiction
 382 of the quantum mechanics principles. Gravity is deterministic while quantum
 383 mechanics is probabilistic; despite that, efforts to develop a quantum theory of
 384 gravity have predicted the “graviton” as mediator of the Gravitational force⁶.

Interaction	Acts on	Relative strength	Range (m)	Mediators
Electromagnetic (QED)	Electrically charged particles	10^{-2}	Infinite	Photon
Strong (QCD)	Quarks and gluons	1	10^{-15}	Gluon
Weak (WI)	Leptons and quarks	10^{-6}	10^{-18}	W^\pm , Z
Gravitational (GI)	Massive particles	10^{-39}	Infinite	Graviton

Table 2.6: Fundamental interactions features [30].

385
 386 Table 2.6 summarizes the main features of the fundamental interactions. The rela-
 387 tive strength of the fundamental forces reveals the meaning of strong and weak; in

⁶ Actually a wide variety of theories have been developed in an attempt to describe gravity; some famous examples are string theory and supergravity.

388 a context where the relative strength of the SI is 1, the EI is about hundred times
 389 weaker and WI is about million times weaker than the SI. A good description on
 390 how the relative strength and range of the fundamental interactions are calculated
 391 can be found in references [30, 31]. In the everyday life, only EI and GI are explicitly
 392 experienced due to the range of these interactions; i.e., at the human scale distances
 393 only EI and GI have appreciable effects, in contrast to SI which at distances greater
 394 than 10^{-15} m become negligible.

395

396 QED was built successfully on the basis of the classical electrodynamics theory (CED)
 397 of Maxwell and Lorentz, following theoretical and experimental requirements imposed
 398 by

- 399 • lorentz invariance: independence on the reference frame.
- 400 • locallity: interacting fields are evaluated at the same space-time point to avoid
 401 action at a distance.
- 402 • renormalizability: physical predictions are finite and well defined
- 403 • particle spectrum, symmetries and conservation laws already known must emerge
 404 from the theory.
- 405 • gauge invariance.

406 The gauge invariance requirement reflects the fact that the fundamental fields cannot
 407 be directly measured but associated fields which are the observables. Electric (“**E**”)
 408 and magnetic (“**B**”) fields in CED are associated with the electric scalar potential
 409 “**V**” and the vector potential “**A**”. In particular, **E** can be obtained by measuring
 410 the change in the space of the scalar potential (ΔV); however, two scalar potentials

411 differing by a constant “f” correspond to the same electric field. The same happens in
 412 the case of the vector potential “ \mathbf{A} ”; thus, different configurations of the associated
 413 fields result in the same set of values of the observables. The freedom in choosing
 414 one particular configuration is known as “gauge freedom”; the transformation law con-
 415 necting two configurations is known as “gauge transformation” and the fact that the
 416 observables are not affected by a gauge transformation is called “gauge invariance”.

417

418 When the gauge transformation:

$$\begin{aligned} \mathbf{A} &\rightarrow \mathbf{A} - \Delta f \\ V &\rightarrow V - \frac{\partial f}{\partial t} \end{aligned} \tag{2.4}$$

419 is applied to Maxwell equations, they are still satisfied and the fields remain invariant.
 420 Thus, CED is invariant under gauge transformations and is called a “gauge theory”.
 421 The set of all gauge transformations form the “symmetry group” of the theory, which
 422 according to the group theory, has a set of “group generators”. The number of group
 423 generators determine the number of “gauge fields” of the theory.

424

425 As mentioned in the first lines of section 2.2, QED has one symmetry group ($U(1)$)
 426 with one group generator (the Q operator) and one gauge field (the electromagnetic
 427 field A^μ). In CED there is not a clear definition, beyond the historical convention, of
 428 which fields are the fundamental and which are the associated, but in QED it is clear
 429 that the fundamental field is A^μ . When a gauge theory is quantized, the gauge field
 430 is quantized and its quanta is called “gauge boson”. The word boson characterizes
 431 particles with integer spin which obey Bose-Einstein statistics.

432

433 As will be detailed in section 2.3, interactions between particles in a system can be
 434 obtained by considering first the Lagrangian density of free particles in the system,
 435 which of course is incomplete because the interaction terms have been left out, and
 436 demanding global phase transformation invariance. Global phase transformation in-
 437 variance means that a gauge transformation is performed identically to every point
 438 in the space⁷ and the Lagrangian remains invariant. Then, the global transformation
 439 is promoted to a local phase transformation (this time the gauge transformation de-
 440 pends on the position in space) and again invariance is required.

441

442 Due to the space dependence of the local transformation, the Lagrangian density is
 443 not invariant anymore. In order to restate the gauge invariance, the gauge covariant
 444 derivative is introduced in the Lagrangian and with it the gauge field responsible for
 445 the interaction between particles in the system. The new Lagrangian density is gauge
 446 invariant, includes the interaction terms needed to account for the interactions and
 447 provides a way to explain the interaction between particles through the exchange of
 448 the gauge boson.

449 This recipe was used to build QED and the theories that aim to explain the funda-
 450 mental interactions.

451 2.2.3 Gauge Bosons

452 The importance of the gauge bosons comes from the fact that they are the force
 453 mediators or force carriers. The features of the gauge bosons reflect the features of
 454 the fields they represent; these features are extracted from the Lagrangian density
 455 used to describe the interactions. In section 2.3, it will be shown how the gauge

⁷ Here space corresponds to the 4-dimensional space i.e. space-time.

456 bosons of the EI and WI emerge from the electroweak Lagrangian. The SI gauge
 457 bosons features are also extracted from the SI Lagrangian but it is not detailed in
 458 this document. The main features of the SM gauge bosons will be briefly presented
 459 below and summarized in table 2.7.

460 • **Photon.** EI occurs when the photon couples to (is exchanged between) particles
 461 carrying electric charge; however, the photon itself does not carry electric charge,
 462 therefore, there is no coupling between photons. Given that the photon is
 463 massless the EI is of infinite range, i.e., electrically charged particles interact
 464 even if they are located far away one from each other; this also implies that
 465 photons always move with the speed of light.

466 • **Gluon.** SI is mediated by gluons which, same as photons, are massless. They
 467 carry one unit of color charge and one unit of anticolor charge which means that
 468 gluons couple to other gluons. As a result, the range of the SI is not infinite
 469 but very short due to the attraction between gluons, giving rise to the “color
 470 confinement” which explains why color charged particles cannot be isolated but
 471 live within composited particles, like quarks inside protons.

472 • **W, Z.** The WI mediators, W^\pm and Z, are massive which explains their short-
 473 range. Given that the WI is the only interaction that can change the flavor
 474 of the interacting particles, the W boson is the responsible for the nuclear
 475 transmutation where a neutron is converted in a proton or vice versa with the
 476 involvement of an electron and a neutrino (see figure 2.4c). The Z boson is the
 477 responsible of the neutral weak processes like neutrino elastic scattering where
 478 no electric charge but momentum transference is involved. WI gauge bosons
 479 carry isospin charge which makes possible the interaction between them.

Interaction	Mediator	Electric charge (e)	Color charge	Weak Isospin	mass (GeV/c ²)
Electromagnetic	Photon (γ)	0	No	0	0
Strong	Gluon (g)	0	Yes -octet	No	0
Weak	W^\pm Z	± 1 0	No No	± 1 0	80.385 ± 0.015 91.188 ± 0.002

Table 2.7: SM gauge bosons main features [21].

480

481 **2.3 Electroweak unification and the Higgs**
 482 **mechanism**

483 Physicists dream of building a theory that contains all the interactions in one single
 484 interaction, i.e., showing that at some scale in energy all the four fundamental in-
 485 teractions are unified and only one interaction emerges in a “Theory of everything”.
 486 The first sign of the feasibility of such unification comes from success in the con-
 487 struction of the CED. Einstein spent years trying to reach that dream, which by
 488 1920 only involved electromagnetism and gravity, with no success; however, a new
 489 partial unification was achieved in the 1960’s, when S.Glashow [14], A.Salam [15] and
 490 S.Weinberg [16] independently proposed that electromagnetic and weak interactions
 491 are two manifestations of a more general interaction called “electroweak interaction
 492 (EWT)”. Both, QCD and EWT, were developed in parallel and following the useful
 493 prescription provided by QED and the gauge invariance principles.

494

495 The theory of weak interactions was capable of explaining the β -decay and in general
 496 the processes mediated by W^\pm bosons. However, there were some processes like the
 497 “ $\nu_\mu - e$ scattering” which would require the exchange of two W bosons (see figure 2.5
 498 top diagrams) giving rise to divergent loop integrals and then non finite predictions.

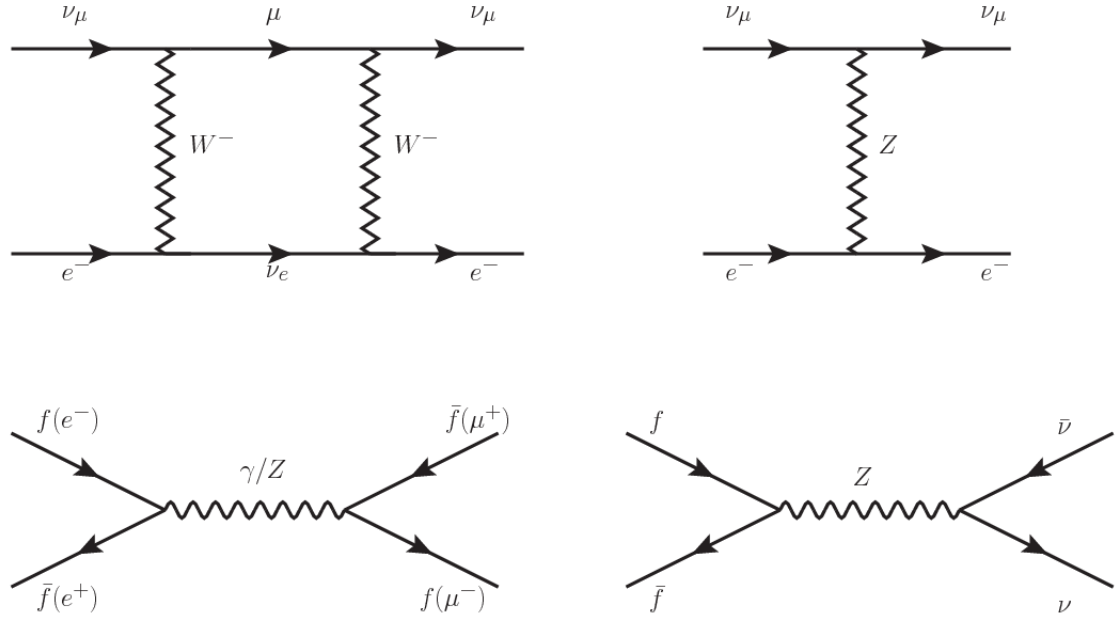


Figure 2.5: Top: $\nu_\mu - e^-$ scattering going through charged currents (left) and neutral currents (right). Bottom: neutral current processes for charged fermions (left) and involving neutrinos (right). While neutral current processes involving only charged fermions can proceed through EI or WI, those involving neutrinos can only proceed via WI.

499 By including neutral currents involving fermions via the exchange of neutral bosons
 500 Z , those divergences are compensated and the predictions become realistic.

501

502 Neutral weak interaction vertices conserve flavor in the same way as the electromag-
 503 netic vertices do, but additionally, the Z boson can couple to neutrinos which implies
 504 that processes involving charged fermions can proceed through EI or WI but processes
 505 involving neutrinos can proceed only through WI.

506

507 The prescription to build a gauge theory of the WI consists of proposing a free field
 508 Lagrangian density that includes the particles involved; next, by requesting invari-
 509 ance under global phase transformations first and generalizing to local phase trans-
 510 formations invariance later, the conserved currents are identified and interactions are

511 generated by introducing gauge fields. Given that the goal is to include the EI and
 512 WI in a single theory, the group symmetry considered should be a combination of
 513 $SU(2)_L$ and $U(1)_{em}$, however the latter cannot be used directly because the EI treats
 514 left and right-handed particles indistinctly in contrast to the former. Fortunately, the
 515 weak hypercharge, which is a combination of the weak isospin and the electric charge
 516 (eqn 2.2) is suitable to be used since it is conserved by the EI and WI. Thus, the
 517 symmetry group to be considered is

$$G \equiv SU(2)_L \otimes U(1)_Y \quad (2.5)$$

518 The following treatment applies to any of the fermion generations, but for simplicity
 519 the first generation of leptons will be considered [2, 3, 32, 33].

520

521 Given the first generation of leptons

$$\psi_1 = \begin{pmatrix} \nu_e \\ e^- \end{pmatrix}_L, \quad \psi_2 = \nu_{eR}, \quad \psi_3 = e_R^- \quad (2.6)$$

522 the charged fermionic currents are given by

$$J_\mu \equiv J_\mu^+ = \bar{\nu}_{eL} \gamma_\mu e_L, \quad J_\mu^\dagger \equiv J_\mu^- = \bar{e}_L \gamma_\mu \nu_{eL} \quad (2.7)$$

523 and the free Lagrangian is given by

$$\mathcal{L}_0 = \sum_{j=1}^3 i\bar{\psi}_j(x) \gamma^\mu \partial_\mu \psi_j(x). \quad (2.8)$$

524 Mass terms are included directly in the QED and QCD free Lagrangians since they
 525 preserve the invariance under the symmetry transformations involved which treat
 526 left-handed and right-handed similarly, however mass terms of the form

$$m_W^2 W_\mu^\dagger(x) W^\mu(x) + \frac{1}{2} m_Z^2 Z_\mu(x) Z^\mu(x) - m_e \bar{\psi}_e(x) \psi_e(x) \quad (2.9)$$

527 which represent the mass of W^\pm , Z and electrons, are not invariant under G trans-
 528 formations, therefore the gauge fields described by the EWI are in principle massless.

529

530 Experiments have shown that the gauge fields are not massless; however, they have
 531 to acquire mass through a mechanism compatible with the gauge invariance; that
 532 mechanism is known as the “Higgs mechanism” and will be considered later in this
 533 section. The global transformations in the combined symmetry group G can be
 534 written as

$$\begin{aligned} \psi_1(x) &\xrightarrow{G} \psi'_1(x) \equiv U_Y U_L \psi_1(x), \\ \psi_2(x) &\xrightarrow{G} \psi'_2(x) \equiv U_Y \psi_2(x), \\ \psi_3(x) &\xrightarrow{G} \psi'_3(x) \equiv U_Y \psi_3(x) \end{aligned} \quad (2.10)$$

535 where U_L represent the $SU(2)_L$ transformation acting only on the weak isospin dou-
 536 blet and U_Y represent the $U(1)_Y$ transformation acting on all the weak isospin mul-
 537 tiplets. Explicitly

$$U_L \equiv \exp\left(i \frac{\sigma_i}{2} \alpha^i\right), \quad U_Y \equiv \exp(i y_i \beta) \quad (i = 1, 2, 3) \quad (2.11)$$

538 with σ_i the Pauli matrices and y_i the weak hypercharges. In order to promote the
 539 transformations from global to local while keeping the invariance, it is required that
 540 $\alpha^i = \alpha^i(x)$, $\beta = \beta(x)$ and the replacement of the ordinary derivatives by the covariant
 541 derivatives

$$\begin{aligned}
D_\mu \psi_1(x) &\equiv \left[\partial_\mu + ig\sigma_i W_\mu^i(x)/2 + ig'y_1 B_\mu(x) \right] \psi_1(x) \\
D_\mu \psi_2(x) &\equiv \left[\partial_\mu + ig'y_2 B_\mu(x) \right] \psi_2(x) \\
D_\mu \psi_3(x) &\equiv \left[\partial_\mu + ig'y_3 B_\mu(x) \right] \psi_3(x)
\end{aligned} \tag{2.12}$$

542 introducing in this way four gauge fields, $W_\mu^i(x)$ and $B_\mu(x)$, in the process. The
543 covariant derivatives (eqn 2.12) are required to transform in the same way as fermion
544 fields $\psi_i(x)$ themselves, therefore, the gauge fields transform as:

$$\begin{aligned}
B_\mu(x) &\xrightarrow{G} B'_\mu(x) \equiv B_\mu(x) - \frac{1}{g'} \partial_\mu \beta(x) \\
W_\mu^i(x) &\xrightarrow{G} W_\mu^{i\prime}(x) \equiv W_\mu^i(x) - \frac{i}{g} \partial_\mu \alpha_i(x) - \varepsilon_{ijk} \alpha_i(x) W_\mu^j(x).
\end{aligned} \tag{2.13}$$

545 The G invariant version of the Lagrangian density 2.8 can be written as

$$\mathcal{L}_0 = \sum_{j=1}^3 i\bar{\psi}_j(x) \gamma^\mu D_\mu \psi_j(x) \tag{2.14}$$

546 where free massless fermion and gauge fields and fermion-gauge boson interactions
547 are included. The EWI Lagrangian density must additionally include kinetic terms
548 for the gauge fields (\mathcal{L}_G) which are built from the field strengths, according to

$$B_{\mu\nu}(x) \equiv \partial_\mu B_\nu - \partial_\nu B_\mu \tag{2.15}$$

$$W_{\mu\nu}^i(x) \equiv \partial_\mu W_\nu^i(x) - \partial_\nu W_\mu^i(x) - g\varepsilon^{ijk} W_\mu^j W_\nu^k \tag{2.16}$$

549 the last term in eqn. 2.16 is added in order to hold the gauge invariance; therefore,

$$\mathcal{L}_G = -\frac{1}{4}B_{\mu\nu}(x)B^{\mu\nu}(x) - \frac{1}{4}W_{\mu\nu}^i(x)W_i^{\mu\nu}(x) \quad (2.17)$$

550 which contains not only the free gauge fields contributions, but also the gauge fields
 551 self-interactions and interactions among them.

552

553 The three weak isospin conserved currents resulting from the $SU(2)_L$ symmetry are
 554 given by

$$J_\mu^i(x) = \frac{1}{2}\bar{\psi}_1(x)\gamma_\mu\sigma^i\psi_1(x) \quad (2.18)$$

555 while the weak hypercharge conserved current resulting from the $U(1)_Y$ symmetry is
 556 given by

$$J_\mu^Y = \sum_{j=1}^3 \bar{\psi}_j(x)\gamma_\mu y_j \psi_j(x) \quad (2.19)$$

557 In order to evaluate the electroweak interactions modeled by an isotriplet field W_μ^i
 558 which couples to isospin currents J_μ^i with strength g and additionally the singlet
 559 field B_μ which couples to the weak hypercharge current J_μ^Y with strength $g'/2$. The
 560 interaction Lagrangian density to be considered is

$$\mathcal{L}_I = -g J^{i\mu}(x) W_\mu^i(x) - \frac{g'}{2} J^{Y\mu}(x) B_\mu(x) \quad (2.20)$$

561 Note that the weak isospin currents are not the same as the charged fermionic currents
 562 that were used to describe the WI (eqn 2.7), since the weak isospin eigenstates are
 563 not the same as the mass eigenstates, but they are closely related

$$J_\mu = \frac{1}{2}(J_\mu^1 + iJ_\mu^2), \quad J_\mu^\dagger = \frac{1}{2}(J_\mu^1 - iJ_\mu^2). \quad (2.21)$$

564 The same happens with the gauge fields W_μ^i which are related to the mass eigenstates
 565 W^\pm by

$$W_\mu^+ = \frac{1}{\sqrt{2}}(W_\mu^1 - iW_\mu^2), \quad W_\mu^- = \frac{1}{\sqrt{2}}(W_\mu^1 + iW_\mu^2). \quad (2.22)$$

566 The fact that there are three weak isospin conserved currents is an indication that in
 567 addition to the charged fermionic currents, which couple charged to neutral leptons,
 568 there should be a neutral fermionic current that couples neutral fermions or electri-
 569 cally charged fermions that have the same electric charge and thus electric charge
 570 change is not implied. The third weak isospin current contains a term that is simi-
 571 lar to the electromagnetic current (j_μ^{em}), indicating that there is a relation between
 572 them and resembling the Gell-Mann-Nishijima formula 2.2 adapted to electroweak
 573 interactions

$$Q = T_3 + \frac{Y_W}{2}. \quad (2.23)$$

574 Just as Q generates the $U(1)_{em}$ symmetry, the weak hypercharge generates the $U(1)_Y$
 575 symmetry as said before. It is possible to write the relationship in terms of the currents
 576 as

$$j_\mu^{em} = J_\mu^3 + \frac{1}{2}J_\mu^Y. \quad (2.24)$$

577 The neutral gauge fields W_μ^3 and B_μ cannot be directly identified with the Z and the
 578 photon fields since the photon interacts similarly with left and right-handed fermions;
 579 however, they are related through a linear combination given by

$$A_\mu = B_\mu \cos \theta_W + W_\mu^3 \sin \theta_W \quad (2.25)$$

$$Z_\mu = -B_\mu \sin \theta_W + W_\mu^3 \cos \theta_W$$

580 where θ_W is known as the “Weinberg angle.” The interaction Lagrangian is now given

581 by

$$\mathcal{L}_I = -\frac{g}{\sqrt{2}}(J^\mu W_\mu^+ + J^{\mu\dagger} W_\mu^-) - \left(g \sin \theta_W J_\mu^3 + g' \cos \theta_W \frac{J_\mu^Y}{2}\right) A^\mu - \left(g \cos \theta_W J_\mu^3 - g' \sin \theta_W \frac{J_\mu^Y}{2}\right) Z^\mu \quad (2.26)$$

582 the first term is the weak charged current interaction, while the second term is the

583 electromagnetic interaction under the condition

$$g \sin \theta_W = g' \cos \theta_W = e, \quad \frac{g'}{g} = \tan \theta_W \quad (2.27)$$

584 contained in the eqn.2.24; the third term is the neutral weak current.

585

586 Note that the neutral fields transformation given by the eqn. 2.25 can be written in

587 terms of the coupling constants g and g' as:

$$A_\mu = \frac{g' W_\mu^3 + g B_\mu}{\sqrt{g^2 + g'^2}}, \quad Z_\mu = \frac{g W_\mu^3 - g' B_\mu}{\sqrt{g^2 + g'^2}} \quad (2.28)$$

588 So far, the Lagrangian density describing the non-massive EWI is:

$$\mathcal{L}_{nmEWI} = \mathcal{L}_0 + \mathcal{L}_G \quad (2.29)$$

589 where fermion and gauge fields have been considered massless because their regular

590 mass terms are manifestly non invariant under G transformations; therefore, masses

591 have to be generated in a gauge invariant way. The mechanism by which this goal is
 592 achieved is known as the “Higgs mechanism” and is closely connected to the concept
 593 of “spontaneous symmetry breaking.”

594 **2.3.1 Spontaneous symmetry breaking (SSB)**

595 Figure 2.6 left shows a steel nail (top) which is subject to an external force; the form
 596 of the potential energy is also shown (bottom).

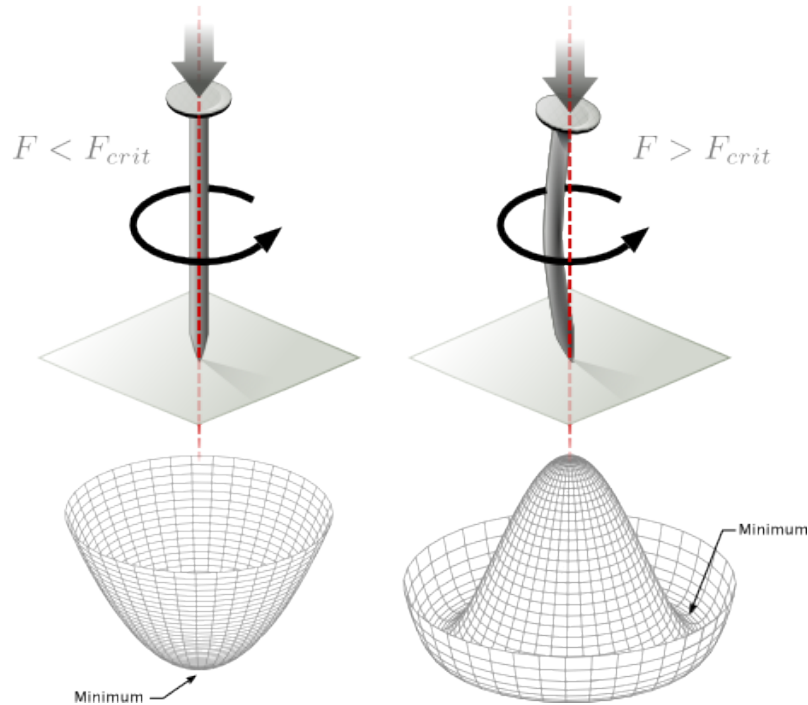


Figure 2.6: Spontaneous symmetry breaking mechanism. The steel nail, subject to an external force (top left), has rotational symmetry with respect to its axis. When the external force overcomes a critical value the nail buckles (top right) choosing a minimal energy state (ground state) and thus “*breaking spontaneously the rotational symmetry*”. The potential energy (bottom) changes but holds the rotational symmetry; however, an infinite number of asymmetric ground states are generated and circularly distributed in the bottom of the potential [34].

598 Before reaching the critical force value, the system has rotational symmetry with re-
 599 spect to the nail axis; however, after the critical force value is reached the nail buckles
 600 (top right). The form of the potential energy (bottom right) changes, preserving its
 601 rotational symmetry although its minima does not exhibit that rotational symmetry
 602 any longer. Right before the nail buckles there is no indication of the direction the
 603 nail will bend because any of the directions are equivalent, but once the nail bent,
 604 choosing a direction, an arbitrary minimal energy state (ground state) is selected and
 605 it does not share the system's rotational symmetry. This mechanism for reaching an
 606 asymmetric ground state is known as "*spontaneous symmetry breaking*".
 607 The lesson from this analysis is that the way to introduce the SSB mechanism into a
 608 system is by adding the appropriate potential to it.

609

610 Figure 2.7 shows a plot of the potential $V(\phi)$ in the case of a scalar field ϕ

$$V(\phi) = \mu^2 \phi^\dagger \phi + \lambda (\phi^\dagger \phi)^2 \quad (2.30)$$

611 If $\mu^2 > 0$ the potential has only one minimum at $\phi = 0$ and describes a scalar field
 612 with mass μ . If $\mu^2 < 0$ the potential has a local maximum at $\phi = 0$ and two minima
 613 at $\phi = \pm\sqrt{-\mu^2/\lambda}$ which enables the SSB mechanism to work.

614

615 In the case of a complex scalar field $\phi(x)$

$$\phi(x) = \frac{1}{\sqrt{2}}(\phi_1 + i\phi_2) \quad (2.31)$$

616 the Lagrangian (invariant under global $U(1)$ transformations) is given by

$$\mathcal{L} = (\partial_\mu \phi)^\dagger (\partial^\mu \phi) - V(\phi), \quad V(\phi) = \mu^2 \phi^\dagger \phi + \lambda (\phi^\dagger \phi)^2 \quad (2.32)$$

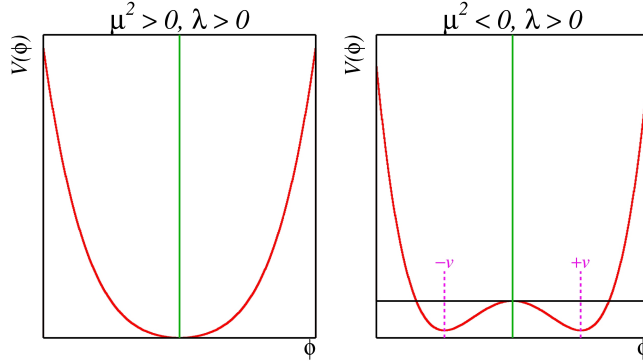


Figure 2.7: Shape of the potential $V(\phi)$ for $\lambda > 0$ and: $\mu^2 > 0$ (left) and $\mu^2 < 0$ (right). The case $\mu^2 < 0$ corresponds to the potential suitable for introducing the SSB mechanism by choosing one of the two ground states which are connected via reflection symmetry. [34].

617 where an appropriate potential has been added in order to introduce the SSB.

618

619 As seen in figure 2.8, the potential has now an infinite number of minima circularly
620 distributed along the ξ -direction which makes possible the occurrence of the SSB by
621 choosing an arbitrary ground state; for instance, $\xi = 0$, i.e. $\phi_1 = v, \phi_2 = 0$

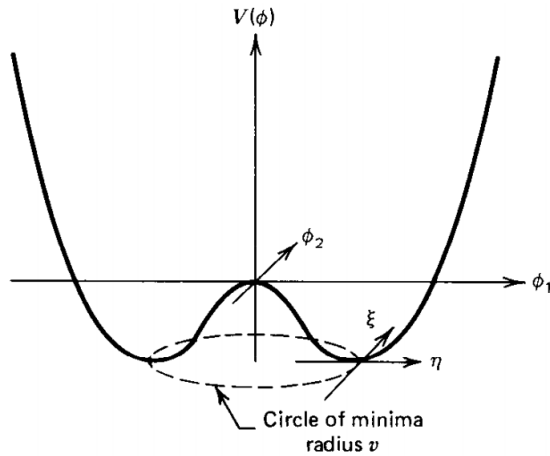


Figure 2.8: Potential for complex scalar field. There is a circle of minima of radius v along the ξ -direction [3].

$$\phi_0 = \frac{v}{\sqrt{2}} \exp(i\xi) \xrightarrow{\text{SSB}} \phi_0 = \frac{v}{\sqrt{2}} \quad (2.33)$$

622 As usual, excitations over the ground state are studied by making an expansion about
 623 it; thus, the excitation can be parametrized as:

$$\phi(x) = \frac{1}{\sqrt{2}}(v + \eta(x) + i\xi(x)) \quad (2.34)$$

624 which when substituted into eqn. 2.32 produces a Lagrangian in terms of the new
 625 fields η and ξ

$$\mathcal{L}' = \frac{1}{2}(\partial_\mu \xi)^2 + \frac{1}{2}(\partial_\mu \eta)^2 + \mu^2 \eta^2 - V(\phi_0) - \lambda v \eta (\eta^2 + \xi^2) - \frac{\lambda}{4}(\eta^2 + \xi^2)^2 \quad (2.35)$$

626 where the last two terms represent the interactions and self-interaction between the
 627 two fields η and ξ . The particular feature of the SSB mechanism is revealed when
 628 looking to the first three terms of \mathcal{L}' . Before the SSB, only the massless ϕ field is
 629 present in the system; after the SSB there are two fields of which the η -field has
 630 acquired mass $m_\eta = \sqrt{-2\mu^2}$ while the ξ -field is still massless (see figure 2.9).

631

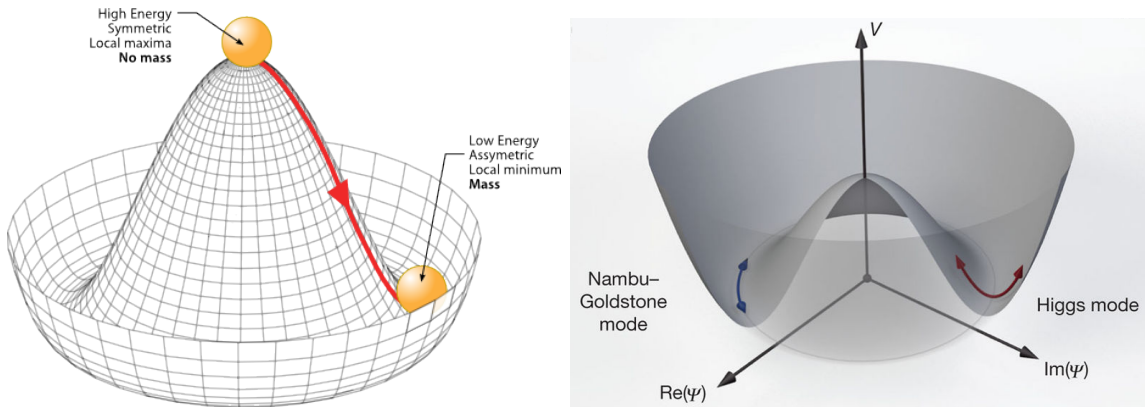


Figure 2.9: SSB mechanism for a complex scalar field [34, 35].

632 Thus, the SSB mechanism serves as a method to generate mass but as a side effect a

633 *massless field is introduced in the system.* This fact is known as the Goldstone theorem
 634 and states that a massless scalar field appears in the system for each continuous
 635 symmetry spontaneously broken. Another version of the Goldstone theorem states
 636 that “*if a Lagrangian is invariant under a continuous symmetry group G , but the*
 637 *vacuum is only invariant under a subgroup $H \subset G$, then there must exist as many*
 638 *massless spin-0 particles (Nambu-Goldstone bosons) as broken generators.*” [33] The
 639 Nambu-Goldstone boson can be understood considering that the potential in the ξ -
 640 direction is flat so excitations in that direction are not energy consuming and thus
 641 represent a massless state.

642 2.3.2 Higgs mechanism

643 When the SSB mechanism is introduced in the formulation of the EWI in an attempt
 644 to generate the mass of the so far massless gauge bosons and fermions, an interesting
 645 effect is revealed. In order to keep the G symmetry group invariance and generate
 646 the mass of the EW gauge bosons, a G invariant Lagrangian density (\mathcal{L}_S) has to be
 647 added to the non massive EWI Lagrangian (eqn. 2.29)

$$\mathcal{L}_S = (D_\mu \phi)^\dagger (D^\mu \phi) - \mu^2 \phi^\dagger \phi - \lambda (\phi^\dagger \phi)^2, \quad \lambda > 0, \mu^2 < 0 \quad (2.36)$$

$$D_\mu \phi = \left(i\partial_\mu - g \frac{\sigma_i}{2} W_\mu^i - g' \frac{Y}{2} B_\mu \right) \phi \quad (2.37)$$

648 ϕ has to be an isospin doublet of complex scalar fields so it preserves the G invariance;
 649 thus ϕ can be defined as:

$$\phi = \begin{pmatrix} \phi^+ \\ \phi^0 \end{pmatrix} \equiv \frac{1}{\sqrt{2}} \begin{pmatrix} \phi_1 + i\phi_2 \\ \phi_3 + i\phi_4 \end{pmatrix}. \quad (2.38)$$

650 The minima of the potential are defined by

$$\phi^\dagger \phi = \frac{1}{2}(\phi_1^2 + \phi_2^2 + \phi_3^2 + \phi_4^2) = -\frac{\mu^2}{2\lambda}. \quad (2.39)$$

651 The choice of the ground state is critical. By choosing a ground state, invariant under
 652 $U(1)_{em}$ gauge symmetry, the photon will remain massless and the W^\pm and Z bosons
 653 masses will be generated which is exactly what is needed. In that sense, the best
 654 choice corresponds to a weak isospin doublet with $T_3 = -1/2$, $Y_W = 1$ and $Q = 0$
 655 which defines a ground state with $\phi_1 = \phi_2 = \phi_4$ and $\phi_3 = v$:

$$\phi_0 \equiv \frac{1}{\sqrt{2}} \begin{pmatrix} 0 \\ v \end{pmatrix}, \quad v^2 \equiv -\frac{\mu^2}{\lambda}. \quad (2.40)$$

656 where the vacuum expectation value v is fixed by the Fermi coupling G_F according
 657 to $v = (\sqrt{2}G_F)^{1/2} \approx 246$ GeV.

658

659 The G symmetry has been broken and three Nambu-Goldstone bosons will appear.
 660 The next step is to expand ϕ about the chosen ground state as:

$$\phi(x) = \frac{1}{\sqrt{2}} \exp\left(\frac{i}{v} \sigma_i \theta^i(x)\right) \begin{pmatrix} 0 \\ v + H(x) \end{pmatrix} \approx \frac{1}{\sqrt{2}} \begin{pmatrix} \theta_1(x) + i\theta_2(x) \\ v + H(x) - i\theta_3(x) \end{pmatrix} \quad (2.41)$$

661 to describe fluctuations from the ground state ϕ_0 . The fields $\theta_i(x)$ represent the
 662 Nambu-Goldstone bosons while $H(x)$ is known as “higgs field.” The fundamental
 663 feature of the parametrization used is that the dependence on the $\theta_i(x)$ fields is
 664 factored out in a global phase that can be eliminated by taking the physical “unitary
 665 gauge” $\theta_i(x) = 0$. Therefore the expansion about the ground state is given by:

$$\phi(x) \frac{1}{\sqrt{2}} \begin{pmatrix} 0 \\ v + H(x) \end{pmatrix} \quad (2.42)$$

666 which when substituted into \mathcal{L}_S (eqn. 2.36) results in a Lagrangian containing the now
 667 massive three gauge bosons W^\pm, Z , one massless gauge boson (photon) and the new
 668 Higgs field (H). The three degrees of freedom corresponding to the Nambu-Goldstone
 669 bosons are now integrated into the massive gauge bosons as their longitudinal po-
 670 larizations which were not available when they were massless particles. The effect
 671 by which vector boson fields acquire mass after an spontaneous symmetry breaking,
 672 but without an explicit gauge invariance breaking is known as the “*Higgs mechanism*”.

673

674 The mechanism was proposed by three independent groups: F.Englert and R.Brout
 675 in August 1964 [36], P.Higgs in October 1964 [37] and G.Guralnik, C.Hagen and
 676 T.Kibble in November 1964 [38]; however, its importance was not realized until
 677 S.Glashow [14], A.Salam [15] and S.Weinberg [16], independently, proposed that elec-
 678 tromagnetic and weak interactions are two manifestations of a more general interac-
 679 tion called “electroweak interaction” in 1967.

680 2.3.3 Masses of the gauge bosons

681 The mass of the gauge bosons is extracted by evaluating the kinetic part of Lagrangian
 682 \mathcal{L}_S in the ground state (known also as the vacuum expectation value), i.e.,

$$\left| \left(\partial_\mu - ig \frac{\sigma_i}{2} W_\mu^i - i \frac{g'}{2} B_\mu \right) \phi_0 \right|^2 = \left(\frac{1}{2} v g \right)^2 W_\mu^+ W^{-\mu} + \frac{1}{8} v^2 (W_\mu^3, B_\mu) \begin{pmatrix} g^2 & -gg' \\ -gg' & g'^2 \end{pmatrix} \begin{pmatrix} W^{3\mu} \\ B^\mu \end{pmatrix} \quad (2.43)$$

683 comparing with the typical mass term for a charged boson $M_W^2 W^+ W^-$

$$M_W = \frac{1}{2} v g. \quad (2.44)$$

The second term in the right side of the eqn.2.43 comprises the masses of the neutral

bosons, but it needs to be written in terms of the gauge fields Z_μ and A_μ in order to be compared to the typical mass terms for neutral bosons, therefore using eqn. 2.28

$$\begin{aligned} \frac{1}{8}v^2[g^2(W_\mu^3)^2 - 2gg'W_\mu^3B^\mu + g'^2B_\mu^2] &= \frac{1}{8}v^2[gW_\mu^3 - g'B_\mu]^2 + 0[g'W_\mu^3 + gB_\mu]^2 \\ &= \frac{1}{8}v^2[\sqrt{g^2 + g'^2}Z_\mu]^2 + 0[\sqrt{g^2 + g'^2}A_\mu]^2 \end{aligned} \quad (2.45)$$

684 and then

$$M_Z = \frac{1}{2}v\sqrt{g^2 + g'^2}, \quad M_A = 0 \quad (2.46)$$

685 2.3.4 Masses of the fermions

686 The lepton mass terms can be generated by introducing a gauge invariant Lagrangian
687 term describing the Yukawa coupling between the lepton field and the Higgs field

$$\mathcal{L}_{Yl} = -G_l \left[(\bar{\nu}_l, \bar{l})_L \begin{pmatrix} \phi^+ \\ \phi^0 \end{pmatrix} l_R + \bar{l}_R (\phi^-, \bar{\phi}^0) \begin{pmatrix} \nu_l \\ l \end{pmatrix}_L \right], \quad l = e, \mu, \tau. \quad (2.47)$$

688 After the SSB and replacing the usual field expansion about the ground state (eqn.2.40)
689 into \mathcal{L}_{Yl} , the mass term arises

$$\mathcal{L}_{Yl} = -m_l(\bar{l}_L l_R + \bar{l}_R l_L) - \frac{m_l}{v}(\bar{l}_L l_R + \bar{l}_R l_L)H = -m_l \bar{l} \left(1 + \frac{H}{v} \right) \quad (2.48)$$

690

$$m_l = \frac{G_l}{\sqrt{2}}v \quad (2.49)$$

691 where the additional term represents the lepton-Higgs interaction. The quark masses
692 are generated in a similar way as lepton masses but for the upper member of the

693 quark doublet a different Higgs doublet is needed:

$$\phi_c = -i\sigma_2\phi^* = \begin{pmatrix} -\bar{\phi}^0 \\ \phi^- \end{pmatrix}. \quad (2.50)$$

694 Additionally, given that the quark isospin doublets are not constructed in terms of
 695 the mass eigenstates but in terms of the flavor eigenstates, as shown in table 2.5, the
 696 coupling parameters will be related to the CKM matrix elements; thus the quark
 697 Lagrangian is given by:

$$\mathcal{L}_{Yq} = -G_d^{i,j}(\bar{u}_i, \bar{d}_i)_L \begin{pmatrix} \phi^+ \\ \phi^0 \end{pmatrix} d_{jR} - G_u^{i,j}(\bar{u}_i, \bar{d}_i)_L \begin{pmatrix} -\bar{\phi}^0 \\ \phi^- \end{pmatrix} u_{jR} + h.c. \quad (2.51)$$

698 with $i,j=1,2,3$. After SSB and expansion about the ground state, the diagonal form
 699 of \mathcal{L}_{Yq} is:

$$\mathcal{L}_{Yq} = -m_d^i \bar{d}_i d_i \left(1 + \frac{H}{v} \right) - m_u^i \bar{u}_i u_i \left(1 + \frac{H}{v} \right) \quad (2.52)$$

700 Fermion masses depend on arbitrary couplings G_l and $G_{u,d}$ and are not predicted by
 701 the theory.

702 2.3.5 The Higgs field

703 After the characterization of the fermions and gauge bosons as well as their interac-
 704 tions, it is necessary to characterize the Higgs field itself. The Lagrangian \mathcal{L}_S in eqn.
 705 2.3.6 written in terms of the gauge bosons is given by

$$\mathcal{L}_S = \frac{1}{4}\lambda v^4 + \mathcal{L}_H + \mathcal{L}_{HV} \quad (2.53)$$

706

$$\mathcal{L}_H = \frac{1}{2}\partial_\mu H \partial^\mu H - \frac{1}{2}m_H^2 H^2 - \frac{1}{2v}m_H^2 H^3 - \frac{1}{8v^2}m_H^2 H^4 \quad (2.54)$$

707

$$\mathcal{L}_{HV} = m_H^2 W_\mu^+ W^{\mu-} \left(1 + \frac{2}{v}H + \frac{2}{v^2}H^2 \right) + \frac{1}{2}m_Z^2 Z_\mu Z^\mu \left(1 + \frac{2}{v}H + \frac{2}{v^2}H^2 \right) \quad (2.55)$$

708 The mass of the Higgs boson is deduced as usual from the mass term in the Lagrangian
 709 resulting in:

$$m_H = \sqrt{-2\mu^2} = \sqrt{2\lambda}v \quad (2.56)$$

710 however, it is not predicted by the theory either. The experimental efforts to find the
 711 Higgs boson, carried out by the CMS and ATLAS experiments⁸, gave great results
 712 by July of 2012 when the discovery of a new particle compatible with the Higgs
 713 boson predicted by the electroweak theory [39, 40] was announced. Although at the
 714 announcement time there were some reservations about calling the new particle the
 715 “Higgs boson”, today this name is widely accepted. The Higgs mass measurement,
 716 reported by both experiments [41], is in table 2.8.

Property	Value
Electric charge	0
Colour charge	0
Spin	0
Weak isospin	-1/2
Weak hypercharge	1
Parity	1
Mass (GeV/c ²)	125.09±0.21 (stat.)±0.11 (syst.)

Table 2.8: Higgs boson properties. Higgs mass is not predicted by the theory and the value here corresponds to the experimental measurement.

717

718 2.3.6 Higgs boson production mechanisms at LHC.

719 At LHC, Higgs boson is produced as a result of the collision of two counter-rotating
 720 protons beams. A detailed description of the LHC machine will be presented in
 721 chapter 3. “The total cross section” is a parameter that quantifies the number of pp
 722 collisions that happen when a number of protons are fired at each other. Different

⁸ CMS stands for Compact Muon Solenoid; ATLAS stand for A Toroidal LHC Apparatus. Both are general experiments held at the Large Hadron Collider(LHC)

723 results can be obtained after a pp collision and for each one the “cross section” is
724 defined as the number of pp collisions that conclude in that particular result with
respect to the number of protons fired at each other.

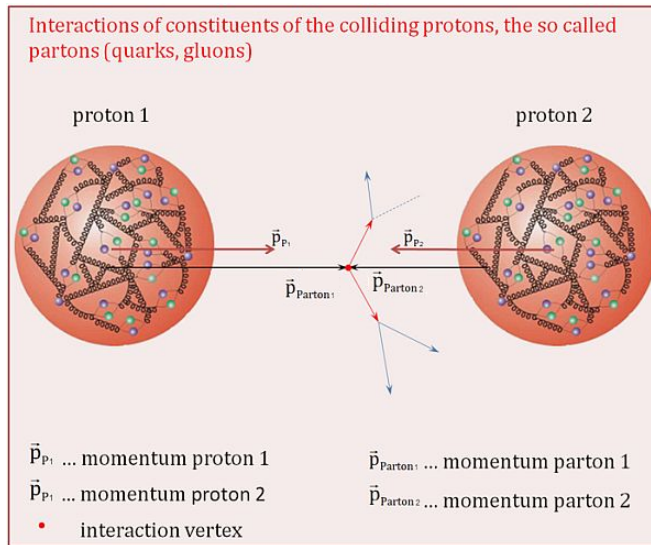


Figure 2.10: Proton-proton collision. Protons are composed of 3 valence quarks, a sea of quarks and gluons; therefore in a proton-proton collision, quarks and gluons are those who collide. [45].

725 Protons are composed of quarks and these quarks are bound by gluons; however,
726 what is commonly called the quark content of the proton makes reference to the
727 valence quarks. A sea of quarks and gluons is also present inside the proton as repre-
728 sented in figure 2.10. In a proton-proton (pp) collision, the constituents (quarks and
729 gluons) are those who collide. The pp cross section depends on the momentum of
730 the colliding particles, reason for which it is needed to know how the momentum is
731 distributed inside the proton. Quarks and gluons are known as partons and the func-
732 tions that describe how the proton momentum is distributed among partons inside it
733 are called “parton distribution functions (PDFs)”; PDFs are determined from experi-
734 mental data obtained in experiments where the internal structure of hadrons is tested.
735

736

737 In addition, in physics, a common approach to study complex systems consists in
 738 starting with a simpler version of them, for which a well known description is avail-
 739 able, and add an additional “perturbation” which represents a small deviation from
 740 the known behavior. If the perturbation is small enough, the physical quantities as-
 741 sociated with the perturbed system are expressed as a series of corrections to those
 742 of the simpler system; therefore, the more terms are considered in the series (the
 743 higher order in the perturbation series), the more precise is the the description of the
 744 complex system.

745

746 This thesis explores the Higgs production at LHC; therefore the overview presented
 747 here will be oriented specifically to the production mechanisms after pp collisions at
 748 LHC.

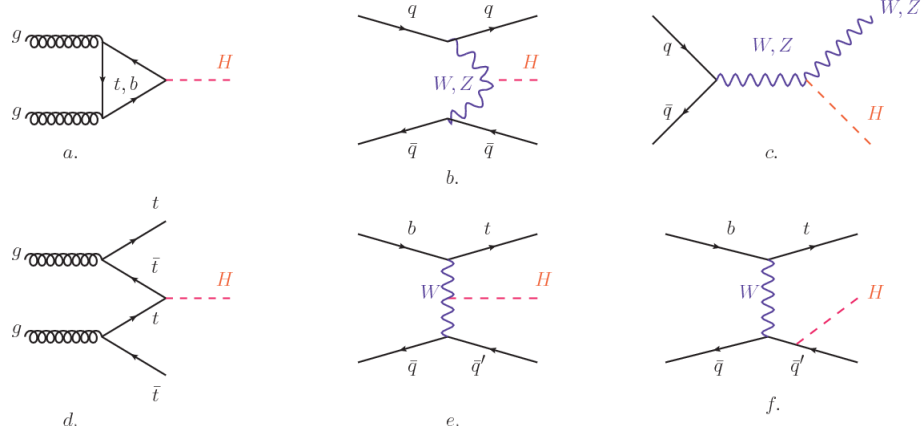


Figure 2.11: Main Higgs production mechanism Feynman diagrams. a. gluon-gluon fusion, b. vector boson fusion (VBF), c. Higgs-strahlung, d. Associated production with a top or bottom quark pair, e-f. associated production with a single top quark.

749 Figure 2.11 shows the Feynman diagrams for the leading order (first order) Higgs
 750 production processes at LHC, while the cross section for Higgs production as a func-
 751 tion of the center of mass-energy (\sqrt{s}) for pp collisions is showed in figure 2.12 left.
 752 The tags NLO (next to leading order), NNLO (next to next to leading order) and

753 N3LO (next to next to next to leading order) make reference to the order at which
 754 the perturbation series have been considered.

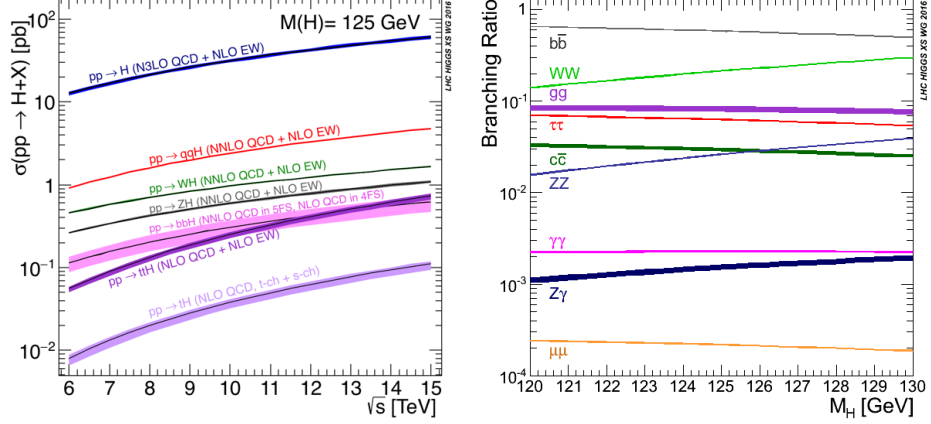


Figure 2.12: Higgs production cross sections (left) and decay branching ratios (right) for the main mechanisms. The VBF is indicated as $q\bar{q}H$ [42].

755 As shown in eqns 2.47, 2.51 and 2.55, the strength of the Higgs-fermion interaction
 756 is proportional to the fermion mass while the strength of the Higgs-gauge boson
 757 interaction is proportional to the square of the gauge boson mass, which implies
 758 that the Higgs production and decay mechanisms are dominated by couplings $H -$
 759 (W, Z, t, b, τ) .

760 The main production mechanism is the gluon fusion (figure 2.11a and $pp \rightarrow H$ in figure
 761 2.12) given that gluons carry the highest fraction of momentum of the protons in pp
 762 colliders. Since the Higgs boson does not couple to gluons, the mechanism proceeds
 763 through the exchange of a virtual top-quark loop given that for it the coupling is
 764 the biggest. Note that in this process, the Higgs boson is produced alone, which
 765 makes this mechanism experimentally clean when combined with the two-photon or
 766 the four-lepton decay channels (see section 2.3.7).

767 Vector boson fusion (figure 2.11b and $pp \rightarrow q\bar{q}H$ in figure 2.12) has the second largest
 768 production cross section. The scattering of two fermions is mediated by a weak

769 gauge boson which later emits a Higgs boson. In the final state, the two fermions
 770 tend to be located in a particular region of the detector which is used as a signature
 771 when analyzing the datasets provided by the experiments. More details about how
 772 to identify events of interest in an analysis will be given in chapter 4.

773 The next production mechanism is Higgs-strahlung (figure 2.11c and $pp \rightarrow WH, pp \rightarrow$
 774 ZH in figure 2.12) where two fermions annihilate to form a weak gauge boson. If the
 775 initial fermions have enough energy, the emergent boson eventually will emit a Higgs
 776 boson.

777 The associated production with a top or bottom quark pair and the associated pro-
 778 duction with a single top quark (figure 2.11d-f and $pp \rightarrow bbH, pp \rightarrow t\bar{t}H, pp \rightarrow tH$
 779 in figure 2.12) have a smaller cross section than the main three mechanisms above,
 780 but they provide a good opportunity to test the Higgs-top coupling. The analysis
 781 reported in this thesis is developed using these production mechanisms. A detailed
 782 description of the tH mechanism will be given in section 2.4.

783 2.3.7 Higgs decay channels

784 When a particle can decay through several modes, also known as channels, the
 785 probability of decaying through a given channel is quantified by the “branching ratio
 786 (BR)” of the decay channel; thus, the BR is defined as the ratio of number of decays
 787 going through that given channel to the total number of decays. In regard to the
 788 Higgs boson decay, the BR can be predicted with accuracy once the Higgs mass is
 789 known [43, 44]. In figure 2.12 right, a plot of the BR as a function of the Higgs mass
 790 is presented. The largest predicted BR corresponds to the $b\bar{b}$ pair decay channel (see
 791 table 2.9).

Decay channel	Branching ratio	Rel. uncertainty
$H \rightarrow bb$	5.84×10^{-1}	$+3.2\% - 3.3\%$
$H \rightarrow W^+W^-$	2.14×10^{-1}	$+4.3\% - 4.2\%$
$H \rightarrow \tau^+\tau^-$	6.27×10^{-2}	$+5.7\% - 5.7\%$
$H \rightarrow ZZ$	2.62×10^{-2}	$+4.3\% - 4.1\%$
$H \rightarrow \gamma\gamma$	2.27×10^{-3}	$+5.0\% - 4.9\%$
$H \rightarrow Z\gamma$	1.53×10^{-3}	$+9.0\% - 8.9\%$
$H \rightarrow \mu^+\mu^-$	2.18×10^{-4}	$+6.0\% - 5.9\%$

Table 2.9: Predicted branching ratios and the relative uncertainty for a SM Higgs boson with $m_H = 125 GeV/c^2$. [21]

793 **2.4 Associated Production of Higgs Boson and**
 794 **Single Top Quark.**

795 Associated production of Higgs boson has been extensively studied [46–50]. While
 796 measurements of the main Higgs production mechanisms rates are sensitive to the
 797 strength of the Higgs coupling to W boson or top quark, they are not sensitive to the
 798 relative sign between the two couplings. In this thesis, the Higgs boson production
 799 mechanism explored is the associated production with a single top quark (*th*) which
 800 offers sensitiveness to the relative sign of the Higgs couplings to W boson and to top
 801 quark. The description given here is based on the reference [48]

802
 803 A process where two incoming particles interact and produce a final state with two
 804 particles can proceed in three ways also called channels (see, for instance, figure 2.13
 805 ommiting the red line). The t-channel represents processes where an intermediate
 806 particle is emitted by one of the incoming particles and absorbed by the other. The
 807 s-channel represents processes where the two incoming particles merge into an inter-
 808 mediate particle which eventually will split into the particles in the final state. The
 809 third channel, u-channel, is similar to the t-channel but the two outgoing particles

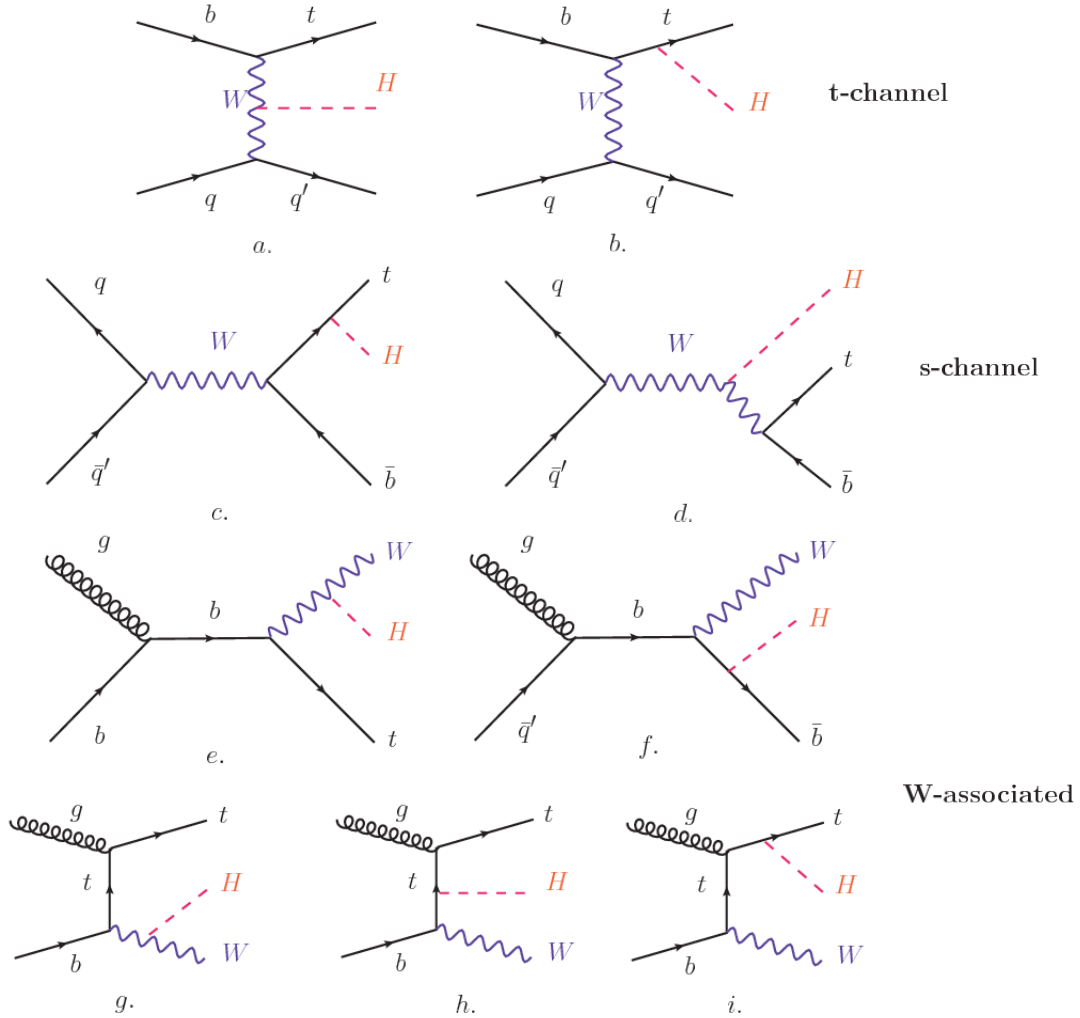


Figure 2.13: Associated higgs production mechanism Feynman diagrams. a.,b. t-channel (tHq), c.,d. s-channel (tHb), e.-i. W-associated.

810 interchange their roles.

811

812 The th production, where Higgs boson can be radiated either from the top quark or
 813 from the W boson, is represented by the leading order Feynman diagrams in figure
 814 2.13. The cross section for the th process is calculated, as usual, summing over
 815 the contributions from the different feynman diagrams; therefore it depends on the
 816 interference between the contributions. In the SM, the interference for t-channel (tHq

817 process) and W-associated (tHW process) production is destructive [46] resulting in
 818 the small cross sections presented in table 2.10.

tH production channel	Cross section (fb)
t-channel ($pp \rightarrow tHq$)	$70.79^{+2.99}_{-4.80}$
W-associated ($pp \rightarrow tHW$)	$15.61^{+0.83}_{-1.04}$
s-channel($pp \rightarrow tHb$)	$2.87^{+0.09}_{-0.08}$

Table 2.10: Predicted SM cross sections for tH production at $\sqrt{s} = 13$ TeV [51, 52].

819

820 While the s-channel contribution can be neglected, it will be shown that a deviation
 821 from the SM destructive interference would result in an enhancement of the th cross
 822 section compared to that in SM, which could be used to get information about the
 823 sign of the Higgs-top coupling [48, 49]. In order to describe th production processes,
 824 Feynman diagram 2.13b will be considered; there, the W boson is radiated by a
 825 quark in the proton and eventually it will interact with the b quark. In the high
 826 energy regime, the effective W approximation [53] allows to describe the process as
 827 the emmision of an approximately on-shell W and its hard scattering with the b
 828 quark; i.e. $Wb \rightarrow th$. The scattering amplitude for the process is given by

$$\mathcal{A} = \frac{g}{\sqrt{2}} \left[(\kappa_t - \kappa_V) \frac{m_t \sqrt{s}}{m_W v} A \left(\frac{t}{s}, \varphi; \xi_t, \xi_b \right) + \left(\kappa_V \frac{2m_W s}{v} \frac{1}{t} + (2\kappa_t - \kappa_V) \frac{m_t^2}{m_W v} \right) B \left(\frac{t}{s}, \varphi; \xi_t, \xi_b \right) \right], \quad (2.57)$$

829 where $\kappa_V \equiv g_{HVV}/g_{HVV}^{SM}$ and $\kappa_t \equiv g_{Ht}/g_{Ht}^{SM} = y_t/y_t^{SM}$ are scaling factors that quan-
 830 tify possible deviations of the couplings, Higgs-Vector boson (H-W) and Higgs-top
 831 (H-t) respectively, from the SM couplings; $s = (p_W + p_b)^2$, $t = (p_W - p_H)^2$, φ is the
 832 Higgs azimuthal angle around the z axis taken parallel to the direction of motion of

the incoming W; A and B are functions describing the weak interaction in terms of the chiral states of the quarks b and t. Terms that vanish in the high energy limit have been neglected as well as the Higgs and b quark masses⁹.

836

837 The scattering amplitude grows with energy like \sqrt{s} for $\kappa_V \neq \kappa_t$, in contrast to
 838 the SM ($\kappa_t = \kappa_V = 1$), where the first term in 2.57 cancels out and the amplitude
 839 is constant for large s; therefore, a deviation from the SM predictions represents an
 840 enhancement in the tHq cross section. In particular, for a SM H-W coupling and a H-t
 841 coupling of inverted sign with respect to the SM ($\kappa_V = -\kappa_t = 1$) the tHq cross section
 842 is enhanced by a factor greater 10 as seen in the figure 2.14 taken from reference [48];
 843 reference [54] has reported similar enhancement results.

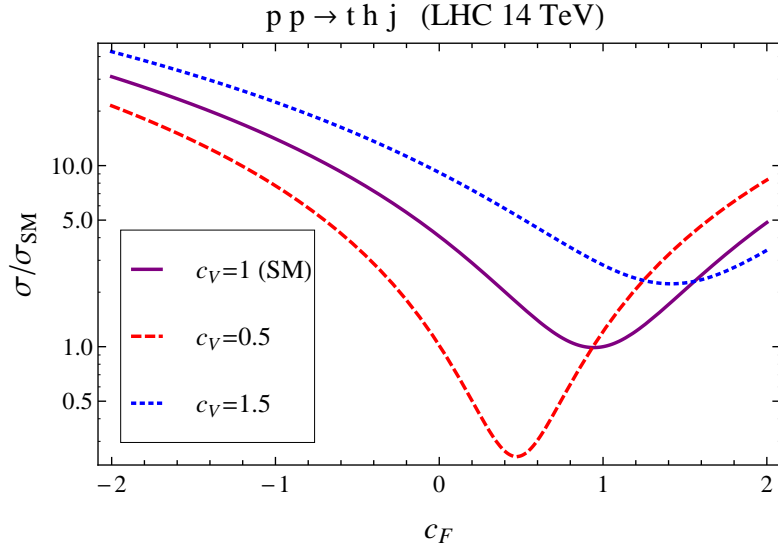


Figure 2.14: Cross section for tHq process as a function of κ_t , normalized to the SM, for three values of κ_V . In the plot c_f refers to the Higgs-fermion coupling which is dominated by the H-t coupling and represented here by κ_t . Solid, dashed and dotted lines correspond to $c_V \rightarrow \kappa_V = 1, 0.5, 1.5$ respectively. Note that for the SM ($\kappa_V = \kappa_t = 1$), the destructive effect of the interference is maximal.

⁹ A detailed explanation of the structure and approximations used to derive \mathcal{A} can be found in reference [48]

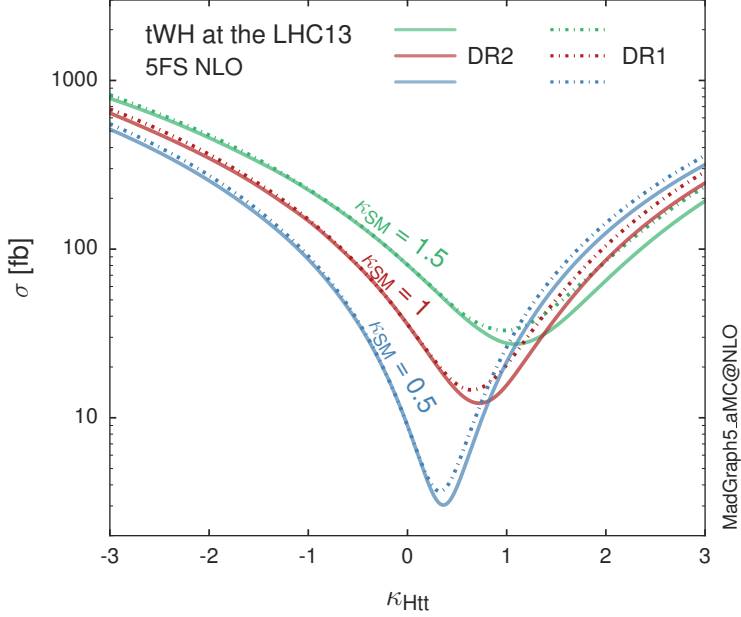


Figure 2.15: Cross section for tHW process as a function of κ_{Htt} , for three values of κ_{SM} at $\sqrt{s} = 13$ TeV. $\kappa_{Htt}^2 = \sigma_{Htt}/\sigma_{Htt}^{SM}$ is a simple rescaling of the SM Higgs interactions.

844 A similar analysis is valid for the W-associated channel but, in that case, the inter-
 845 ference is more complicated since there are more than two contributions and an ad-
 846 ditional interference with the production of Higgs boson and a top pair process($t\bar{t}H$).
 847 The calculations are made using the so-called Diagram Removal (DR) technique where
 848 interfering diagrams are removed (or added) from the calculations in order to evaluate
 849 the impact of the removed contributions. DR1 was defined to neglect $t\bar{t}H$ interference
 850 while DR2 was defined to take $t\bar{t}H$ interference into account [55]. As shown in figure
 851 2.15, the tHW cross section is enhanced from about 15 fb (SM: $\kappa_{Htt} = 1$) to about
 852 150 fb ($\kappa_{Htt} = -1$). Differences between curves for DR1 and DR2 help to gauge the
 853 impact of the interference with $t\bar{t}H$.
 854 Results of the calculations of the tHq and tHW cross sections at $\sqrt{s} = 13$ TeV can be
 855 found in reference [56] and a summary of the results is presented in table 2.11.

	\sqrt{s} TeV	$\kappa_t = 1$	$\kappa_t = -1$
$\sigma^{LO}(tHq)(\text{fb})$ [48]	8	≈ 17.4	≈ 252.7
	14	≈ 80.4	≈ 1042
$\sigma^{NLO}(tHq)(\text{fb})$ [48]	8	$18.28^{+0.42}_{-0.38}$	$233.8^{+4.6}_{-0.0}$
	14	$88.2^{+1.7}_{-0.0}$	$982.8^{+28}_{-0.0}$
$\sigma^{LO}(tHq)(\text{fb})$ [54]	14	≈ 71.8	≈ 893
$\sigma^{LO}(tHW)(\text{fb})$ [54]	14	≈ 16.0	≈ 139
$\sigma^{NLO}(tHq)(\text{fb})$ [56]	8	$18.69^{+8.62\%}_{-17.13\%}$	-
	13	$74.25^{+7.48\%}_{-15.35\%}$	$848^{+7.37\%}_{-13.70\%}$
	14	$90.10^{+7.34\%}_{-15.13\%}$	$1011^{+7.24\%}_{-13.39\%}$
$\sigma^{LO}(tHW)(\text{fb})$ [55]	13	$15.77^{+15.91\%}_{-15.76\%}$	-
$\sigma^{NLO}DR1(tHW)(\text{fb})$ [55]	13	$21.72^{+6.52\%}_{-5.24\%}$	≈ 150
$\sigma^{NLO}DR2(tHW)(\text{fb})$ [55]	13	$16.28^{+7.34\%}_{-15.13\%}$	≈ 150

Table 2.11: Predicted enhancement of the tHq and tHW cross sections at LHC for $\kappa_V = 1$ and $\kappa_t = \pm 1$ at LO and NLO; the cross section enhancement of more than a factor of 10 is due to the flipping in the sign of the H-t coupling with respect to the SM one.

857 2.5 The CP-mixing in tH processes

858 In addition to the sensitivity to sign of the H-t coupling, tHq and tHW processes have
859 been proposed as a tool to investigate the possibility of a H-t coupling that does not
860 conserve CP [50, 55, 57]. Current experimental results are consistent with SM H-V
861 and H-t couplings; however, negative H-t coupling is not excluded completely [60].

862

863 In this thesis, the sensitivity of th processes to CP-mixing is also studied in the
864 effective field theory framework and based in references [50, 55]; a generic particle
865 (X_0) of spin-0 and a general CP violating interaction with the top quark, can couple
866 to scalar and pseudoscalar fermionic densities. The H-W interaction is assumed to
867 be SM-like. The Lagrangian modeling the H-t interaction is given by

$$\mathcal{L}_0^t = -\bar{\psi}_t (c_\alpha \kappa_{Htt} g_{Htt} + i s_\alpha \kappa_{Att} g_{Att} \gamma_5) \psi_t X_0, \quad (2.58)$$

868 where α is the CP-mixing phase, $c_\alpha \equiv \cos \alpha$ and $s_\alpha \equiv \sin \alpha$, κ_{Htt} and κ_{Att} are real
 869 dimensionless rescaling parameters¹⁰, $g_{Htt} = g_{Att} = m_t/v = y_t/\sqrt{2}$ and $v \sim 246$ GeV
 870 is the Higgs vacuum expectation value. In this parametrization, it is easy to recover
 871 three special cases

- 872 • CP-even coupling $\rightarrow \alpha = 0^\circ$
- 873 • CP-odd coupling $\rightarrow \alpha = 90^\circ$
- 874 • SM coupling $\rightarrow \alpha = 0^\circ$ and $\kappa_{Htt} = 1$

875 The loop induced X_0 coupling to gluons can also be described in terms of the
 876 parametrization above, according to

$$\mathcal{L}_0^g = -\frac{1}{4} \left(c_\alpha \kappa_{Hgg} g_{Hgg} G_{\mu\nu}^a G^{a,\mu\nu} + s_\alpha \kappa_{Agg} g_{Agg} G_{\mu\nu}^a \tilde{G}^{a,\mu\nu} \right) X_0. \quad (2.59)$$

877 where $g_{Hgg} = -\alpha_s/3\pi v$ and $g_{Agg} = \alpha_s/2\pi v$. Under the assumption that the top quark
 878 dominates the gluon-fusion process at LHC energies, $\kappa_{Hgg} \rightarrow \kappa_{Htt}$ and $\kappa_{Agg} \rightarrow \kappa_{Att}$,
 879 so that the ratio between the gluon-gluon fusion cross section for X_0 and for the SM
 880 Higgs prediction can be written as

$$\frac{\sigma_{NLO}^{gg \rightarrow X_0}}{\sigma_{NLO,SM}^{gg \rightarrow H}} = c_\alpha^2 \kappa_{Htt}^2 + s_\alpha^2 \left(\kappa_{Att} \frac{g_{Agg}}{g_{Hgg}} \right)^2. \quad (2.60)$$

881 If the rescaling parameters are set to

$$\kappa_{Htt} = 1, \quad \kappa_{Att} = \left| \frac{g_{Hgg}}{g_{Agg}} \right| = \frac{2}{3}. \quad (2.61)$$

882 the gluon-fusion SM cross section is reproduced for every value of the CP-mixing
 883 angle α ; therefore, by imposing that condition to the Lagrangian density 2.58, the

¹⁰ analog to κ_t and κ_V

CP-mixing angle is not constrained by current data. Figure 2.16 shows the NLO cross sections for t-channel tX_0 (blue) and $t\bar{t}X_0$ (red) associated production processes as a function of the CP-mixing angle α . X_0 is a generic spin-0 particle with top quark CP-violating coupling. Rescaling factors κ_{Htt} and κ_{Att} have been set to reproduce the SM gluon-fusion cross sections.

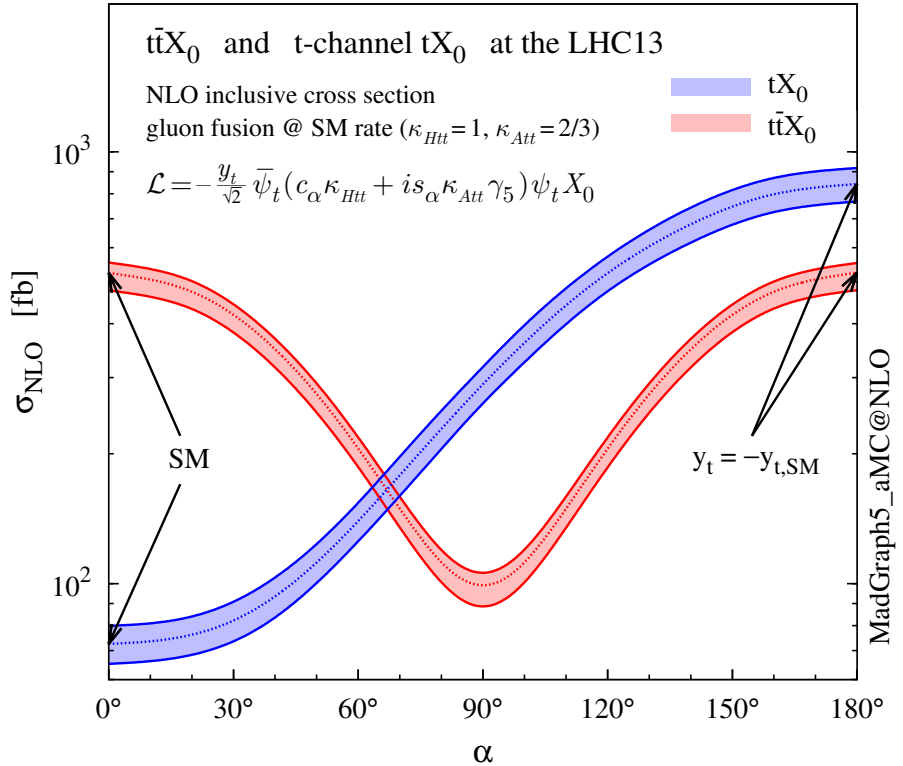


Figure 2.16: NLO cross sections for t-channel tX_0 (blue) and $t\bar{t}X_0$ (red) associated production processes as a function of the CP-mixing angle α . X_0 is a generic spin-0 particle with top quark CP-violating coupling [50].

It is interesting to notice that the tX_0 cross section is enhanced, by a factor of about 10, when a continuous rotation in the scalar-pseudoscalar plane is applied; this enhancement is similar to the enhancement produced when the H-t coupling is flipped in sign with respect to the SM ($y_t = -y_{t,SM}$ in the plot), as showed in section 2.4. In contrast, the degeneracy in the $t\bar{t}X_0$ cross section is still present given that it depends

quadratically on the H-t coupling, but more interesting is to notice that $t\bar{t}X_0$ cross section is exceeded by tX_0 cross section after $\alpha \sim 60^\circ$.

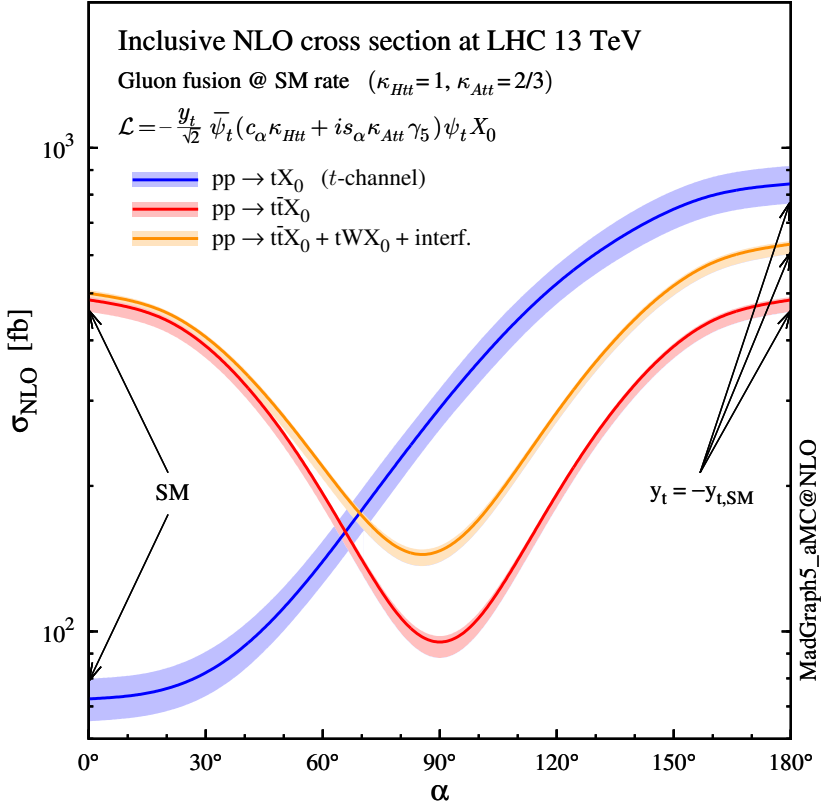


Figure 2.17: NLO cross sections for t-channel tX_0 (blue), $t\bar{t}X_0$ (red) associated production processes and combined $tWX_0 + t\bar{t}X_0$ (including interference) production as a function of the CP-mixing angle α [50].

895

896 A similar parametrization can be used to investigate the tHW process sensitivity to
 897 CP-violating H-t coupling. As said in 2.4, the interference in the W-associated chan-
 898 nel is more complicated because there are more than two contributions and also there
 899 is interference with the $t\bar{t}H$ production process.

900

901 Figure 2.17 shows the NLO cross sections for t-channel tX_0 (blue), $t\bar{t}X_0$ (red) asso-
 902 ciated production and for the combined $tWX_0 + t\bar{t}X_0 +$ interference (orange) as a
 903 function of the CP-mixing angle. It is clear that the effect of the interference in the

904 combined case is the lifting of the degeneracy present in the $t\bar{t}X_0$ production. The
905 constructive interference enhances the cross section from about 500 fb at SM ($\alpha = 0$)
906 to about 600 fb ($\alpha = 180^\circ \rightarrow y_t = -y_{t,SM}$).

907 An analysis combining tHq and tHW processes will be made in this thesis taking
908 advantage of the sensitivity improvement.

₉₀₉ **Chapter 3**

₉₁₀ **The CMS experiment at the LHC**

₉₁₁ **3.1 Introduction**

₉₁₂ Located in the Swiss-French border, the European Council for Nuclear Research
₉₁₃ (CERN) is the largest scientific organization leading the particle physics research.
₉₁₄ About 13000 people in a broad range of fields including users, students, scientists,
₉₁₅ engineers among others, contribute to the data taking and analysis, with the goal
₉₁₆ of unveiling the secrets of the nature and revealing the fundamental structure of the
₉₁₇ universe. CERN is also the home of the Large Hadron Collider (LHC), the largest
₉₁₈ circular particle accelerator around the world, where protons (or heavy ions) travel-
₉₁₉ ing close to the speed of light, are made to collide. These collisions open a window
₉₂₀ to investigate how particles (and their constituents if they are composite) interact
₉₂₁ with each other, providing clues about the laws of the nature. This chapter present
₉₂₂ an overview of the LHC structure and operation; a brief mention of the four main
₉₂₃ experiments that collect the information coming from the collisions is also included.
₉₂₄ A more detailed description of the Compact Muon Solenoid (CMS) detector is offered,
₉₂₅ given that the data used in this thesis have been taken with this detector.

926 3.2 The LHC

927 With 27 km of circumference, the LHC is currently the largest and most powerful
 928 accelerator in the world. It is installed in the same tunnel where the large Electron-
 929 Positron (LEP) collider was located, taking advantage of the existing infraestructure.
 930 The LHC is also the larger accelerator in the CERN's accelerator complex and is
 931 assisted by several successive accelerating stages before the particles are injected into
 932 the LHC ring where they reach their maximum eneregy (see figure 3.1).

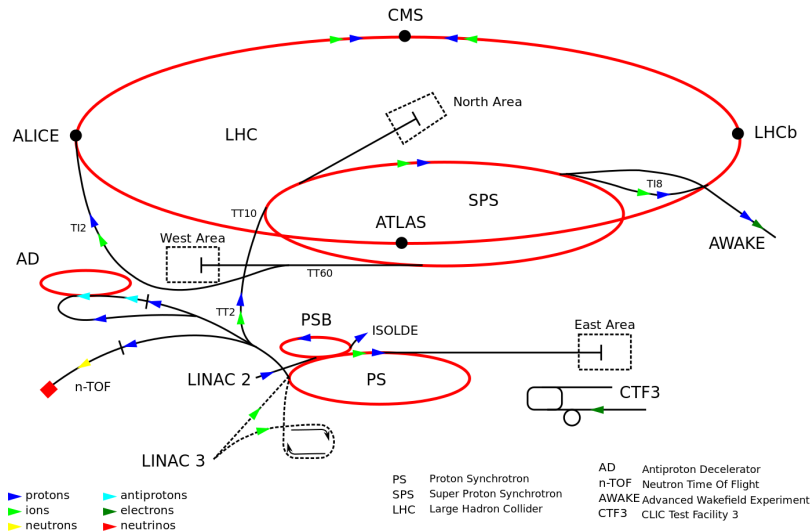


Figure 3.1: CERN accelerator complex. Blue arrows show the path followed by protons along the acceleration process [61].

933 LHC run in three modes depending on the particles being accelerated

- 934 • Proton-Proton collisions ($p\bar{p}$) for multiple physics experiments.
- 935 • Lead-Lead collisions ($Pb-Pb$) for heavy ion experiments.
- 936 • Proton-Lead collisions ($p-Pb$) for quark-gluon plasma experiments.

937 In this thesis $p\bar{p}$ collisions will be considered.

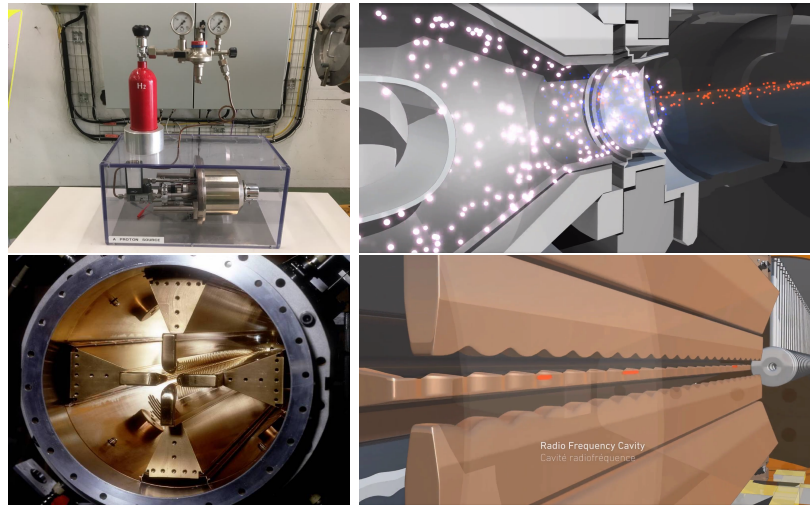


Figure 3.2: LHC protons source and first acceleration stage. Top: the bottle contains hydrogen gas (white dots) which is injected into the metal cylinder to be broken down into electrons(blue dots) and protons(red dots); Bottom: the obtained protons are directed towards the radio frequency quadrupole which perform the first acceleration, focus the beam and create the bunches of protons. [65, 66]

939 Collection of protons starts with hydrogen atoms taken from a bottle, containing hy-
 940 drogen gas, and injecting them in a metal cillinder; hydrogen atoms are broken down
 941 into electrons and protons by an intense electric field (see figure3.2 top). The result-
 942 ing protons leave the metal cylinder towards a radio frecuency quadrupole (RFQ)
 943 that focus the beam, accelerate the protons and create the packets of protons called
 944 bunches. In the RFQ, an electric field is generated by a RF wave at a frecuency that
 945 matches the resonance frecuency of the cavity where the electrodes are contained.
 946 The beam of protons traveling on the RFQ axis experience an alternating electric
 947 field gradient that generates the focusing forces.

948

949 In order to accelerate the protons, a longitudinal time-varying electric field compo-
 950 nent is added to the system; it is done by giving the electrodes a sinus-like profile as
 951 shown in figure 3.2 bottom. By matching the speed and phase of the protons with the
 952 longitudinal electric field the bunching is performed; protons synchronized with the

953 RFQ (synchronous proton) does not feel an accelerating force, but those protons in
 954 the beam that have more (or less) energy than the synchronous proton (asynchronous
 955 protons) will feel a decelerating (accelerating) force; therefore, asynchronous protons
 956 will oscillate around the synchronous ones forming bunches of protons [63]. From
 957 the RFQ emerges protons with energy 750 keV in bunches of about 1.15×10^{11} pro-
 958 tons [64].

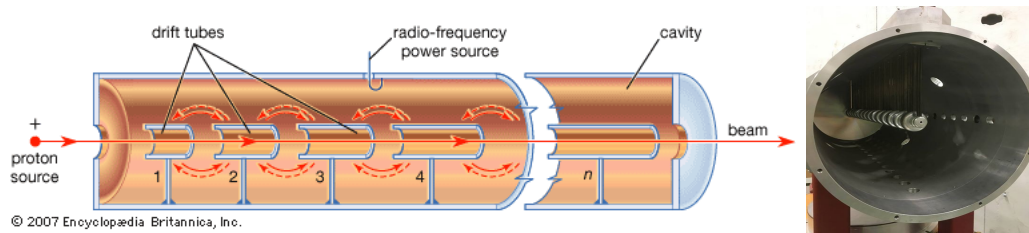


Figure 3.3: The LINAC2 accelerating system at CERN. Radio frequency (RF) generated electric fields create acceleration and deceleration zones inside the cavity; deceleration zones are blocked by drift tubes where quadrupole magnets focus the proton beam. [67]

959 Proton bunches coming from the RFQ goes to the linear accelerator 2 (LINAC2)
 960 where they are accelerated to reach 50 MeV energy. In the LINAC2 stage, acceler-
 961 ation is performed using radio frequency generated electric fields which create zones
 962 of acceleration and deceleration as shown in figure 3.3. In the decelerations zones
 963 the electric field is blocked using drift tubes where protons are free to drift while
 964 quadrupole magnets focus the beam.

965

966 The beam coming from LINAC2 is injected into the proton synchrotron booster
 967 (PSB) to reach 1.4 GeV in energy. The next acceleration is provided at the pro-
 968 ton synchrotron (PS) up to 26 GeV, followed by the injection into the super proton
 969 synchrotron (SPS) where protons are accelerated to 450 GeV. Finally, protons are
 970 injected into the LHC where they are accelerated to the target energy of 6.5 TeV.
 971 PSB, PS, SPS and LHC accelerate protons using the same RF acceleration technic

972 described before.

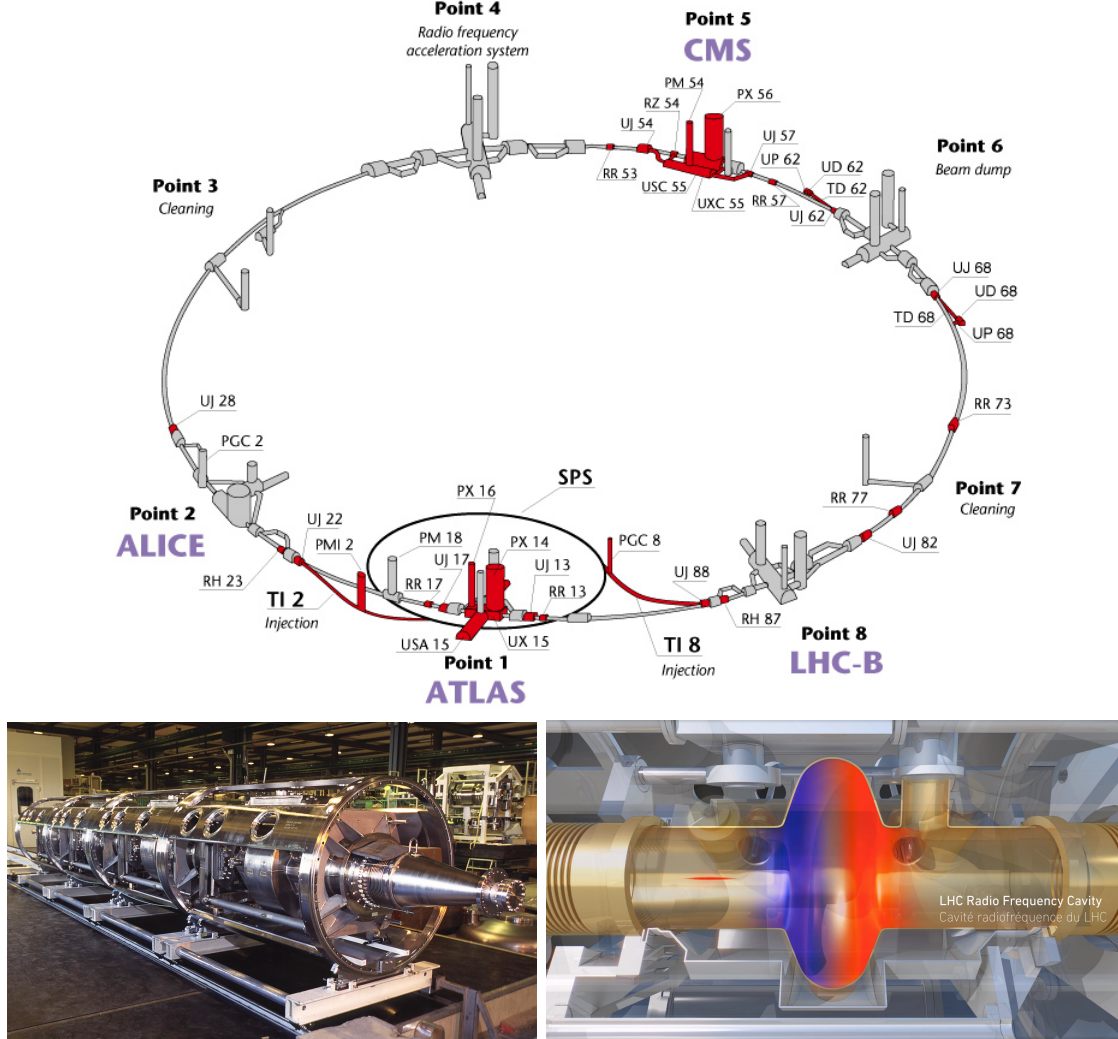


Figure 3.4: Top: LHC layout. The red zones indicate the infrastructure additions to the LEP installations, built to accomodate the ATLAS and CMS experiments which exceed the size of the former experiments located there [62]. Bottom: LHC RF cavities. A module accomodates 4 cavities that accelerate protons and preserve the bunch structure of the beam. [66,68]

973 LHC have a system of 16 RF cavities located in the so-called point 4, as shown in
 974 figure 3.4 top, tunned at a freqency of 400 MHz and the protons are carefully timed
 975 so additionally to the acceleration effect the bunch structure of the beam is preserved.
 976 Bottom side of figure 3.4 shows a picture of a Rf module composed of 4 RF cavities

977 working in a superconducting state at 4.5 K; also is showed a representation of the
 978 accelerating electric field that accelerates the protons in the bunch.

979

980 While protons are accelerated in one section of the LHC ring, where the RF cavities
 981 are located, in the rest of their path they have to be kept in the curved trajectory
 982 defined by the LHC ring. Technically, LHC is not a perfect circle; RF, injection, beam
 983 dumping, beam cleaning and sections before and after the experimental points where
 984 protons collide are all straight sections. In total, there are 8 arcs 2.45 Km long each
 985 and 8 straight sections 545 m long each. In order to curve the proton's trajectory in
 986 the arc sections, superconducting dipole magnets are used.

987

988 Inside the LHC ring, there are two proton beams traveling in opposite directions in
 989 two separated beam pipes; the beam pipes are kept at ultra high vacuum ($\sim 10^{-9}$
 990 Pa) to ensure that there are no particles that interact with the proton beams. The
 991 superconducting dipole magnets used in LHC are made of a NbTi alloy, capable of
 992 transporting currents of about 12000 A when cooled at a temperature below 2K using
 993 liquid helium (see figure 3.5).

994 Protons in the arc sections of LHC feel a centripetal force exerted by the dipole
 995 magnets which is perpendicular to the beam trajectory; The magnitude of magnetic
 996 field needed can be found assuming that protons travel at $v \approx c$, using the standard
 997 values for proton mass and charge and the LHC radius, as

$$F_m = \frac{mv^2}{r} = qBv \quad \rightarrow B = 8.33T \quad (3.1)$$

998 which is about 100000 times the Earth's magnetic field. A representation of the mag-
 999 netic field generated by the dipole magnets is shown in the bottom left side of figure

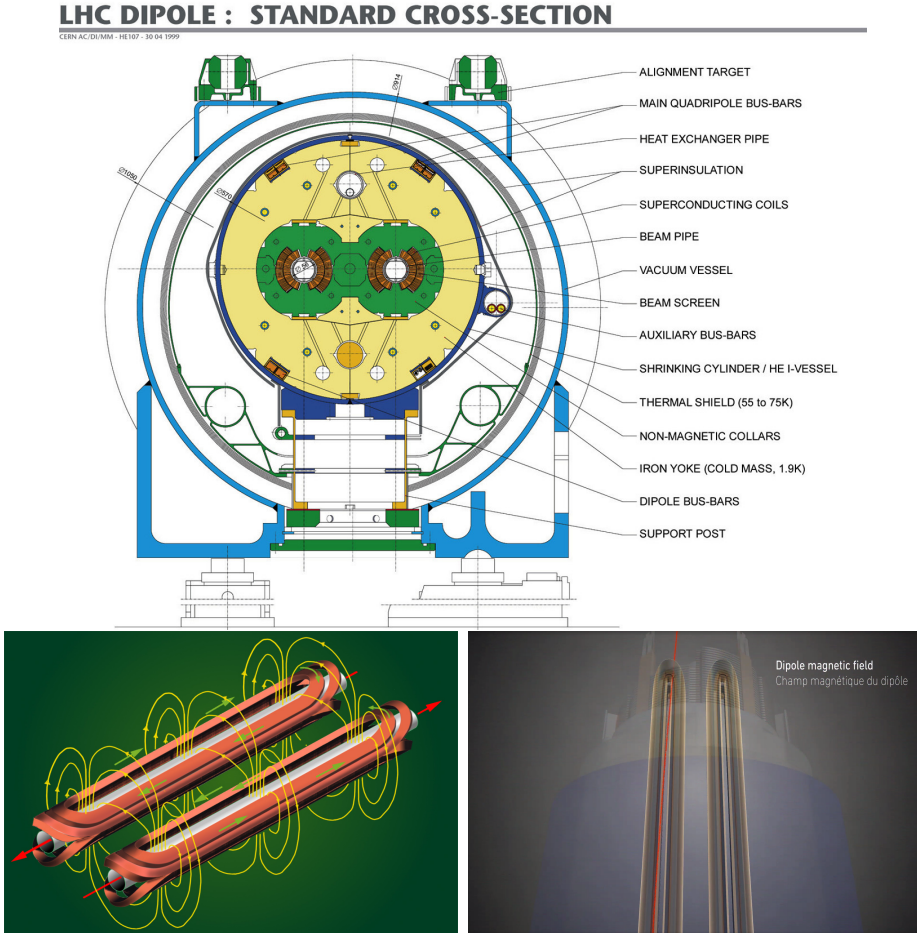


Figure 3.5: Top: LHC dipole magnet transversal view; cooling, shielding and mechanical support are indicated. Bottom left: Magnetic field generated by the dipole magnets; note that the direction of the field inside one beam pipe is opposite with respect to the other beam pipe which guarantee that both proton beams are curved in the same direction towards the center of the ring. The effect of the dipole magnetic field on the proton beam is represented in the bottom right side [66,69,70].

1000 3.5. The bending effect of the magnetic field on the proton beam is shown in the
 1001 bottom right side of figure 3.5. Note that the dipole magnets are not curved; the arc
 1002 section of the LHC ring is composed of straight dipole magnets of about 15 m. In
 1003 total there are 1232 dipole magnets along the LHC ring.
 1004 In addition to bending the beam trajectory, the beam has to be focused so it stays
 1005 in side the beam pipe. The focusing is performed by quadrupole magnets installed

1006 in another straight section. Other effects like electromagnetic interaction among
 1007 bunches, electron clouds from the beam pipe, gravitational force on the protons,
 1008 differences in energy among protons in the same bunch among others, are corrected
 1009 using sextupole magnets and other magnetic multipoles.

1010 The two proton beams inside the LHC ring are made of bunches with a cylindrical
 1011 shape of ≈ 7.5 cm long and ≈ 1 mm in diameter when they are not close to the
 1012 collision points (IP); close to the IP, the beam is focused up to a diameter of $\approx 16\mu m$
 1013 in order to maximize the expected number of collisions per unit area and per second
 1014 which is known as luminosity(L). Luminosity can be calculated using

$$L = fn \frac{N_1 N_2}{4\pi\sigma_x\sigma_y} \quad (3.2)$$

1015 where f is the revolution frequency, n is the number of bunches per beam, N_1 and N_2
 1016 are the number of protons per bunch, σ_x and σ_y are the gaussian transverse sizes of
 1017 the bunches. Using

$$f = \frac{v}{2\pi r_{LHC}} \approx \frac{3 \times 10^8 m/s}{27 km} \approx 11.1 kHz,$$

$$n = 2808$$

$$N_1 = N_2 = 1.5 \times 10^{11}$$

$$\sigma_x = \sigma_y = 16\mu m$$

1018

$$L = 1.28 \times 10^{34} cm^{-2}s^{-1} \quad (3.3)$$

1019 Luminosity is fundamental aspect for LHC given that the bigger luminosity, the bigger
 1020 number of collisions which means that processes with a very small cross section the
 1021 number of expected occurrences is increased and so the chances of being detected.

1022 The integrated luminosity collected by the CMS experiment during 2016 is shown in
 1023 figure 3.6; the data analized in this thesis corresponds to an integrated luminosity of
 1024 35.9 fb^{-1} at $\sqrt{s} = 13 \text{ TeV}$.

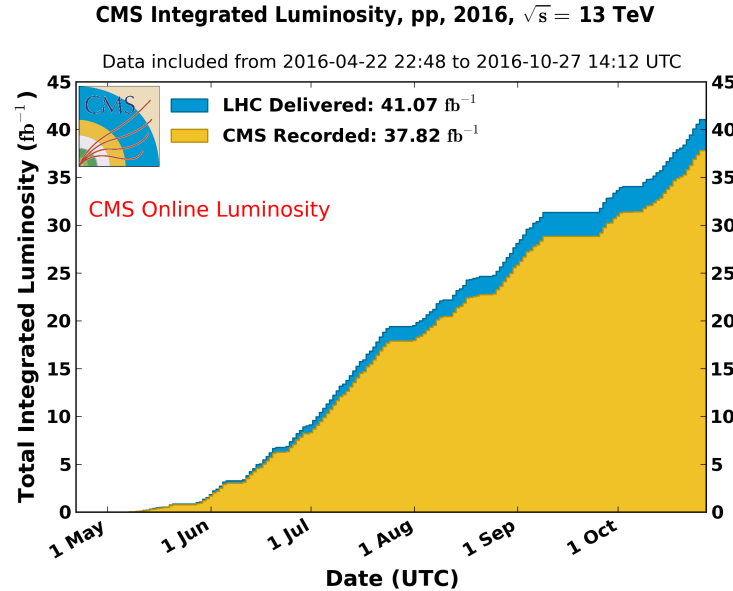


Figure 3.6: Integrated luminosity delivered by LHC and recorded by CMS during 2016. The difference between the delivered and the recorded luminosities is due to fails and issues occurred during the data taking in the CMS experiment [71].

1025 Once the beams reach the desired energy, they are brought to cross each other
 1026 producing proton-proton collisions. The bunch crossing happens in precise places
 1027 where the LHC experiments are located. As seen in Figure ???

1028 The beams intersect at four points where collisions take place. In 2008, the first
 1029 set of collisions involved protons with center-of-mass energy (\sqrt{s}) of 7 TeV; the energy
 1030 was increased to 8 TeV in 2012 and to 13 TeV in 2015.

1031 the CMS (point 5) and ATLAS (point 1) experiments, which are multi-purpose
 1032 experiments, enabled to explore physics in any of the collision modes. LHCb (point 8)
 1033 experiment is optimized to explore B-physics, while ALICE (point 2) is optimized for
 1034 heavy ion collisions researches; TOTEM (point 5) and LHCf (point 1) are dedicated to

1035 forward physics studies and MoEDAL (point 8) is intended for monopoles or massive
1036 pseudo stable particles searches.

1037 **3.3 The CMS experiment**

1038 The Compact Muon Solenoid (CMS) is a general purpose detector designed to conduct
1039 research in a wide range of physics from standard model to new physics like extra
1040 dimensions and dark matter. Located at the point 5 in the LHC layout as shown in
1041 Figure ??, CMS is composed by several detection systems distributed in a cylindrical
1042 structure where the main feature is a solenoid magnet made of superconducting cable
1043 capable to generate a 3.8 T magnetic field. In total, CMS weight about 14000 tons
1044 in a very compact 21.6 m long and 14.6 m diameter cylinder (include areference for
1045 CMS TDR). It was built in 15 separated sections at the ground level and lowered
1046 to the cavern individually to be assembled. Figure 3.7 show the layout of the CMS
1047 detector (CMS TDR).

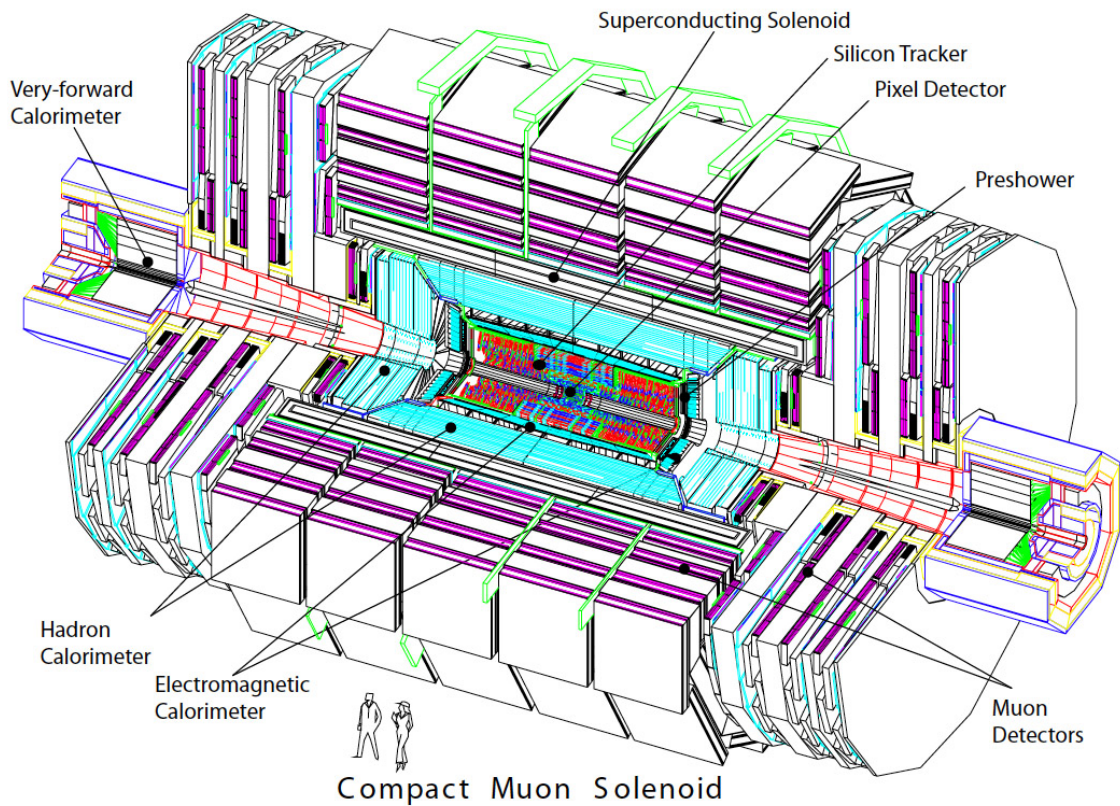


Figure 3.7: ref: CMS Collaboration, “Detector Drawings”, CMS-PHO-GEN-2012-002, <http://cds.cern.ch/record/1433717>, 2012.

1048 **3.3.1 coordinate system**

1049 **3.3.2 tracker- pixels and strips**

1050 **3.3.3 calorimeters**

1051 **3.3.4 magnet**

1052 **3.3.5 muon system**

1053 **3.3.6 trigger system - HLT- L1**

1054 **3.3.7 computing model**

1055 **3.4 Event generation simulation and
1056 reconstruction**

1057 **3.4.1 event generation**

1058 **3.4.2 Hard scattering**

1059 **3.4.3 parton shower**

1060 **3.4.4 hadronization and decays**

1061 **3.4.5 underlying events and pileup**

1062 **3.4.6 MC - MadEvent, MadGraph and madgraphNLO,
1063 powheg, pythia, tauola**

1064 **3.4.7 detector simulation**

1065 **3.4.8 event reconstruction- particle flow algorithm,
1066 vertexing , muon reco, electron reco, photon and**

¹⁰⁷⁵ **Chapter 4**

¹⁰⁷⁶ **Search for production of a Higgs**
¹⁰⁷⁷ **boson and a single top quark in**
¹⁰⁷⁸ **multilepton final states in pp**
¹⁰⁷⁹ **collisions at $\sqrt{s} = 13$ TeV**

¹⁰⁸⁰ **4.1 Introduction**

¹⁰⁸¹ Dont forget to mention previous constrains to ct check reference ?? and references
¹⁰⁸² <https://link.springer.com/content/pdf/10.1007%2FJHEP01>
¹⁰⁸³ A. Azatov, R. Contino and J. Galloway, âIJModel-Independent Bounds on a
¹⁰⁸⁴ Light Higgs,â JHEP 1204 (2012) 127 [arXiv:1202.3415 [hep-ph]].
¹⁰⁸⁵ J. R. Espinosa, C. Grojean, M. Muhlleitner and M. Trott, âIJFingerprinting
¹⁰⁸⁶ Higgs Suspects at the LHC,â JHEP 1205 (2012) 097 [arXiv:1202.3697 [hep-ph]].
¹⁰⁸⁷ This chapter present the search for the associated production of a Higgs boson and
¹⁰⁸⁸ a single top quark events with three leptons in the final state, targeting Higgs decay

1089 modes to WW , ZZ , and $\tau\tau$. The analysis uses the 13 TeV dataset produced in 2016,
 1090 corresponding to an integrated luminosity of 35.9fb^{-1} . It is based on and expands
 1091 previous analyses at 8 TeV [72, 73] and searches for associated production of $t\bar{t}$ and
 1092 Higgs in the same channel [74], and complements searches in other decay channels
 1093 targeting $H \rightarrow b\bar{b}$ [75].

1094 As showed in section 2.4, the cross section of the associated production of a Higgs
 1095 boson and a single top quark (tHq) process is driven by a destructive interference of
 1096 two contributions (see Figure 4.1), where the Higgs couples to either the W boson or
 1097 the top quark. Any deviation from the standard model (SM) in the Higgs coupling
 1098 structure could therefore lead to a large enhancement of the cross section, making
 1099 this analysis sensitive to such deviations. A second process, where the Higgs and
 1100 top quark are accompanied by a W boson (tHW) has similar behavior, albeit with a
 1101 weaker interference pattern.

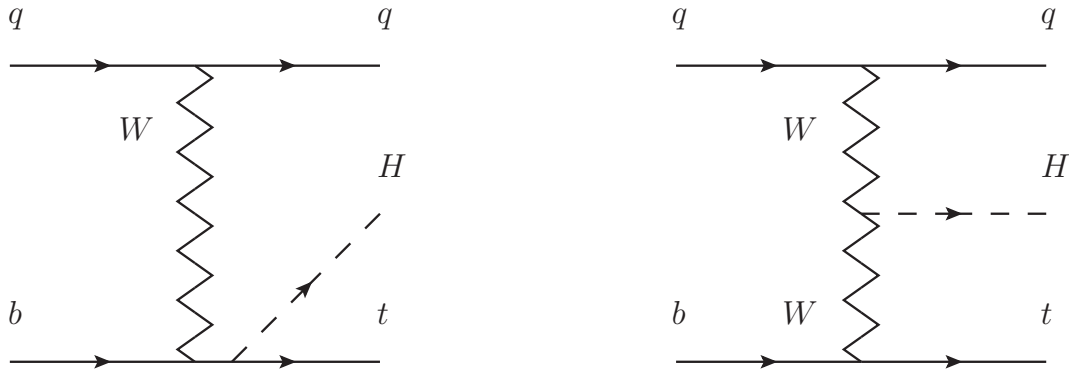


Figure 4.1: The two leading-order diagrams of tHq production.

1102 We selects events with three leptons and a b tagged jet in the final state. The tHq
 1103 signal contribution is then determined in a fit of the observed data to two multivariate
 1104 classifier outputs, each trained to discriminate against one of the two dominant back-
 1105 grounds of events with non-prompt leptons from $t\bar{t}$ and of associated production of $t\bar{t}$

and vector bosons ($t\bar{t}W$, $t\bar{t}Z$). The fit result is then used to set an upper limit on the combined $t\bar{t}H$, tHq and tHW production cross section, as a function of the relative coupling strengths of Higgs and top quark and Higgs and W boson, respectively.

4.2 Data and MC Samples

The data considered in this analysis were collected by the CMS experiment during 2016 and correspond to a total integrated luminosity of 35.9fb^{-1} . Only periods when the CMS magnet was on were considered when selecting the data samples, that corresponds to the 23 Sep 2016 (Run B to G) and PromptReco (Run H) versions of the datasets. The MC samples used in this analysis correspond to the RunIISummer16MiniAODv2 campaign produced with CMSSW 80X. The two signal samples (for tHq and tHW) were produced with MG5_aMC@NLO (version 5.222), in leading-order mode, and are normalized to next-to-leading-order cross sections, see Tab. 4.1. Each sample is generated with a set of event weights corresponding to different values of κ_t and κ_V couplings as shown in Tab. 4.2.

4.2.1 Full 2016 dataset and MC samples

Sample	σ [pb]	BF
/THQ_Hincl_13TeV-madgraph-pythia8_TuneCUETP8M1/	0.7927	0.324
/THW_Hincl_13TeV-madgraph-pythia8_TuneCUETP8M1/	0.1472	1.0

Table 4.1: Signal samples and their cross section and branching fraction used in this analysis. See Ref. [76] for more details.

Different MC generators were used to generate the background processes. The dominant sources ($t\bar{t}$, $t\bar{t}W$, $t\bar{t}Z$, $t\bar{t}H$) were produced using AMC@NLO interfaced to PYTHIA8, and are scaled to NLO cross sections. Other processes are simulated

		<i>tHq</i>			<i>tHW</i>		
κ_V	κ_t	sum of weights	cross section [pb]	sum of weights	cross section [pb]	LHE weights	
1.0	-3.0	35.700022	2.991	11.030445	0.6409	LHEweight_wgt[446]	
1.0	-2.0	20.124298	1.706	5.967205	0.3458	LHEweight_wgt[447]	
1.0	-1.5	14.043198	1.205	4.029093	0.2353	LHEweight_wgt[448]	
1.0	-1.25	11.429338	0.9869	3.208415	0.1876	LHEweight_wgt[449]	
1.0	-1.0		0.7927		0.1472		
1.0	-0.75	7.054998	0.6212	1.863811	0.1102	LHEweight_wgt[450]	
1.0	-0.5	5.294518	0.4723	1.339886	0.07979	LHEweight_wgt[451]	
1.0	-0.25	3.818499	0.3505	0.914880	0.05518	LHEweight_wgt[452]	
1.0	0.0	2.627360	0.2482	0.588902	0.03881	LHEweight_wgt[453]	
1.0	0.25	1.719841	0.1694	0.361621	0.02226	LHEweight_wgt[454]	
1.0	0.5	1.097202	0.1133	0.233368	0.01444	LHEweight_wgt[455]	
1.0	0.75	0.759024	0.08059	0.204034	0.01222	LHEweight_wgt[456]	
1.0	1.0	0.705305	0.07096	0.273617	0.01561	LHEweight_wgt[457]	
1.0	1.25	0.936047	0.0839	0.442119	0.02481	LHEweight_wgt[458]	
1.0	1.5	1.451249	0.1199	0.709538	0.03935	LHEweight_wgt[459]	
1.0	2.0	3.335034	0.2602	1.541132	0.08605	LHEweight_wgt[460]	
1.0	3.0	10.516125	0.8210	4.391335	0.2465	LHEweight_wgt[461]	
<hr/>							
1.5	-3.0	45.281492	3.845	13.426212	0.7825	LHEweight_wgt[462]	
1.5	-2.0	27.606715	2.371	7.809713	0.4574	LHEweight_wgt[463]	
1.5	-1.5	20.476088	1.784	5.594971	0.3290	LHEweight_wgt[464]	
1.5	-1.25	17.337465	1.518	4.635978	0.2749	LHEweight_wgt[465]	
1.5	-1.0	14.483302	1.287	3.775902	0.2244	LHEweight_wgt[466]	
1.5	-0.75	11.913599	1.067	3.014744	0.1799	LHEweight_wgt[467]	
1.5	-0.5	9.628357	0.874	2.352505	0.1410	LHEweight_wgt[468]	
1.5	-0.25	7.627574	0.702	1.789184	0.1081	LHEweight_wgt[469]	
1.5	0.0	5.911882	0.5577	1.324946	0.08056	LHEweight_wgt[470]	
1.5	0.25	4.479390	0.4365	0.959295	0.05893	LHEweight_wgt[471]	
1.5	0.5	3.331988	0.3343	0.692727	0.04277	LHEweight_wgt[472]	
1.5	0.75	2.469046	0.2558	0.525078	0.03263	LHEweight_wgt[473]	
1.5	1.0	1.890565	0.2003	0.456347	0.02768	LHEweight_wgt[474]	
1.5	1.25	1.596544	0.1689	0.486534	0.02864	LHEweight_wgt[475]	
1.5	1.5	1.586983	0.1594	0.615638	0.03509	LHEweight_wgt[476]	
1.5	2.0	2.421241	0.2105	1.170602	0.06515	LHEweight_wgt[477]	
1.5	3.0	7.503280	0.5889	3.467546	0.1930	LHEweight_wgt[478]	
<hr/>							
0.5	-3.0	27.432685	2.260	8.929074	0.5136	LHEweight_wgt[479]	
0.5	-2.0	13.956013	1.160	4.419093	0.2547	LHEweight_wgt[480]	
0.5	-1.5	8.924438	0.7478	2.757611	0.1591	LHEweight_wgt[481]	
0.5	-1.25	6.835341	0.5726	2.075247	0.1204	LHEweight_wgt[482]	
0.5	-1.0	5.030704	0.4273	1.491801	0.08696	LHEweight_wgt[483]	
0.5	-0.75	3.510528	0.2999	1.007273	0.05885	LHEweight_wgt[484]	
0.5	-0.5	2.274811	0.1982	0.621663	0.03658	LHEweight_wgt[485]	
0.5	-0.25	1.323555	0.1189	0.334972	0.01996	LHEweight_wgt[486]	
0.5	0.0	0.656969	0.06223	0.147253	0.008986	LHEweight_wgt[487]	
0.5	0.25	0.274423	0.02830	0.058342	0.003608	LHEweight_wgt[488]	
0.5	0.5	0.176548	0.01778	0.068404	0.003902	LHEweight_wgt[489]	
0.5	0.75	0.363132	0.03008	0.177385	0.009854	LHEweight_wgt[490]	
0.5	1.0	0.834177	0.06550	0.385283	0.02145	LHEweight_wgt[491]	
0.5	1.25	1.589682	0.1241	0.692099	0.03848	LHEweight_wgt[492]	
0.5	1.5	2.629647	0.2047	1.097834	0.06136	LHEweight_wgt[493]	
0.5	2.0	5.562958	0.4358	2.206057	0.1246	LHEweight_wgt[494]	
0.5	3.0	14.843102	1.177	5.609519	0.3172	LHEweight_wgt[495]	

Table 4.2: κ_V and κ_t combinations generated for the two signal samples and their NLO cross sections. The tHq cross section is multiplied by the branching fraction of the enforced leptonic decay of the top quark (0.324). See also Ref. [76].

Sample	σ [pb]
TTWJetsToLNu_TuneCUETP8M1_13TeV-amcatnloFXFX-madspin-pythia8	0.2043
TTZToLLNuNu_M-10_TuneCUETP8M1_13TeV-amcatnlo-pythia8	0.2529
ttHJetToNonbb_M125_13TeV_amcatnloFXFX_madspin_pythia8_mWCutfix /store/cmst3/group/susy/gpetrucc/13TeV/u/TTLL_m1to10_LO_NoMS_for76X/	0.2151 0.0283
WGToLNug_TuneCUETP8M1_13TeV-madgraphMLM-pythia8	585.8
ZGTo2LG_TuneCUETP8M1_13TeV-amcatnloFXFX-pythia8	131.3
TGJets_TuneCUETP8M1_13TeV_amcatnlo_madspin_pythia8	2.967
TGJets_TuneCUETP8M1_13TeV_amcatnlo_madspin_pythia8	2.967
TTGJets_TuneCUETP8M1_13TeV-amcatnloFXFX-madspin-pythia8	3.697
WpWpJJ_EWK-QCD_TuneCUETP8M1_13TeV-madgraph-pythia8	0.03711
ZZZ_TuneCUETP8M1_13TeV-amcatnlo-pythia8	0.01398
WWZ_TuneCUETP8M1_13TeV-amcatnlo-pythia8	0.1651
WZZ_TuneCUETP8M1_13TeV-amcatnlo-pythia8	0.05565
WW_DoubleScattering_13TeV-pythia8	1.64
tZq_1l_4f_13TeV-amcatnlo-pythia8_TuneCUETP8M1	0.0758
ST_tW1l_5f_L0_13TeV-MadGraph-pythia8	0.01123
TTTT_TuneCUETP8M1_13TeV-amcatnlo-pythia8	0.009103
WZTo3LNu_TuneCUETP8M1_13TeV-powheg-pythia8	4.4296
ZZTo4L_13TeV_powheg_pythia8	1.256
TTJets_SingleLeptFromTbar_TuneCUETP8M1_13TeV-madgraphMLM-pythia8	182.1754
TTJets_SingleLeptFromT_TuneCUETP8M1_13TeV-madgraphMLM-pythia8	182.1754
TTJets_DiLept_TuneCUETP8M1_13TeV-madgraphMLM-pythia8	87.3
DYJetsToLL_M-10to50_TuneCUETP8M1_13TeV-amcatnloFXFX-pythia8	18610
DYJetsToLL_M-50_TuneCUETP8M1_13TeV-madgraphMLM-pythia8	6024
WJetsToLNu_TuneCUETP8M1_13TeV-amcatnloFXFX-pythia8	61526.7
ST_tW_top_5f_inclusiveDecays_13TeV-powheg-pythia8_TuneCUETP8M1	35.6
ST_tW_antitop_5f_inclusiveDecays_13TeV-powheg-pythia8_TuneCUETP8M1	35.6
ST_t-channel_4f_leptonDecays_13TeV-amcatnlo-pythia8_TuneCUETP8M1	70.3144
ST_t-channel_antitop_4f_leptonDecays_13TeV-powheg-pythia8_TuneCUETP8M1	26.2278
ST_s-channel_4f_leptonDecays_13TeV-amcatnlo-pythia8_TuneCUETP8M1	3.68064
WWTo2L2Nu_13TeV-powheg	10.481

Table 4.3: List of background samples used in this analysis (CMSSW 80X). In the first section of the table are listed the samples of the processes for which we use the simulation to extract the final yields and shapes, in the second section the samples of the processes we will estimate from data. The MC simulation is used to design the data driven methods and derive the associated systematics.

Sample	σ [pb]
ttWJets_13TeV_madgraphMLM	0.6105
ttZJets_13TeV_madgraphMLM	0.5297/0.692

Table 4.4: Leading-order $t\bar{t}W$ and $t\bar{t}Z$ samples used in the signal BDT training.

1124 using POWHEG interfaced to PYTHIA, or bare PYTHIA (see table 4.3 and [74]
1125 for more details).

Three lepton and Four lepton
HLT_DiMu9_Ele9_CaloIdL_TrackIdL_v*
HLT_Mu8_DiEle12_CaloIdL_TrackIdL_v*
HLT_TripleMu_12_10_5_v*
HLT_Ele16_Ele12_Ele8_CaloIdL_TrackIdL_v*
HLT_Mu23_TrkIsoVVL_Ele8_CaloIdL_TrackIdL_IsoVL_v*
HLT_Mu23_TrkIsoVVL_Ele8_CaloIdL_TrackIdL_IsoVL_DZ_v*
HLT_Mu8_TrkIsoVVL_Ele23_CaloIdL_TrackIdL_IsoVL_v*
HLT_Mu8_TrkIsoVVL_Ele23_CaloIdL_TrackIdL_IsoVL_DZ_v*
HLT_Ele23_Ele12_CaloIdL_TrackIdL_IsoVL_DZ_v*
HLT_Mu17_TrkIsoVVL_Mu8_TrkIsoVVL_DZ_v*
HLT_Mu17_TrkIsoVVL_TkMu8_TrkIsoVVL_DZ_v*
HLT_IsoMu22_v*
HLT_IsoTkMu22_v*
HLT_IsoMu22_eta2p1_v*
HLT_IsoTkMu22_eta2p1_v*
HLT_IsoMu24_v*
HLT_IsoTkMu24_v*
HLT_Ele27_WPTight_Gsf_v*
HLT_Ele25_eta2p1_WPTight_Gsf_v*
HLT_Ele27_eta2p1_WPLoose_Gsf_v*

Table 4.5: Table of high-level triggers that we consider in the analysis.

1126 4.2.2 Triggers

1127 We consider online-reconstructed events triggered by one, two, or three leptons.
 1128 Single-lepton triggers are included to boost the acceptance of events where the p_T of
 1129 the sub-leading lepton falls below the threshold of the double-lepton triggers. Ad-
 1130 ditionally, by including double-lepton triggers in the ≥ 3 lepton category, as well
 1131 as single-lepton triggers in all categories, we increase the efficiency, considering the
 1132 logical “or” of the trigger decisions of all the individual triggers in a given category.
 1133 Tab. 4.5 shows the lowest-threshold non-prescaled triggers present in the High-Level
 1134 Trigger (HLT) menus for both Monte-Carlo and data in 2016.

1135 4.2.2.1 Trigger efficiency scale factors

1136 The efficiency of events to pass the trigger is measured in simulation (trivially using
 1137 generator information) and in the data (using event collected by an uncorrelated

Category	Scale Factor
ee	1.01 ± 0.02
e μ	1.01 ± 0.01
$\mu\mu$	1.00 ± 0.01
3l	1.00 ± 0.03

Table 4.6: Trigger efficiency scale factors and associated uncertainties, shown here rounded to the nearest percent.

1138 MET trigger). Small differences between the data and MC efficiencies are corrected
 1139 by applying scale factors as shown in Tab. 4.6. The exact procedure and control plots
 1140 are documented in [77] for the current analysis.

1141 4.3 Object Identification and event selection

1142 4.3.1 Jets and b tagging

1143 The analysis uses anti- k_t (0.4) particle-flow (PF) jets, corrected for charged hadrons
 1144 not coming from the primary vertex (charged hadron subtraction), and having jet
 1145 energy corrections (`Summer16_23Sep2016V3`) applied as a function of the jet E_T and
 1146 η . Jets are only considered if they have a transverse energy above 25GeV.

1147 In addition, they are required to be separated from any lepton candidates passing
 1148 the fakeable object selections (see Tables 4.7 and 4.8) by $\Delta R > 0.4$.

1149 The loose and medium working points of the CSV b-tagging algorithm are used to
 1150 identify b jets. Data/simulation differences in the b tagging performance are corrected
 1151 by applying per-jet weights to the simulation, dependent on the jet p_T , eta, b tagging
 1152 discriminator, and flavor (from simulation truth) [78]. The per-event weight is taken
 1153 as the product of the per-jet weights, including those of the jets associated to the
 1154 leptons. More details can be found in the corresponding $t\bar{t}H$ documentation [74, 77].

1155 **4.3.2 Lepton selection**

Cut	Loose	Fakeable object	Tight
$ \eta < 2.4$	✓	✓	✓
p_T	$> 5\text{GeV}$	$> 15\text{GeV}$	$> 15\text{GeV}$
$ d_{xy} < 0.05 \text{ (cm)}$	✓	✓	✓
$ d_z < 0.1 \text{ (cm)}$	✓	✓	✓
$\text{SIP}_{3D} < 8$	✓	✓	✓
$I_{\text{mini}} < 0.4$	✓	✓	✓
is Loose Muon	✓	✓	✓
jet CSV	—	< 0.8484	< 0.8484
is Medium Muon	—	—	✓
tight-charge	—	—	✓
lepMVA > 0.90	—	—	✓

Table 4.7: Requirements on each of the three muon selections. In the cases where the cut values change between the selections, those values are listed in the table. Otherwise, whether the cut is applied is indicated. For the two p_T^{ratio} and CSV rows, the cuts marked with a † are applied to leptons that fail the lepton MVA cut, while the loose cut value is applied to those that pass the lepton MVA cut.

1156 The lepton reconstruction and selection is identical to that used in the $t\bar{t}H$ mul-
 1157 tilepton analysis, as documented in Refs. [74, 77]. For details on the reconstruction
 1158 algorithms, isolation, pileup mitigation, and a description of the lepton MVA discrim-
 1159 inator and validation plots thereof, we refer to that document since they are out of
 1160 the scope of this thesis. Three different selections are defined both for the electron
 1161 and muon object identification: the *Loose*, *Fakeable Object*, and *Tight* selection. As
 1162 described in more detail later, these are used for event level vetoes, the fake rate
 1163 estimation application region, and the final signal selection, respectively. The p_T of
 1164 fakeable objects is defined as $0.85 \times p_T(\text{jet})$, where the jet is the one associated to the
 1165 lepton object. This mitigates the dependence of the fake rate on the momentum of
 1166 the fakeable object and thereby improves the precision of the method.

1167 Tables 4.7 and 4.8 list the full criteria for the different selections of muons and
 1168 electrons.

Cut	Loose	Fakeable Object	Tight
$ \eta < 2.5$	✓	✓	✓
p_T	$> 7\text{GeV}$	$> 15\text{GeV}$	$> 15\text{GeV}$
$ d_{xy} < 0.05 \text{ (cm)}$	✓	✓	✓
$ d_z < 0.1 \text{ (cm)}$	✓	✓	✓
$\text{SIP}_{3D} < 8$	✓	✓	✓
$I_{\text{mini}} < 0.4$	✓	✓	✓
MVA ID $> (0.0, 0.0, 0.7)$	✓	✓	✓
$\sigma_{i\eta i\eta} < (0.011, 0.011, 0.030)$	—	✓	✓
$\text{H/E} < (0.10, 0.10, 0.07)$	—	✓	✓
$\Delta\eta_{in} < (0.01, 0.01, 0.008)$	—	✓	✓
$\Delta\phi_{in} < (0.04, 0.04, 0.07)$	—	✓	✓
$-0.05 < 1/E - 1/p < (0.010, 0.010, 0.005)$	—	✓	✓
p_T^{ratio}	—	$> 0.5 \dagger / -$	—
jet CSV	—	$< 0.3 \dagger / < 0.8484$	< 0.8484
tight-charge	—	—	✓
conversion rejection	—	—	✓
Number of missing hits	< 2	$== 0$	$== 0$
lepMVA > 0.90	—	—	✓

Table 4.8: Criteria for each of the three electron selections. In cases where the cut values change between selections, those values are listed in the table. Otherwise, whether the cut is applied is indicated. In some cases, the cut values change for different η ranges. These ranges are $0 < |\eta| < 0.8$, $0.8 < |\eta| < 1.479$, and $1.479 < |\eta| < 2.5$ and the respective cut values are given in the form (value₁, value₂, value₃).

1169 4.3.3 Lepton selection efficiency

1170 Efficiencies of reconstruction and selecting loose leptons are measured both for muons
 1171 and electrons using a tag and probe method on both data and MC, using $Z \rightarrow \ell^+\ell^-$.
 1172 Corresponding scale factors are derived from the ratio of efficiencies and applied to the
 1173 selected These. Events are produced for the leptonic SUSY analyses using equivalent
 1174 lepton selections and recycled for the $t\bar{t}H$ analysis as well as for this analysis. The
 1175 efficiencies of applying the tight selection as defined in Tables 4.7 and 4.8, on the
 1176 loose leptons are determined again by using a tag and probe method on a sample of
 1177 DY-enriched events. They are documented for the $t\bar{t}H$ analysis in Ref. [77] and are
 1178 exactly equivalent for this analysis.

1179 4.4 Background predictions

1180 The modeling of reducible and irreducible backgrounds in this analysis uses the exact
 1181 methods, analysis code, and ROOT trees used for the $t\bar{t}H$ multilepton analysis. We
 1182 give a brief description of the methods and refer to the documentation of that analysis
 1183 in Refs. [74, 77] for any details.

1184 The backgrounds in three-lepton final states can be split in two broad categories:
 1185 irreducible backgrounds with genuine prompt leptons (i.e. from on-shell W and Z
 1186 boson decays); and reducible backgrounds where at least one of the leptons is “non-
 1187 prompt”, i.e. produced within a hadronic jet, either a genuine lepton from heavy
 1188 flavor decays, or simply mis-reconstructed jets.

1189 Irreducible backgrounds can be reliably estimated directly from Monte-Carlo sim-
 1190 ulated events, using higher-order cross sections or data control regions for the overall
 1191 normalization. This is done in this analysis for all backgrounds involving prompt lep-
 1192 tons: $t\bar{t}W$, $t\bar{t}Z$, $t\bar{t}H$, WZ , ZZ , $W^\pm W^\pm qq$, $t\bar{t}t\bar{t}$, tZq , tZW , WWW , WWZ , WZZ ,
 1193 ZZZ .

1194 Reducible backgrounds, on the other hand, are not well predicted by simulation,
 1195 and are estimated using data-driven methods. In the case of non-prompt leptons, a
 1196 fake rate method is used, where the contribution to the final selection is estimated by
 1197 extrapolating from a sideband (or “application region”) with a looser lepton definition
 1198 (the fakeable object definitions in Tabs. 4.7 and 4.8) to the signal selection. The tight-
 1199 to-loose ratios (or “fake rates”) are measured in several background dominated data
 1200 events with dedicated triggers, subtracting the residual prompt lepton contribution
 1201 using MC. Non-prompt leptons in our signal regions are predominantly produced in $t\bar{t}$
 1202 events, with a much smaller contribution, from Drell–Yan production. The systematic
 1203 uncertainty on the normalization of the non-prompt background estimation is on the

1204 order of 50%, and thereby one of the dominant limitations on the performance of
 1205 multilepton analyses in general and this analysis in particular. It consists of several
 1206 individual sources, such as the result of closure tests of the method using simulated
 1207 events, limited statistics in the data control regions due to necessary prescaling of
 1208 lepton triggers, and the uncertainty in the subtraction of residual prompt leptons
 1209 from the control region.

1210 The fake background where the leptons pass the looser selection are weighted
 1211 according to how many of them fail the tight criteria. Events with a single failing
 1212 lepton are weighted with the factor $f/(1-f)$ for the estimate to the tight selection
 1213 region, where f is the fake rate. Events with two failing leptons are given the negative
 1214 weight $-f_i f_j / (1-f_i)(1-f_j)$, and for three leptons the weight is positive and equal
 1215 to the product of $f/(1-f)$ factor evaluated for each failing lepton.

1216 Figures 4.2 show the distributions of some relevant kinematic variables, normalized
 1217 to the cross section of the respective processes and to the integrated luminosity.

1218 4.5 Signal discrimination

1219 The tHq signal is separated from the main backgrounds using a boosted decision
 1220 tree (BDT) classifier, trained on simulated signal and background events. A set of
 1221 discriminating variables are given as input to the BDT which produces a output
 1222 distribution maximizing the discrimination power. Table 4.9 lists the input variables
 1223 used while Figures 4.3 show their distributions for the relevant signal and background
 1224 samples, for the three lepton channel. Two BDT classifiers are trained for the two
 1225 main backgrounds expected in the analysis: events with prompt leptons from $t\bar{t}W$ and
 1226 $t\bar{t}Z$ (also referred to as $t\bar{t}V$), and events with non-prompt leptons from $t\bar{t}$. The datasets
 1227 used in the training are the tHq signal (see Tab. 4.1), and LO MADGRAPH samples

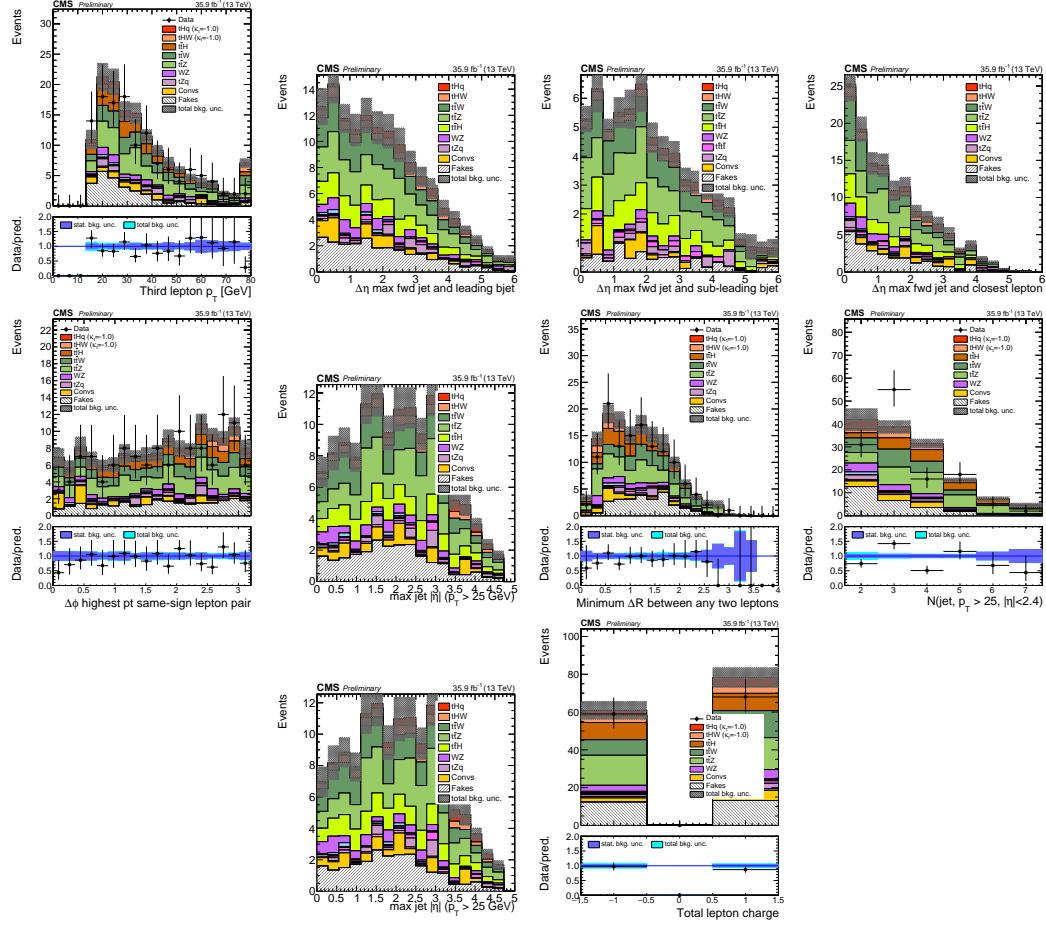


Figure 4.2: Distributions of input variables to the BDT for signal discrimination, three lepton channel, normalized to their cross section and to 35.9fb^{-1} .

of $t\bar{t}W$ and $t\bar{t}Z$, in an admixture proportional to their respective cross sections (see Tab. 4.4).

The MVA analysis consist of two stages: first a “training” where the MVA method is trained to discriminate between simulated signal and background events, then a “test” stage where the trained algorithm is used to classify different events from the samples. The sample is obtained from a pre-selection (see Tab. ?? with pre-selection cuts). Figures 4.4 show the input variables distributions as seen by the MVA algorithm. Note that in contrast to the distributions in Fig. 4.3 only the main backgrounds ($t\bar{t}$ from simulation, $t\bar{t}V$) are included.

Variable name	Description
nJet25	Number of jets with $p_T > 25$ GeV, $ \eta < 2.4$
MaxEtaJet25	Maximum $ \eta $ of any (non-CSV-loose) jet with $p_T > 25$ GeV
totCharge	Sum of lepton charges
nJetEta1	Number of jets with $ \eta > 1.0$, non-CSV-loose
detaFwdJetBJet	$\Delta\eta$ between forward light jet and hardest CSV loose jet
detaFwdJet2BJet	$\Delta\eta$ between forward light jet and second hardest CSV loose jet (defaults to -1 in events with only one CSV loose jet)
detaFwdJetClosestLep	$\Delta\eta$ between forward light jet and closest lepton
dphiHighestPtSSPair	$\Delta\phi$ of highest p_T same-sign lepton pair
minDRll	minimum ΔR between any two leptons
Lep3Pt/Lep2Pt	p_T of the 3 rd lepton (2 nd for ss2l)

Table 4.9: MVA input discriminating variables

1237 Note that splitting the training in two groups reveals that some variables show
 1238 opposite behavior for the two background sources; potentially screening the discrimi-
 1239 nation power if they were to be used in a single discriminant. For some other variables
 1240 the distributions are similar in both background cases.

1241 From table 4.9, it is clear that the input variables are correlated to some extend.
 1242 These correlations play an important role for some MVA methods like the Fisher
 1243 discriminant method in which the first step consist of performing a linear transfor-
 1244 mation to an phase space where the correlations between variables are removed. In
 1245 case a boosted decision tree (BDT) method however, correlations do not affect the
 1246 performance. Figure 4.6 show the linear correlation coefficients for signal and back-
 1247 ground for the two training cases (the signal values are identical by construction). As
 1248 expected, strong correlations appears for variables related to the forward jet activity.
 1249 Same trend is seen in case of the same sign dilepton channel in Figure ??.

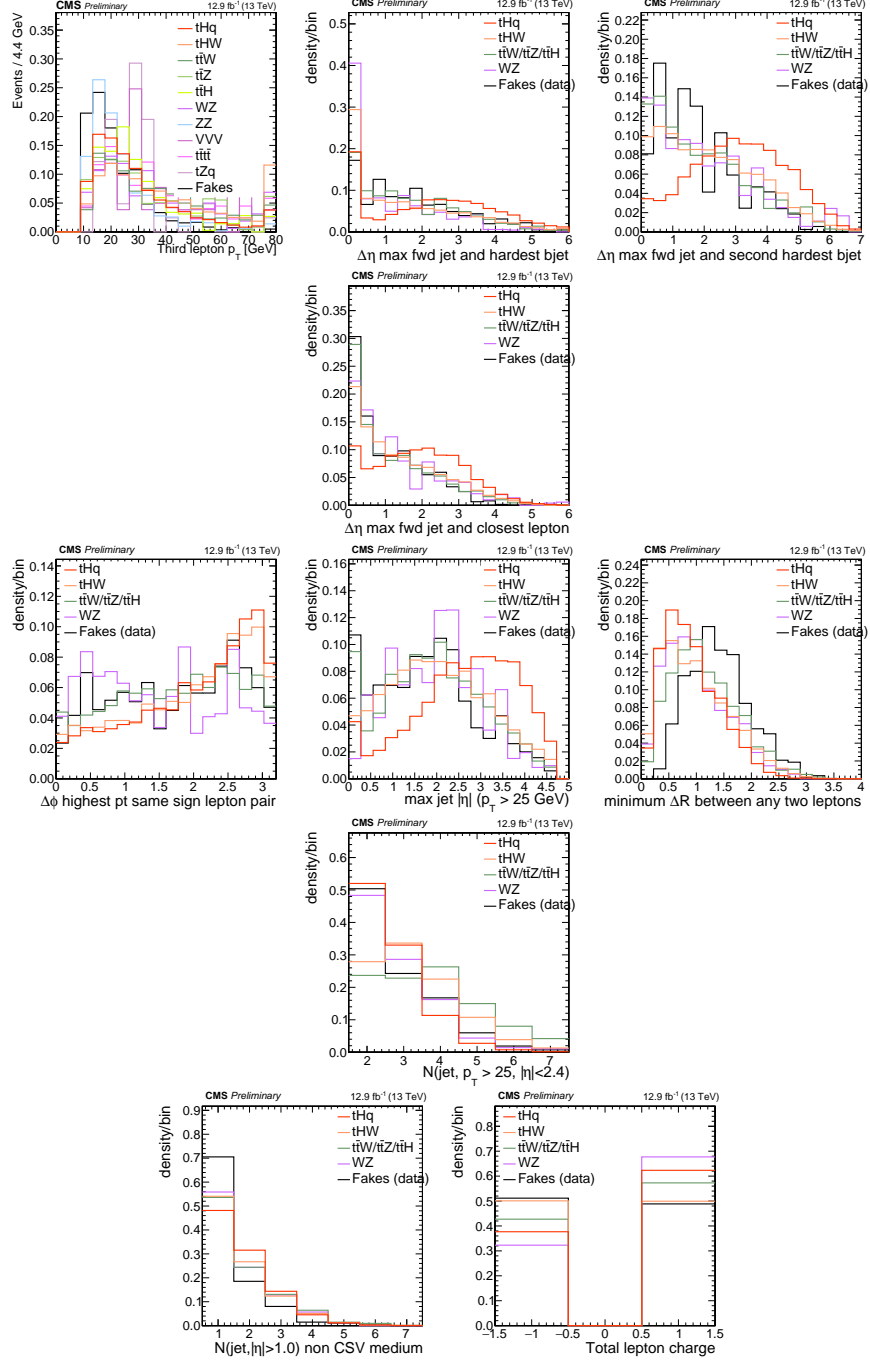


Figure 4.3: Distributions of input variables to the BDT for signal discrimination, three lepton channel.

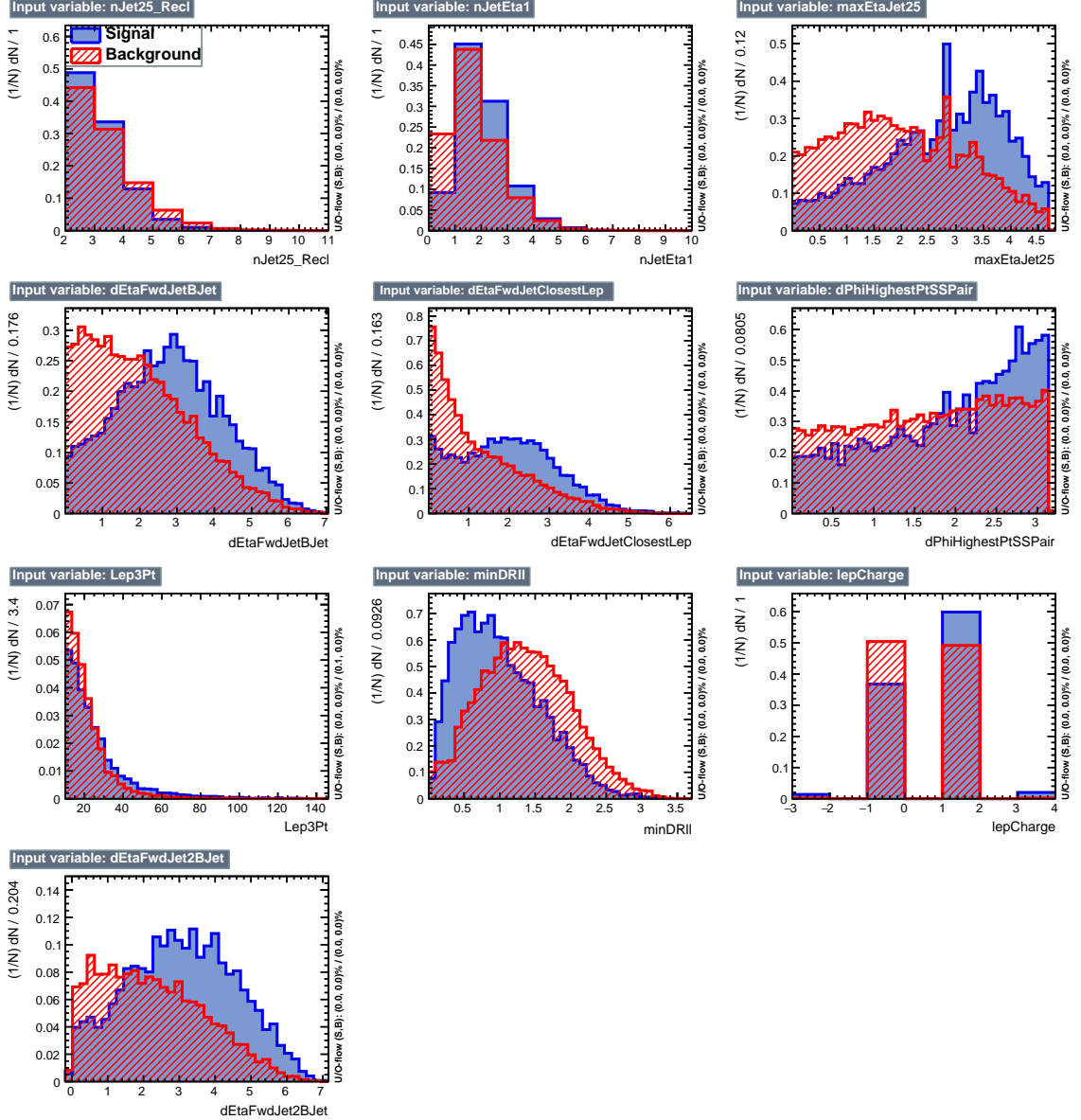


Figure 4.4: BDT inputs as seen by TMVA (signal, in blue, is tHq , background, in red, is $t\bar{t}$) for the three lepton channel, discriminated against $t\bar{t}$ (fakes) background.

1250 4.5.1 Classifiers response

1251 Several MVA algorithms were evaluated to determine the most appropriate method
 1252 for this analysis. The plots in Fig. 4.7 (top) show the background rejection as a
 1253 function of the signal efficiency for $t\bar{t}$ and $t\bar{t}V$ trainings (ROC curves) for the different

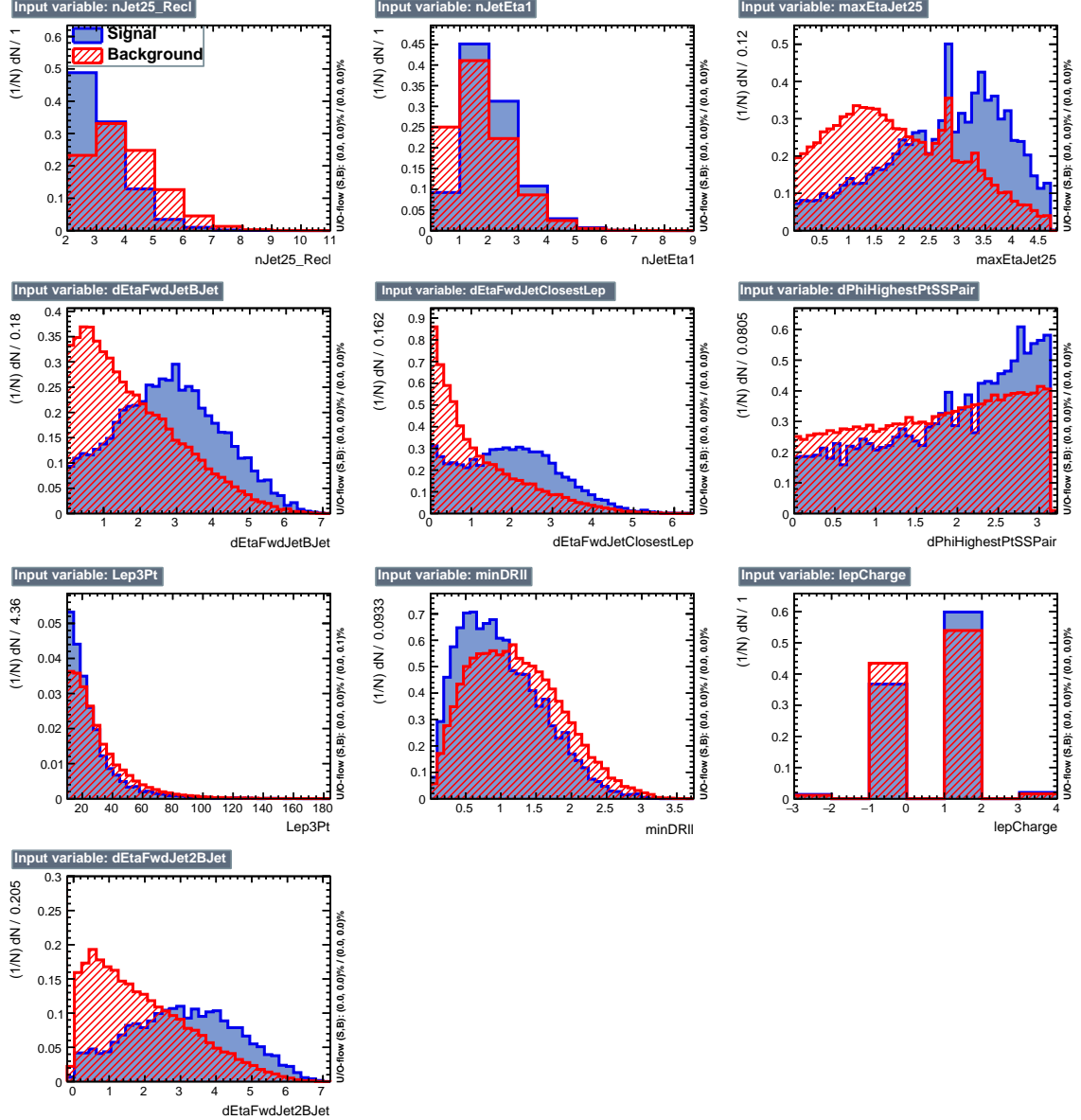


Figure 4.5: BDT inputs as seen by TMVA (signal, in blue, is tHq , background, in red, is $t\bar{t}W+t\bar{t}Z$) for the three lepton channel, discriminated against $t\bar{t}V$ background.

algorithms that were evaluated.

In both cases the gradient boosted decision tree (“BDTA_GRAD”) classifier offers the best results, followed by an adaptive BDT classifier (“BDTA”). The BDTA_GRAD classifier output distributions for signal and backgrounds are shown on the bottom of Fig. 4.7. As expected, a good discrimination power is obtained using default discrim-

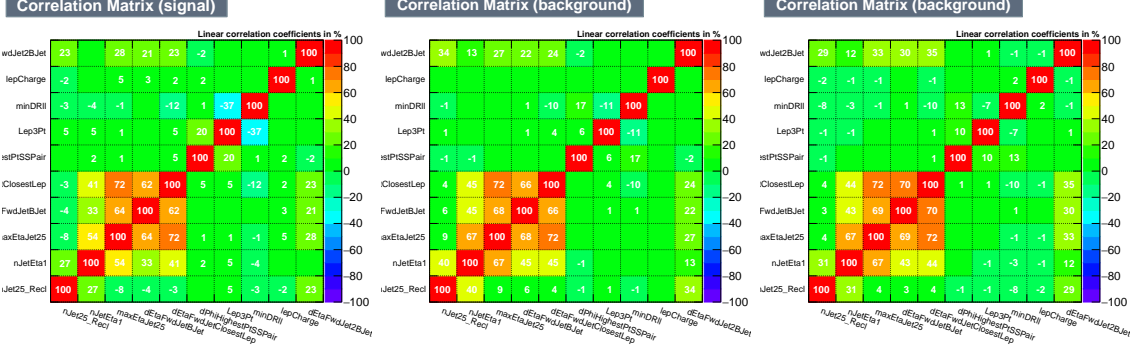


Figure 4.6: Signal (left), $t\bar{t}$ background (middle), and $t\bar{t}V$ background (right.) correlation matrices for the input variables in the TMVA analysis for the three lepton channel.

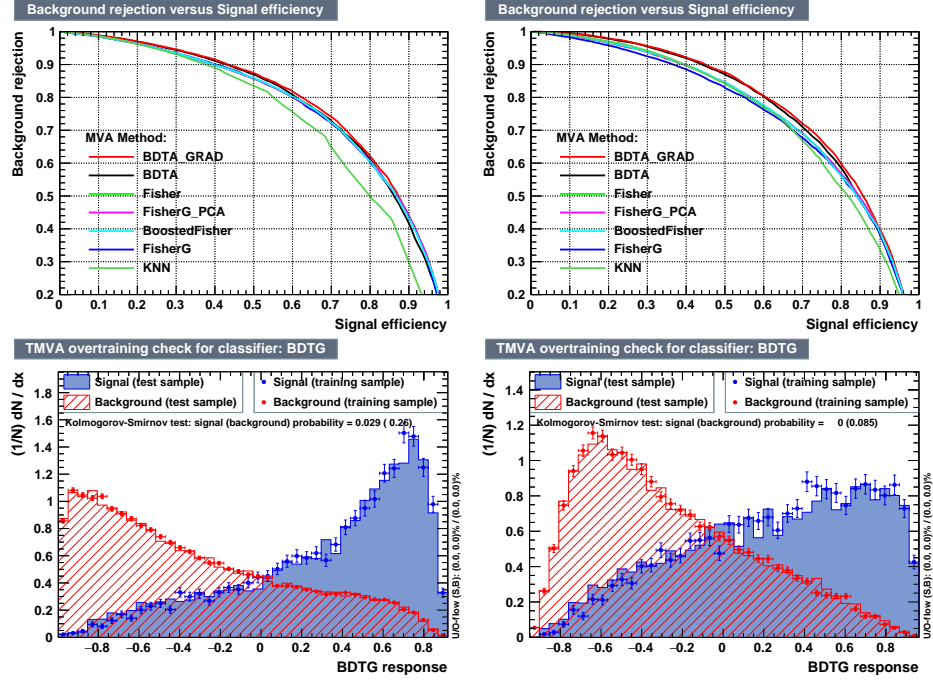


Figure 4.7: Top: background rejection vs signal efficiency (ROC curves) for various MVA classifiers (top) in the three lepton channel against $t\bar{t}V$ (left) and $t\bar{t}$ (right). Bottom: classifier output distributions for the gradient boosted decision trees, for training against $t\bar{t}V$ (left) and against $t\bar{t}$ (right).

1259 inator parameter values, with minimal overtraining. TMVA provides a ranking of the
 1260 input variables by their importance in the classification process, shown in Tab. 4.10.
 1261 The TMVA settings used in the BDT training are shown in Tab. 4.11.

ttbar training			ttV training		
Rank	Variable	Importance	Variable	Importance	Importance
1	minDRll	1.329e-01	dEtaFwdJetBJet	1.264e-01	
2	dEtaFwdJetClosestLep	1.294e-01	Lep3Pt	1.224e-01	
3	dEtaFwdJetBJet	1.209e-01	maxEtaJet25	1.221e-01	
4	dPhiHighestPtSSPair	1.192e-01	dEtaFwdJet2BJet	1.204e-01	
5	Lep3Pt	1.158e-01	dEtaFwdJetClosestLep	1.177e-01	
6	maxEtaJet25	1.121e-01	minDRll	1.143e-01	
7	dEtaFwdJet2BJet	9.363e-02	dPhiHighestPtSSPair	9.777e-02	
8	nJetEta1	6.730e-02	nJet25_Recl	9.034e-02	
9	nJet25_Recl	6.178e-02	nJetEta1	4.749e-02	
10	lepCharge	4.701e-02	lepCharge	4.116e-02	

Table 4.10: TMVA input variables ranking for BDTA_GRAD method for the trainings in the three lepton channel. For both trainings the rankings show almost the same 5 variables in the first places.

```
TMVA.Types.kBDT
NTrees=800
BoostType=Grad
Shrinkage=0.10
!UseBaggedGrad
nCuts=50
MaxDepth=3
NegWeightTreatment=PairNegWeightsGlobal
CreateMVApdfs
```

Table 4.11: TMVA configuration used in the BDT training.

1262 4.6 Additional discriminating variables

1263 Two additional discriminating variables were tested considering the fact that the
 1264 forward jet in the background could come from the pileup; since we have a real
 1265 forward jet in the signal, it could give some improvement in the discriminating power.
 1266 The additional variables describe the forward jet momentum (fwdJetPt25) and the
 1267 forward jet identification(fwdJetPUID). Distributions for these variables in the three
 1268 lepton channel are shown in the figure 4.8. The forward jet identification distribution
 1269 show that for both, signal and background, jets are mostly real jets.

1270 The testing was made including in the MVA input one variable at a time, so we

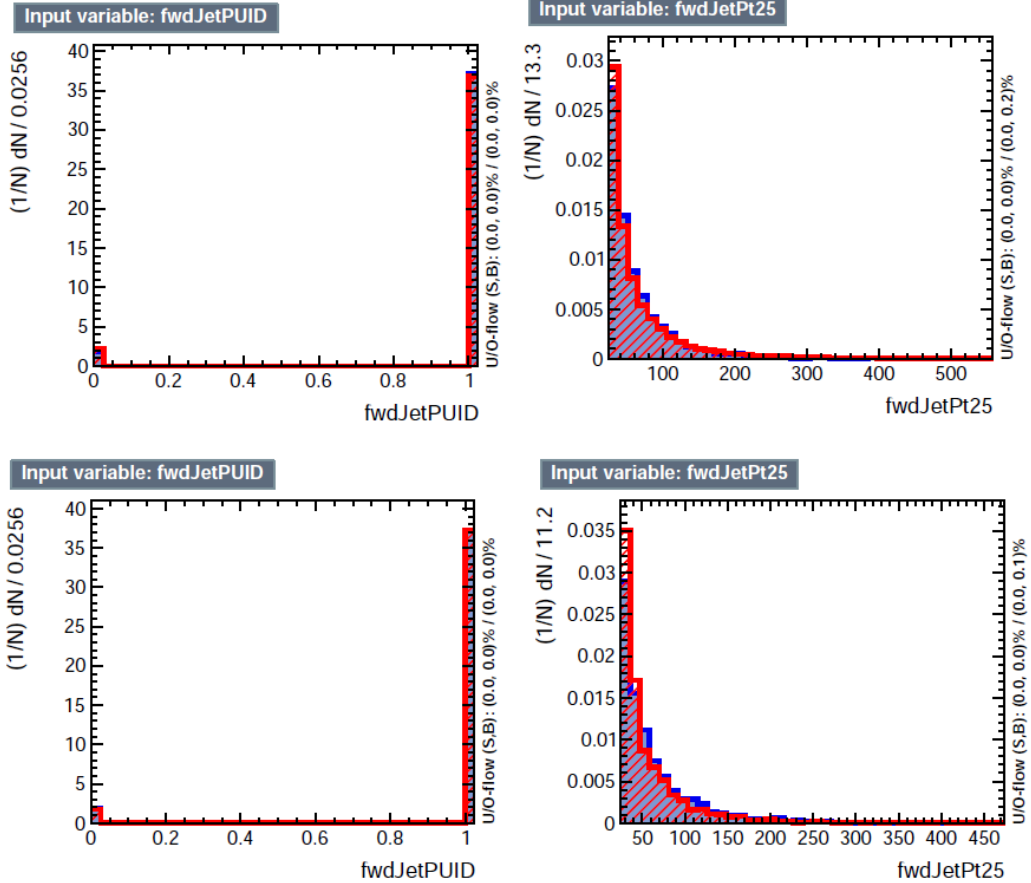


Figure 4.8: Additional discriminating variables distributions for ttV training (Top row) and tt training (bottom row) in the three lepton channel. The origin of the jets in the forward jet identification distribution is tagged as 0 for “pileup jets” while “real jets” are tagged as 1.

1271 can evaluate the discrimination power of each variable, and then both simultaneously.
 1272 fwdJetPUID was ranked in the last place in importance (11) in both training (ttV
 1273 and tt) while fwdJetPt25 was ranked 3 in the ttV training and 7 in the tt training.
 1274 When training using 12 variables, fwdJetPt25 was ranked 5 and 7 in the ttV and tt
 1275 trainings respectively, while fwdJetPUID was ranked 12 in both cases.

1276 The improvement in the discrimination performance provided by the additional
 1277 variables is about 1%, so it was decided not to include them in the procedure. Table
 1278 4.12 show the ROC-integral for all the testing cases we made.

ROC-integral	
base 10 var ttv	0.848
+ fwdJetPUID ttv	0.849
+ fwdJetPt25 ttv	0.856
12 var ttv	0.856
<hr/>	
base 10 var tt	0.777
+ fwdJetPUID tt	0.777
+ fwdJetPt25 tt	0.787
12 var	0.787

Table 4.12: ROC-integral for all the testing cases we made in the evaluation of the additional variables discriminating power. The improvement in the discrimination performance provided by the additional variables is about 1%

¹²⁷⁹ **Chapter 5**

¹²⁸⁰ **The CMS forward pixel detector**

¹²⁸¹ **5.0.1 The phase 1 FPix upgrade**

¹²⁸² **5.0.2 FPix module production line**

¹²⁸³ **5.0.3 The Gluing stage**

¹²⁸⁴ **5.0.4 The Encapsulation stage**

¹²⁸⁵ **5.0.5 The FPix module production yields**

1286 References

- 1287 [1] D.J. Griffiths, “Introduction to electrodynamics”. 4th ed. Pearson, (2013).
- 1288 [2] F. Mandl, G. Shaw. “Quantum field theory.” Chichester: Wiley (2009).
- 1289 [3] F. Halzen, and A.D. Martin, “Quarks and leptons: An introductory course in
1290 modern particle physics”. New York: Wiley, (1984) .
- 1291 [4] J.C. Maxwell. “A dynamical theory of the electromagnetic field”. Philosophical
1292 Transactions of the Royal Society of London. 155: 459â€¢512.(1865)
1293 doi:10.1098/rstl.1865.0008
- 1294 [5] M. Planck. “ÃIJber das Gesetz der Energieverteilung im Normalspektrum”.
1295 Annalen der Physik. 4 (3): 553.(1901).
- 1296 [6] A. Einstein “ÃIJber einen die Erzeugung und Verwandlung des Lichtes betref-
1297 fenden heuristischen Gesichtspunkt”. Annalen der Physik. 17 (6): 132â€¢148,
1298 (1905).
- 1299 [7] A. Einstein. “ÃIJber die von der molekularkinetischen Theorie der WÃdrme
1300 geforderte Bewegung von in ruhenden FlÃijssigkeiten suspendierten Teilchen”.
1301 Annalen der Physik. 17 (8): 549â€¢560, (1905).
- 1302 [8] A. Einstein. “Zur Elektrodynamik bewegter KÃürper”. Annalen der Physik. 17
1303 (10): 891â€¢921, (1905).

- 1304 [9] A. Einstein, "Ist die TrÄdgheit eines KÃürpers von seinem Energieinhalt ab-
 1305 hÃdngig?". Annalen der Physik. 18 (13): 639â€¢641, (1905).
- 1306 [10] B. P. Abbott et al. "Observation of Gravitational Waves from a Binary Black
 1307 Hole Merger". PRL 116, 061102 (2016).
- 1308 [11] J. Schwinger. "Quantum Electrodynamics. I. A Covariant Formulation". Phys-
 1309 ical Review. 74 (10): 1439â€¢61, (1948).
- 1310 [12] R. P. Feynman. "Spaceâ€¢Time Approach to Quantum Electrodynamics".
 1311 Physical Review. 76 (6): 769â€¢89, (1949).
- 1312 [13] S. Tomonaga. "On a Relativistically Invariant Formulation of the Quantum
 1313 Theory of Wave Fields". Progress of Theoretical Physics. 1 (2): 27â€¢42, (1946).
- 1314 [14] S.L. Glashow. "Partial symmetries of weak interactions", Nucl. Phys. 22 579-
 1315 588, (1961).
- 1316 [15] A. Salam, J.C. Ward. "Electromagnetic and weak interactions", Physics Letters
 1317 13 168-171, (1964).
- 1318 [16] S. Weinberg, "A model of leptons", Physical Review Letters, vol. 19, no. 21, p.
 1319 1264, (1967).
- 1320 [17] E. Noether, "Invariante Variationsprobleme", Nachrichten von der Gesellschaft
 1321 der Wissenschaften zu GÃüttingen, mathematisch-physikalische Klasse, vol.
 1322 1918, pp. 235â€¢257, (1918).
- 1323 [18] File:Standard_Model_of_Elementary_Particle_dark.svg. (2017, June 12)
 1324 Wikimedia Commons, the free media repository. Retrieved November 27,
 1325 2017 from <https://www.collegiate-advanced-electricity.com/single-post/2017/04/10/The-Standard-Model-of-Particle-Physics>.

- 1327 [19] M. Goldhaber, L. Grodzins, A.W. Sunyar “Helicity of Neutrinos”, Phys. Rev.
 1328 109, 1015 (1958).
- 1329 [20] Palanque-Delabrouille N et al. “Neutrino masses and cosmology with Lyman-
 1330 alpha forest power spectrum”, JCAP 11 011 (2015).
- 1331 [21] C. Patrignani et al. (Particle Data Group), Chin. Phys. C, 40, 100001 (2016)
 1332 and 2017 update.
- 1333 [22] M. Gell-Mann. “A Schematic Model of Baryons and Mesons”. Physics Letters.
 1334 8 (3): 214–215 (1964).
- 1335 [23] G. Zweig. “An SU(3) Model for Strong Interaction Symmetry and its Breaking”
 1336 (PDF). CERN Report No.8182/TH.401 (1964).
- 1337 [24] G. Zweig. “An SU(3) Model for Strong Interaction Symmetry and its Breaking:
 1338 II” (PDF). CERN Report No.8419/TH.412(1964).
- 1339 [25] M. Gell-Mann. “The Interpretation of the New Particles as Displaced Charged
 1340 Multiplets”. Il Nuovo Cimento 4: 848. (1956).
- 1341 [26] T. Nakano, K. Nishijima. “Charge Independence for V-particles”. Progress of
 1342 Theoretical Physics 10 (5): 581-582. (1953).
- 1343 [27] N. Cabibbo, “Unitary symmetry and leptonic decays” Physical Review Letters,
 1344 vol. 10, no. 12, p. 531, (1963).
- 1345 [28] M.Kobayashi, T.Maskawa, “CP-violation in the renormalizable theory of weak
 1346 interaction,” Progress of Theoretical Physics, vol. 49, no. 2, pp. 652-657, (1973).
- 1347 [29] File:Weak Decay (flipped).svg. (2017, June 12). Wikimedia Com-
 1348 mons, the free media repository. Retrieved November 27, 2017

- 1349 from `https : //commons.wikimedia.org/w/index.php?title = File :`
 1350 `Weak_Decay_(flipped).svg&oldid = 247498592.`
- 1351 [30] Georgia Tech University. Coupling Constants for the Fundamental
 1352 Forces(2005). Retrieved January 10, 2018, from `http://hyperphysics.phy –`
 1353 `astr.gsu.edu/hbase/Forces/couple.html#c2`
- 1354 [31] M. Strassler. (May 31, 2013).The Strengths of the Known Forces. Retrieved
 1355 January 10, 2018, from `https://profmattstrassler.com/articles – and –`
 1356 `posts/particle – physics – basics/the – known – forces – of – nature/the –`
 1357 `strength – of – the – known – forces/`
- 1358 [32] M. Peskin, D. Schroeder, “An introduction to quantum field theory”. Perseus
 1359 Books Publishing L.L.C., (1995).
- 1360 [33] A. Pich. “The Standard Model of Electroweak Interactions”
 1361 `https://arxiv.org/abs/1201.0537`
- 1362 [34] F.Bellaiche. (2012, 2 September). “What’s this Higgs boson anyway?”. Retrieved
 1363 from: `https://www.quantum-bits.org/?p=233`
- 1364 [35] M. Endres et al. Nature 487, 454-458 (2012) doi:10.1038/nature11255
- 1365 [36] F. Englert, R. Brout. “Broken Symmetry and the Mass of Gauge Vec-
 1366 tor Mesons”. Physical Review Letters. 13 (9): 321–323.(1964) Bib-
 1367 code:1964PhRvL..13..321E. doi:10.1103/PhysRevLett.13.321
- 1368 [37] P.Higgs. “Broken Symmetries and the Masses of Gauge Bosons”. Physical
 1369 Review Letters. 13 (16): 508–509,(1964). Bibcode:1964PhRvL..13..508H.
 1370 doi:10.1103/PhysRevLett.13.508.

- 1371 [38] G.Guralnik, C.R. Hagen and T.W.B. Kibble. “Global Conservation Laws and
 1372 Massless Particles”. Physical Review Letters. 13 (20): 585–587, (1964). Bib-
 1373 code:1964PhRvL..13..585G. doi:10.1103/PhysRevLett.13.585.
- 1374 [39] CMS collaboration. “Observation of a new boson at a mass of 125
 1375 GeV with the CMS experiment at the LHC”. Physics Letters B.
 1376 716 (1): 30–61 (2012). arXiv:1207.7235. Bibcode:2012PhLB..716...30C.
 1377 doi:10.1016/j.physletb.2012.08.021
- 1378 [40] ATLAS collaboration. “Observation of a New Particle in the Search for the Stan-
 1379 dard Model Higgs Boson with the ATLAS Detector at the LHC”. Physics Let-
 1380 ters B. 716 (1): 1–29(2012). arXiv:1207.7214 Bibcode:2012PhLB..716....1A.
 1381 doi:10.1016/j.physletb.2012.08.020.
- 1382 [41] ATLAS collaboration; CMS collaboration (26 March 2015). “Combined
 1383 Measurement of the Higgs Boson Mass in pp Collisions at $\sqrt{s}=7$ and
 1384 8 TeV with the ATLAS and CMS Experiments”. Physical Review Let-
 1385 ters. 114 (19): 191803. arXiv:1503.07589. Bibcode:2015PhRvL.114s1803A.
 1386 doi:10.1103/PhysRevLett.114.191803.
- 1387 [42] CMS Collaboration, “SM Higgs Branching Ratios and To-
 1388 tal Decay Widths (up-date in CERN Report4 2016)”.
 1389 <https://twiki.cern.ch/twiki/bin/view/LHCPhysics/CERNYellowReportPageBR>
 1390 , last accessed on 17.12.2017.
- 1391 [43] R.Grant V. “Determination of Higgs branching ratios in $H \rightarrow W^+W^- \rightarrow l^+l^- jj$ and $H \rightarrow ZZ \rightarrow l^+l^- jj$ channels”. Physics Department, Uni-
 1392 versity of Tennessee (Dated: October 31, 2012). Retrieved from
 1393 <http://aesop.phys.utk.edu/ph611/2012/projects/Riley.pdf>

- 1395 [44] LHC Higgs Cross Section Working Group, Denner, A., Heinemeyer, S. et al.
 1396 “Standard model Higgs-boson branching ratios with uncertainties”. Eur. Phys.
 1397 J. C (2011) 71: 1753. <https://doi.org/10.1140/epjc/s10052-011-1753-8>
- 1398 [45] LHC InternationalMasterclasses“When protons collide”. Retrieved from
 1399 http://atlas.physicsmasterclasses.org/en/zpath_protoncollisions.htm
- 1400 [46] F. Maltoni, K. Paul, T. Stelzer, and S. Willenbrock, “Associated production
 1401 of Higgs and single top at hadron colliders”, Phys.Rev. D64 (2001) 094023,
 1402 [hep-ph/0106293].
- 1403 [47] S. Biswas, E. Gabrielli, F. Margaroli, and B. Mele, “Direct constraints on the
 1404 top-Higgs coupling from the 8 TeV LHC data,” Journal of High Energy Physics,
 1405 vol. 07, p. 073, (2013).
- 1406 [48] M. Farina, C. Grojean, F. Maltoni, E. Salvioni, and A. Thamm, “Lifting de-
 1407 generacies in Higgs couplings using single top production in association with a
 1408 Higgs boson,” Journal of High Energy Physics, vol. 05, p. 022, (2013).
- 1409 [49] T.M. Tait and C.-P. Yuan, “Single top quark production as a window to physics
 1410 beyond the standard model”, Phys. Rev. D 63 (2000) 014018 [hep-ph/0007298].
- 1411 [50] F. Demartin, F. Maltoni, K. Mawatari, and M. Zaro, “Higgs production in
 1412 association with a single top quark at the LHC,” European Physical Journal C,
 1413 vol. 75, p. 267, (2015).
- 1414 [51] CMS Collaboration, “Modelling of the single top-quark pro-
 1415 duction in association with the Higgs boson at 13 TeV.”
 1416 <https://twiki.cern.ch/twiki/bin/viewauth/CMS/SingleTopHiggsGeneration13TeV>,
 1417 last accessed on 16.01.2018.

- 1418 [52] CMS Collaboration, “SM Higgs production cross sections at $\sqrt{s} = 13$ TeV.”
 1419 <https://twiki.cern.ch/twiki/bin/view/LHCPhysics/CERNYellowReportPageAt13TeV>,
 1420 last accessed on 16.01.2018.
- 1421 [53] S. Dawson, The effective W approximation, Nucl. Phys. B 249 (1985) 42.
- 1422 [54] S. Biswas, E. Gabrielli and B. Mele, JHEP 1301 (2013) 088 [arXiv:1211.0499
 1423 [hep-ph]].
- 1424 [55] F. Demartin, B. Maier, F. Maltoni, K. Mawatari, and M. Zaro, “tWH associated
 1425 production at the LHC”, European Physical Journal C, vol. 77, p. 34, (2017).
 1426 arXiv:1607.05862
- 1427 [56] LHC Higgs Cross Section Working Group, “Handbook of LHC Higgs Cross
 1428 Sections: 4.Deciphering the Nature of the Higgs Sector”, arXiv:1610.07922.
- 1429 [57] J. Ellis, D. S. Hwang, K. Sakurai, and M. Takeuchi.“Disentangling Higgs-Top
 1430 Couplings in Associated Production”, JHEP 1404 (2014) 004, [arXiv:1312.5736].
- 1431 [58] CMS Collaboration, V. Khachatryan et al., “Precise determination of the mass
 1432 of the Higgs boson and tests of compatibility of its couplings with the standard
 1433 model predictions using proton collisions at 7 and 8 TeV,” arXiv:1412.8662.
- 1434 [59] ATLAS Collaboration, G. Aad et al., “Updated coupling measurements of the
 1435 Higgs boson with the ATLAS detector using up to 25 fb^{-1} of proton-proton
 1436 collision data”, ATLAS-CONF-2014-009.
- 1437 [60] ATLAS and CMS Collaborations, “Measurements of the Higgs boson produc-
 1438 tion and decay rates and constraints on its couplings from a combined ATLAS
 1439 and CMS analysis of the LHC pp collision data at $\sqrt{s} = 7$ and 8 TeV,” (2016).
 1440 CERN-EP-2016-100, ATLAS-HIGG-2015-07, CMS-HIG-15-002.

- 1441 [61] File:Cern-accelerator-complex.svg. Wikimedia Commons,
 1442 the free media repository. Retrieved January, 2018 from
 1443 <https://commons.wikimedia.org/wiki/File:Cern-accelerator-complex.svg>
- 1444 [62] J.L. Caron , “Layout of the LEP tunnel including future LHC infrastructures.”, (Nov, 1993). A C Collection. Legacy of AC. Pictures from 1992 to 2002. Retrieved from <https://cds.cern.ch/record/841542>
- 1447 [63] M. Vretenar, “The radio-frequency quadrupole”. CERN Yellow Report CERN-
 1448 2013-001, pp.207-223 DOI:10.5170/CERN-2013-001.207. arXiv:1303.6762
- 1449 [64] L.Evans. P. Bryant (editors). “LHC Machine”. JINST 3 S08001 (2008).
- 1450 [65] CERN Photographic Service.“Radio-frequency quadrupole, RFQ-1”, March
 1451 1983, CERN-AC-8303511. Retrieved from <https://cds.cern.ch/record/615852>.
- 1452 [66] CERN Photographic Service “Animation of CERN’s accelerator net-
 1453 work”, 14 October 2013. DOI: 10.17181/cds.1610170 Retrieved from
 1454 <https://videos.cern.ch/record/1610170>
- 1455 [67] C.Sutton. “Particle accelerator”.Encyclopedia Britannica. July 17, 2013. Re-
 1456 trieved from <https://www.britannica.com/technology/particle-accelerator>.
- 1457 [68] L.Guiraud. “Installation of LHC cavity in vacuum tank.”. July 27 2000. CERN-
 1458 AC-0007016. Retrieved from <https://cds.cern.ch/record/41567>.
- 1459 [69] J.L. Caron, “Magnetic field induced by the LHC dipole’s superconducting coils”. March 1998. AC Collection. Legacy of AC. Pictures from 1992 to 2002. LHC-
 1460 PHO-1998-325. Retrieved from <https://cds.cern.ch/record/841511>
- 1462 [70] AC Team. “Diagram of an LHC dipole magnet”. June 1999. CERN-DI-9906025
 1463 retrieved from <https://cds.cern.ch/record/40524>.

- 1464 [71] CMS Collaboration “Public CMS Luminosity Information”.
 1465 https://twiki.cern.ch/twiki/bin/view/CMSPublic/LumiPublicResults#2016_proton_proton
 1466 last accessed 24.01.2018
- 1467 [72] CMS Collaboration, “Search for the associated production of a Higgs boson
 1468 with a single top quark in proton-proton collisions at $\sqrt{s} = 8$ TeV”, JHEP 06
 1469 (2016) 177, doi:10.1007/JHEP06(2016)177, arXiv:1509.08159.
- 1470 [73] B. Stieger, C. Jorda Lope et al., “Search for Associated Production of a Single
 1471 Top Quark and a Higgs Boson in Leptonic Channels”, CMS Analysis Note CMS
 1472 AN-14-140, 2014.
- 1473 [74] M. Peruzzi, C. Mueller, B. Stieger et al., “Search for ttH in multilepton final
 1474 states at $\sqrt{s} = 13$ TeV”, CMS Analysis Note CMS AN-16-211, 2016.
- 1475 [75] CMS Collaboration, “Search for H to bbar in association with a single top quark
 1476 as a test of Higgs boson couplings at $\sqrt{s} = 13$ TeV”, CMS Physics Analysis
 1477 Summary CMS-PAS-HIG-16-019, 2016.
- 1478 [76] B. Maier, “SingleTopHiggProduction13TeV”, February, 2016.
 1479 <https://twiki.cern.ch/twiki/bin/viewauth/CMS/SingleTopHiggsGeneration13TeV>.
- 1480 [77] M. Peruzzi, F. Romeo, B. Stieger et al., “Search for ttH in multilepton final1
 1481 states at $\sqrt{s} = 13$ TeV”, CMS Analysis Note CMS AN-17-029, 2017.
- 1482 [78] B. WG, “BtagRecommendation80XReReco”, February, 2017.
 1483 <https://twiki.cern.ch/twiki/bin/view/CMS/BtagRecommendation80XReReco>.